Yale University

EliScholar – A Digital Platform for Scholarly Publishing at Yale

Yale Graduate School of Arts and Sciences Dissertations

Spring 2021

Energetics of Biological Mechanics and Dynamics

Daniel Seara

Yale University Graduate School of Arts and Sciences, dsseara@gmail.com

Follow this and additional works at: https://elischolar.library.yale.edu/gsas_dissertations

Recommended Citation

Seara, Daniel, "Energetics of Biological Mechanics and Dynamics" (2021). *Yale Graduate School of Arts and Sciences Dissertations*. 112.
https://elischolar.library.yale.edu/gsas_dissertations/112

This Dissertation is brought to you for free and open access by EliScholar – A Digital Platform for Scholarly Publishing at Yale. It has been accepted for inclusion in Yale Graduate School of Arts and Sciences Dissertations by an authorized administrator of EliScholar – A Digital Platform for Scholarly Publishing at Yale. For more information, please contact elischolar@yale.edu.

Abstract

Energetics of Biological Mechanics and Dynamics

Daniel S. Seara

2021

Living matter is a class of soft matter systems that maintains itself away from thermodynamic equilibrium by the continual consumption of energy. Individual proteins consume energy and break detailed balance to drive active force generation by molecular motors, force-dependent binding kinetics, and chemically driven (dis)assembly. These non-equilibrium dynamics propagate across heterogeneous structures to drive essential life processes such as replication, migration, and shape change at the scale of both single cells and multicellular tissues. While much work has been done to understand the molecular processes underlying each individual non-equilibrium behaviors, we lack a general understanding of how the microscopic breaking of detailed balance translates to large-scale cellular behaviors and materials properties.

Using the tools of non-equilibrium thermodynamics, this thesis examines this question by estimating energy dissipation during dynamical and mechanical phase transitions seen in experiments, simulations, and theoretical models of biological materials. We choose the actomyosin cytoskeleton, a network composed of polymeric proteins (actin) that are driven away from thermodynamic equilibrium by the activity of molecular motors (myosin), as our model system. Actomyosin contains the three types of non-equilibrium driving we will focus on: force generation, non-equilibrium binding kinetics, and active (dis)assembly. At the subcellular level, analysis of actin filament motions in experiments shows that energy dissipated through bending controls the transition between stable and contractile steady states. Using simulations, we show that non-equilibrium binding kinetics of molecular motors controls a fluid-solid phase transition characterized by thermodynamic quantities with opposite symmetries under time-reversal. At the cellular level, we develop new tools for measuring irreversibility in spatiotemporal dynamics to analyze the energetic costs of oscillations and synchronization of a model biochemical oscillator inspired by (dis)assembly driven actomyosin dynamics.

Throughout this thesis, we show that a cell's distance from equilibrium tunes its mechanical properties and dynamics. This establishes non-equilibrium thermodynamics as a common language with which to unify disparate biological functions, establishing a framework for discovering universal design principles for living matter.

Energetics of Biological Mechanics and Dynamics

A Dissertation
Presented to the Faculty of the Graduate School
of
Yale University
in Candidacy for the Degree of
Doctor of Philosophy

by
Daniel S. Seara

Dissertation Director: Michael P. Murrell

June 2021

Copyright © 2021 by Daniel S. Seara

All rights reserved.

Acknowledgments

I have been lucky to work with and learn from many excellent scientists during my Ph.D. First and foremost, I have to give thanks to the members of my thesis committee. To my advisor, Michael Murrell, for taking a chance in taking on an aspiring theorist in his lab, for giving me the freedom to pursue my science, and for teaching me how to ask big scientific questions. To Benjamin Machta for sharing his intuition, skill, and enthusiasm for theoretical physics, and for helping me build the BioSoftMatter community at Yale. To Simon Mochrie, whose vision for biophysics at Yale Physics Department has shaped my time there and whose course I helped teach was fundamental in my own development as a biophysicist. Finally, to Steven Girvin for incisive questions that broadened my perspectives on my work beyond biology.

In addition to my committee, my collaborators, especially Shiladitya Banerjee and Bill Bement, have been instrumental to my growth as a scientist. The past and present members of the Lab of Living Matter – Ian Linsmeier, Pasha Tabatabai, Vikrant Yadav, Camelia Muresan, Sulaiman Yousafszai, Sorosh Amiri, Zachary Sun, Laura Lanier, Dong Wang – have made my this work not only possible but also, more importantly, enjoyable. The PEB program at Yale gave me access to an international biophysics community. I am especially indebted to Enrique De la Cruz and Dorottya Noble, whose guidance and support throughout my Ph.D. is a major reason for my continuing in this career. Furthermore, every person I have had to pleasure of working with for any amount of time – Thierry Emonet, John Wettlauffer, David Pine – have each left indelible marks in my approach towards science.

I have been extremely lucky to meet incredibly talented peers at Yale who have not only made me smarter, but have made my time in graduate school more fun than it has an right to be. This includes my physics cohort and beyond – Paul, Chris, Ryan, Hannah, Kelly, Simone, Jeremy, Sam, Jack, Sohan, Will, Bara, Patrick, Savannah, *et al.* I also have an amazing community of people outside of Yale who have made me smarter, kinder, and happier during my time in New Haven. They are most conveniently grouped under the umbrella of Jabroni Studios$^{\text{TM}}$ – Ratan, Cary, Annalisa, Sam, Max, Jeanette, Annie, Kayleigh, Nina, Ethan, Lex, Victor *et al.*. These are non-exhaustive lists and the reason anyone has not been mentioned is my own poor memory, not their impact on my life.

An especially large thank you for my partner, Mariel. You've been my biggest advocate, cheerleader, and confidante throughout my Ph.D. and I cannot imagine my time here without you. Thank you for the adventures and for inspiring me with the examples you set in your life and your incredible work.

Finally, I have to thank my entire family, but especially my parents Elizabeth and Saul. They sacrificed more than I have ever had to in order to give me the freedom to pursue my dreams and passions. The work done in this thesis is only possible because of them.

Para mis abuelos

Contents

List of Figures

List of Tables

Chapter 1

Introduction

It is in relation to the statistical point of view that the structure of the vital parts of living organisms differs so entirely from that of any piece of matter that we physicists and chemists have ever handled.

Erwin Schrodinger, *What is Life?*

Living matter constitutes a class of complex, many-body systems characterized by self-replication and adaptation performed via evolutionarily selected mechanisms. These mechanisms are powered by chemical reactions that result in the generation of mechanical work, processing of information, and synthesis of new materials. These chemical reactions occur in microscopic systems that exchange energy and particles with a fluctuating environment and are constantly barraged by thermal noise. In other words – living matter is quintessentially non-equilibrium with no right to predictable or long-lived dynamics at the level physicists have come to expect from non-living matter.

And yet, genes are conserved over time-scales relevant for plate tectonics [9]. Proteins extracted from a cell will spontaneously self-assemble into properly functioning, complex machines that perform their original function in under an hour [10]. DNA is replicated at a rate of 1,000 base pairs per second, with an error rate of 1 per million base pairs [11]. Unlike non-living matter that succumbs to chaos, turbulence, or decoherence when driven away from equilibrium, living matter builds robust, reproducible dynamics and structures by continually consuming and dissipating energy.

The question that remains is – How does non-equilibrium driving give rise to ordered dynamics across time and length scales? This question is fundamentally physical in nature. However, as noted by Erwin Schrödinger in the quote at the beginning of this chapter, living matter is unlike any other matter physicists have dealt with. In a broad sense, this stems from living matter's ability to avoid thermodynamic equilibrium for long periods of time, delaying the eventual decay to disorder required by the laws of thermodynamics. Progress in biological physics, therefore, is synonymous with progress in non-equilibrium physics.

The work in this thesis studies how entropy production at the microscopic scale leads to various mechanical and dynamical phases and transitions at larger length scales in biological materials. I take an approach rooted in statistical physics to tie entropy production to biological function. In this chapter, after reviewing equilibrium thermodynamics in Section 1.1, I introduce the theoretical framework I build upon throughout the rest of the thesis, *stochastic thermodynamics* [12]. Stochastic thermodynamics ascribes thermodynamic interpretations to systems at the microscopic scale ($\ell \sim 1$ μm) driven arbitrarily far from equilibrium, and has found increasing use in the description of living matter [13].

In Section 1.3 I introduce three related, but distinct, sources of non-equilibrium behavior and discuss their impacts on the mechanics and dynamics of biological materials. In particular, I focus on the generation of active stress, force-dependent binding kinetics, and (dis)assembly. Each of these phenomena are explained through the lens of the *actomyosin cytoskeleton*, which I take as a model system for a more general class of active, adaptive biological materials. For each phenomenon, I introduce previous attempts to study their non-equilibrium behavior, and briefly explain how the work in subsequent chapters expands upon them.

1.1 Review of statistical physics

Statistical physics is the study of the mathematical laws that govern the dynamics and properties of *macroscopic* systems. Roughly speaking, macroscopic systems are those found at the human scale, for example, a liter of gas that contains $\sim 10^{23}$ particles. To predict the evolution of the gas using the framework of classical mechanics, one could "simply" write and integrate the 10^{23} coupled ordinary differential equations that express Newton's Laws for each particle. Not only is a solution analytically intractable, numerical methods will also be almost useless[1]. While intuition based solely on Newtonian mechanics would indicate that macroscopic systems are unpredictable, everyday experience instead illustrates that macroscopic systems are remarkably regular and predictable, described by a handful of thermodynamic quantities such as pressure, volume, temperature, heat, work, and entropy. Statistical mechanics gives us map from the behavior of individual particles to those quantities. As we will be eventually dealing with biological systems at a scale where quantum effects are unimportant, we will focus solely on classical systems.

1.1.1 Microcanonical ensemble

We begin by considering a system composed of N particles within a volume V. The particles can be described by a set of generalized coordinates x_i, that can encode positions, momenta, spins, etc. A particular state of the system is given by the vector $\mathbf{m}$, called a *microstate*. This microstate is a vector in a *phase space*, Γ, spanned by

---

[1] At the time of this writing in January 2021, the fastest supercomputer in the world is the Japanese Fugaku supercomputer which operates at $\sim 4 \times 10^{17}$ floating point operations per second. With a generous assumption that each equation only requires a single floating point operation (addition or multiplication) 10^{23} equations/$4 \times 10^{17} FLOPS \approx 3$ days.

$\{x_i\}$. If this system is isolated from the environment, the total internal energy E will remain fixed. The collection of all microstates with a particular value of E makes up a *macrostate*. While we cannot control the fluctuations of $\mathbf{m}$, we know it must be confined to the portion of phase space where the Hamiltonian, $\mathcal{H}(\mathbf{m})$, is equal to the system's energy E. The central postulate of statistical mechanics is that all $\mathbf{m}$ compatible with $\mathcal{H}(\mathbf{m}) = E$, i.e. all the microstates within a macrostate, are equally probable. This defines the *microcanonical ensemble*, which gives the probability for observing a particular microstate given a particular macrostate:

$$p(\mathbf{m}|E) = \frac{1}{\Omega(E)}\delta(\mathcal{H}(\mathbf{m}) - E). \tag{1.1}$$

In Equation 1.1, $\Omega(E)$ is the volume of phase space that satisfies $\mathcal{H}(\mathbf{m}) = E$ to ensure proper normalization of the probability distribution, i.e. $\int_\Gamma \mathrm{d}\mathbf{m}\, p(\mathbf{m}|E) = 1$. As is often the case in statistical mechanics, this normalization constant plays an outsize role in what follows. For a collection of independent systems, the total allowed phase space volume is given as the product of the volumes of the subsystems, $\prod_j \Omega_j$. However, the total energy of the system is an extensive quantity, given by the sum of the energies of the subsystems, $\sum_j E_j$. In order to better correspond the change in phase space volume with the change in energy, we define the *entropy*, S, as the natural logarithm of Ω:

$$S(E) = k_\mathrm{B} \ln \Omega(E), \tag{1.2}$$

where k_B is the Boltzmann constant, which gives S units of energy per Kelvin. Equation 1.2 is called the Boltzmann entropy, and can be found on its namesake's gravestone in Vienna if you ever need a quick reminder.

Like the energy, S is an additive function of the number of subsystems. Equation 1.2 allows us to write the relative probability of observing a particular state with energy E_1 with respect to another state with energy E_2, given by the ratio of the two phase space volumes, in terms of the difference in the entropy between the two states, i.e.

$$\frac{\Omega(E_1)}{\Omega(E_2)} = \exp(\Delta S/k_{\mathrm{B}}) \tag{1.3}$$

Expressions of this form that relate relative probabilities to entropy differences will play a pivotal role in non-equilibrium statistical mechanics.

Thermodynamic equilibrium can be defined as the state where two interacting systems with total energy $E_{\mathrm{tot}} = E_1 + E_2$ stop evolving in time. In the thermodynamic limit, this state is fixed around some energies (E_1^*, E_2^*) where the phase space volume is exponentially larger than any other state [14]. This position in Γ being a maximum of Ω implies that the variation in the entropy

$$\left.\frac{\partial S_1}{\partial E_1}\right|_{E_1^*} = \left.\frac{\partial S_2}{\partial E_2}\right|_{E_2^*}, \tag{1.4}$$

where the vertical line indicates to evaluate the derivative at E_1^*. The derivative $\partial S/\partial E = T^{-1}$ is defined as the (inverse) temperature, making the equilibrium condition equivalent to the two subsystems having the same temperature.

1.1.2 First law of thermodynamics

We can also consider other parameters that describe the system beyond the energy. Traditional introductions to statistical mechanics consider the bulk of three dimensional systems and therefore use the volume, V, as this additional parameter. However, there is nothing special about the volume, so we will consider a general vector of parameters, $\mathbf{x}$. Before we saw that equilibrium occurs when $\partial S/\partial E$ is equal between subsystems. Using the same line of reasoning, we now also consider the entropy changes with respect to each component of $\mathbf{x}$. Now, the energy is a function of these new parameters, $E = E(\mathbf{x})$, which endows the phase space volume, and therefore the entropy, with dependence on $\mathbf{x}$, $S = S(E(\mathbf{x}))$. Using the chain rule of calculus, we can write

$$\frac{\partial S}{\partial x_i} = \frac{\partial S}{\partial E}\frac{\partial E}{\partial x_i} = -T^{-1} J_i. \tag{1.5}$$

In the above, we recognized the definition of the temperature, and defined a new quantity, $J_i \equiv -\partial E/\partial x_i$. We call this quantity a *generalized force*, as it is written as a gradient of the energy, similar to the definition of a force in classical mechanics, $F = -\nabla U$. For example, when we consider a change in volume, J_i is the pressure p, and when we consider a change in the total number of particles, J_i is the chemical potential, μ.

We can write the total variation in the entropy as

$$\mathrm{d}S = \frac{\partial S}{\partial E}\,\mathrm{d}E + \frac{\partial S}{\partial x_i}\,\mathrm{d}x_i\,, \tag{1.6}$$

where summation over repeated indices is implied. Rearranging and using the definition for temperature and the generalized force, we have

$$\mathrm{d}E = T\,\mathrm{d}S + J_i\,\mathrm{d}x_i\,. \tag{1.7}$$

This is the *first law of thermodynamics*, which is a statement about the conservation of energy. Any change in energy stems from either a change in entropy or a change in the parameters that define the system.

1.1.3 Second law of thermodynamics

Classical thermodynamics is related to statistical mechanics by relating two forms of energy, heat Q and work W, with the first two terms in Equation 1.7, respectively

$$\mathrm{d}E = đQ + đW \tag{1.8}$$

The symbol $đ$ is meant to signify that the work and heat performed depend on the specific protocol used to induce a change in the energy. The work, $đW = J_i \, \mathrm{d}x_i$ follows directly from its definition in classical mechanics as a force multiplied by a displacement, but the relationship $đQ = T \, \mathrm{d}S$ is more subtle. The total heat exchange is a path-dependent function, while the entropy S is a state function, independent of how a system happened to be prepared. However, if the protocol used is reversible, meaning the system stays in equilibrium at every point between the initial and final times, the quantity Q/T is itself a state function that is equal to S. Integrating Q/T along a reversible path γ_{rev} between an initial equilibrium state A and final equilibrium state B is the entropy change between the two states

$$\int_{\gamma_{\text{rev}}} \frac{đQ}{T} = \Delta S \tag{1.9}$$

If the process instead takes an *irreversible* path, γ_{irr}, the heat exchanged is smaller than the heat exchanged during its reversible counterpart. Intuitively, this is due to the fact that reversible processes are done extremely slowly and heat transfer occurs at a rate dependent on the temperature difference and a substance-specific quantity called the heat capacity. Equating the heat exchange during the irreversible process with the change in entropy, we can write

$$\int_{\gamma_{\mathrm{irr}}} \frac{đQ}{T} \leq \Delta S \tag{1.10}$$

This is the *second law of thermodynamics*, as given by Rudolph Clausius. With this, we can write the change in entropy of a system as a sum of two components, the heat exchanged over γ_{irr} and an *entropy production*, S_{prod}

$$\Delta S = \frac{Q}{T} + S_{\mathrm{prod}}$$

Then, the second law of thermodynamics can be written as

$$S_{\mathrm{prod}} \geq 0. \tag{1.11}$$

The entropy production can be considered the total entropy increase that the system and the environment experience as a result of performing irreversible protocols. The second law is therefore sometimes explained as a statement asserting that the total entropy production of the "universe" must increase, $\Delta S_{\mathrm{tot}} \geq 0$. These statements directly relate irreversibility to entropy production, a concept that will play an important role in non-equilibrium statistical mechanics.

1.1.4 Canonical Ensemble

While the microcanonical ensemble assumes that the energy of the system can be specified precisely to define our macrostate and the exact configuration of our system, the microstate, was allowed to fluctuate. However, interactions with the environment make this approach impractical. Instead, if the environment (also called a heat bath) is large compared to the system, its temperature will remain constant in spite of any exchange of energy. The probability distribution of observed a particular microstate given a particular temperature for a system that obeys a Hamiltonian $\mathcal{H}(\mathbf{m})$ is given by the *canonical ensemble*

$$p(\mathbf{m}|T) = \frac{1}{Z}\int \mathrm{d}\mathbf{m}\exp(-\beta\mathcal{H}(\mathbf{m})) \tag{1.12}$$

where we have defined $\beta = (k_\mathrm{B}T)^{-1}$, which gives the energy scale of fluctuations in a heat bath of temperature T.

The normalization constant $Z = \int \mathrm{d}\mathbf{m}\exp(-\beta\mathcal{H})$ is called the *partition function*. Much like the microcanonical normalization constant Ω, Z plays an outsize role when making calculations using the canonical ensemble. Similarly to Ω, Z is multiplicative in composite systems. In order to get an additive function analogous to energy, we can again take the natural logarithm of the normalization constant to define a new, surprisingly useful function, the *free energy* F:

$$-\beta F = \ln(Z). \tag{1.13}$$

With this, we can rewrite Equation 1.12 as $p(\mathbf{m}) = \exp(-\beta(\mathcal{H}(\mathbf{m}) - F))$.

The Boltzmann entropy, Equation 1.2, provides a definition of the entropy under the equiprobability assumption. If $\Omega(E)$ is the volume of phase space at a particular energy E, then $\rho = \Omega^{-1}$ is a phase space density which gives the probability of observing a state with energy E. The entropy can then be rewritten as $S = -k_\mathrm{B}\ln\rho$. However, the canonical ensemble tells us that fixing the temperature renders microstates nonequiprobable – they are weighted by $\exp(-\beta\mathcal{H})$. Josiah Gibbs[2] showed that, in general, the entropy can be written as the average over the logarithm of the

---

[2] Josiah Willard Gibbs (1839-1903) was the pinnacle of a Yale man. He was born in New Haven, attended Yale University for his undergraduate and Ph.D. studies, and worked in the Physics Department at Yale for his entire career. He almost single handedly invented our modern formulation of statistical mechanics[15]

probability distribution over microstates:

$$S = -k_{\mathrm{B}} \int \mathrm{d}\mathbf{m}\, \rho(\mathbf{m}) \ln \rho(\mathbf{m}). \tag{1.14}$$

Note that this is closely related to the information theoretic entropy, $H = \sum p_i \ln p_i$, which measures the uncertainty in a discrete probability distribution p_i [16]. In the canonical ensemble, we have

$$S = -k_{\mathrm{B}} \langle -\beta\mathcal{H} - F \rangle \to F = E - TS, \tag{1.15}$$

where we have replaced $\langle \mathcal{H} \rangle$ with the energy E. As $N \to \infty$, this approximation becomes exact as fluctuations in the energy scale as $N^{-1/2}$. In this limit, the two definitions of entropy (Equations 1.2 & 1.14) coincide as the averages become indistinguishable from their most probable values.

The free energy is the amount of energy available to perform work, a result that comes directly from an application of the Second Law, Equation 1.11. Rewriting the entropy production as $S_{\mathrm{prod}} = \Delta S - Q/T \geq 0$, we can use the finite version the first law to replace the heat, $Q = \Delta E - W$. This gives

$$W - (\Delta E - T\Delta S) = W - \Delta F \geq 0. \tag{1.16}$$

The equality holds during a reversible process, giving $W_{\mathrm{rev}} = \Delta F$. While an irreversible process results in a lower transfer of heat, we now see it comes at the cost of an increase in the amount of work performed. This excess work, W_{diss}, is then dissipated. If the process done is isothermal, W_{diss} is equal to the heat given to the heat bath, which is related to the entropy production, giving

$$W_{\mathrm{diss}} = TS_{\mathrm{prod}}. \tag{1.17}$$

1.1.5 Irreversibility near equilibrium

The above laws of thermodynamics underpin the regularity seen in macroscopic systems at equilibrium, circumventing the need to detail every microscopic interaction within them. They come from purely probabilistic arguments that assume a very large number of particles, weak interactions, and slow, reversible variations. Anytime irreversibile processes occurred, we are left with inequalities, such as $S_{\text{prod}} \geq 0$ and $W_{\text{diss}} \geq \Delta F$. However, Lars Onsager[3] showed that one can do better if we operate near equilibrium [17, 18].

In these cases, the entropy production rate $\dot{S}$ can be written as a linear combination of the product between thermodynamic forces F_i and their resulting flux J_i, $\dot{S} = F_i J_i$, where summation over repeated indices is implied. Examples include gradients in temperature driving a flux of heat or gradients in concentration driving flux in matter (two examples of Fick's law), and an electric field driving a current (a.k.a. Ohm's Law). Near equilibrium, the forces themselves can also be written as a linear combination of the fluxes, $F_i = L_{ij} J_j$, where L_{ij} are phenomeneological constants that make up a symmetric matrix, i.e. $L_{ij} = L_{ji}$. This general statement constitutes Onsager's reciprocal relations

$$\dot{S} = L_{ij} J_i J_j. \tag{1.18}$$

We see here that $\dot{S}$ is a positive definite, quadratic form of the fluxes, implying that entropy production is associated with the presence of observable flows, without regard for the direction of the flow.

Biological systems, on the other hand, break the assumption of linearity between forces and fluxes. As a consequence, they are considered far-from equilibrium

---

[3] Lars Onsager (1903-1976), born 6 months after Gibbs died, became another giant of statistical mechanics to work out of Yale University.

and a new formalism is needed to describe the flow of work and energy. Over the past two decades, the field of stochastic thermodynamics has been developed and successfully applied to studying various living and non-living systems driven away from thermodynamic equilibrium [12]. While the introduction below only deals with classical systems, many of the ideas have been extended to quantum systems as well [19, 20, 21].

1.2 Stochastic Thermodynamics

Stochastic thermodynamics is a theory that assigns thermodynamic interpretations to the dynamics of microscopic systems immersed in some solution such as colloidal particles, biopolymers, and molecular motors [12]. While there are several ways to be driven away from equilibrium, we will focus in particular on cases where there exists a time-independent external driving force. While these forces can have many origins, such as an external field or flow or unbalanced chemical potentials, they largely result in establishing a non-equilibrium steady state (NESS) in the system dynamics. In all cases, the temperature of the system is defined as the temperature of the solution in which the system is submerged. In conjunction with a separation of time-scales between the time it takes for the observable and unobservable degrees of freedom to reach equilibrium, a self-consistent thermodynamic description can be achieved.

Depending on the type of dynamics and the time and length scales involved, there exist several different descriptions for stochastic dynamics. We will begin with the most common, the Langevin Equation description of Brownian motion. After first deriving expressions for systems near-equilibrium, such as the fluctuation dissipation theorem, we will use the Langevin equation to illustrate the main features of stochastic thermodynamics, specifically the identification of heat, work, and entropy as stochastic variables defined according to individual trajectories. Each Langevin equation can be mapped onto two other descriptions of stochastic dynamics – the Fokker-Planck equation describing the evolution of an ensemble of trajectories, and a path-integral description for the probability of observing a particular trajectory. Finally, coarse-graining can lead to discrete dynamics governed by a Master Equation for the transition rates between states. For each description of stochastic dynamics, we will discuss the associated expression for the entropy production rate.

1.2.1 Brownian motion and the Langevin Equation

The paradigmatic example used throughout stochastic thermodynamics is that of a *Brownian particle*. Brownian particles are generally approximately 1 μm in size and immersed in a fluid at temperature T whose atoms bombard the Brownian particle to induce a random walking motion [22]. At this scale, the Reynold's number is very small, Re $\sim 10^{-4}$, rendering inertial effects negligible [23]. The mean-square displacement of a Brownian particle in d dimensions increases linearly in time with a slope defined by its diffusion coefficient D

$$\left\langle (\mathbf{x}(t) - \mathbf{x}(0))^2 \right\rangle = 2dDt. \tag{1.19}$$

In 1905, Einstein showed that D is related to the drag coefficient of the colloid γ and the temperature of the ambient fluid T in equilibrium by [22]

$$D = \frac{k_{\mathrm{B}} T}{\gamma}. \tag{1.20}$$

These two unassuming equations have had a massive impact on physics. Jean Baptiste Perrin used them to experimentally measure Avogadro's number in 1908 [24], which is widely considered as the piece of evidence that definitively ended the dispute over the existence of atoms, earning Perrin a Nobel Prize in 1926 [25][4].

Equation 1.20 is a particular version of the fluctuation-dissipation theorem, as given in linear response theory [27]. This theorem holds near equilibrium, and states that correlations due to thermal fluctuations contain the same information as the response to a small perturbation. To be precise, it relates the correlation function, $C(t-t') = \langle x(t)x(t')\rangle$ to the response function, $\chi(t-t')$ defined for a small perturbation $h(t)$ using $\langle x(t)\rangle = \int \mathrm{d}t'\, \chi(t-t')h(t')$. In equilibrium, the fluctuation dissipation theorem is most commonly written in terms of the Fourier transforms of C and χ,

$$C(\omega) = \frac{2k_{\mathrm{B}}T}{\omega}\widetilde{\chi}(\omega), \tag{1.21}$$

where $\widetilde{\chi}$ is the imaginary part of the complex-valued $\chi(\omega)$.

In 1911, Paul Langevin wrote an equivalent yet, in his own words, "infinitely more simple" description of Brownian motion based on a stochastic differential equation [28]. This approach applies Newton's Law, $F = ma$, to the Brownian particle, but averages the effects from the surrounding fluid into a random force. In general, the Langevin equation for an overdamped Brownian particle in an external potential V and subject to a non-conservative force $\mathbf{f}$ is given by

$$\gamma\frac{\partial \mathbf{x}}{\partial t} = -\nabla V(\mathbf{x},\lambda) + \mathbf{f}(\mathbf{x},\lambda) + \boldsymbol{\xi} = \mathbf{F}(\mathbf{x},\lambda) + \boldsymbol{\xi}, \tag{1.22}$$

where $\mathbf{F} = -\nabla V + \mathbf{f}$ is the total force. For our case here, both the potential landscape V and non-conservative force $\mathbf{f}$ can be made time-dependent by the action of some external control parameter, $\lambda(t)$, which varies according to some prescribed

---

[4] This triumph is also marred by a tragedy. Ludwig Boltzmann, the first physicist to write $S = k_{\mathrm{B}} \ln \Omega$, was harshly criticized by contemporaries as an ardent proponent of the atomic hypothesis. While letters written by his friends and family suggest that the physicist suffered from bi-polar disorder [26], one cannot help but lament that Boltzmann died by his own hand in 1906, a mere 2 years prior to his intellectual vindication by Perrin's experiments.

protocol[5]. The term $\boldsymbol{\xi}$ is the random force that describes the thermal noise due to the surrounding fluid. In the simplest case, this noise is written as a zero-mean, delta-correlated Gaussian process, such that [29]

$$\langle \xi_i(t) \rangle = 0; \quad \langle \xi_i(t)\xi_j(t') \rangle = 2D\delta_{ij}\delta(t-t'). \tag{1.23}$$

The coefficient in front of the Dirac-delta function ensures that Equation 1.19 is obeyed when the system is in equilibrium, i.e. $\mathbf{f} = 0$.

Sekimoto was the first to suggest that Langevin dynamics can be given a thermodynamic interpretation by application of the First Law of Thermodynamics, Equation 1.8, to individual trajectories [30]. The work performed on the particle is the sum of the work done to change the potential via λ, and the work done against the non-conservative force[6]

$$đW = \frac{\partial V}{\partial \lambda}\,\mathrm{d}\lambda + \mathbf{f} \circ \mathrm{d}x\,. \tag{1.24}$$

The heat can be identified as simply the difference between the total change in potential energy and the amount of work

$$đQ = \mathrm{d}V - đW = -\mathbf{F} \circ \mathrm{d}x\,, \tag{1.25}$$

where the negative sign indicates that this heat is dissipated into the environment, which is a result of a choice of convention of what to call positive heat flow. For the sake of clarity, we will drop this minus sign in the following, defining positive heat

---

[5] For example, the protocol could describe the motion of a harmonic trap with stiffness k, $V(x,\lambda(t)) = \frac{1}{2}k(x-\lambda(t))^2$, or it could describe the changing of the stiffness, $V(x,\lambda(t)) = \frac{1}{2}(k-\lambda(t))x^2$.

[6] The stochastic nature of the trajectories introduces a subtlety in taking the integral of $\mathbf{f} \circ \mathrm{d}x$. This arises arises because the definition of the Riemann–Stieltjes integral, which assumes that a function approaches a single value as the discretization width vanishes. However, $\boldsymbol{\xi}$ prevents this limit from being reached, necessitating a prescription for how to discretize the random force [29]. Here, we have used $\circ$ to indicate that we will use the mid-point, or Stratonovich, discretization scheme. This allows one to use the regular rule of calculus and is used for the rest of this work.

flow as an outflow from the system to the environment.

Now, each segment of a trajectory, $\mathrm{d}\mathbf{x}$, is associated with an amount of work performed on the particle and an amount of heat dissipated into the environment. The total work and heat are therefore functionals of the trajectory, given as

$$W[\mathbf{x}(t)] = \int\limits_0^t \mathrm{d}\tau \left[\frac{\partial V}{\partial \lambda}\frac{\partial \lambda}{\partial \tau} + \mathbf{f} \circ \frac{\partial x}{\partial \tau}\right] \tag{1.26}$$

$$Q[\mathbf{x}(t)] = \int\limits_0^t \mathrm{d}\tau \, \mathbf{F} \circ \frac{\partial \mathbf{x}}{\partial \tau} \tag{1.27}$$

The total change in the entropy of the environment can also be identified using the heat functional and the usual relationship between the heat and entropy, $S_{\text{env}}[\mathbf{x}(t)] = Q[\mathbf{x}(t)]/T$. For systems in a non-equilibrium steady state, the mean entropy production rate is well-defined and, in this case, is given by

$$T\dot{S}_{\text{env}} = \langle F\dot{x}\rangle \tag{1.28}$$

Fluctuation theorems

At the microscopic scale, entropy itself is a stochastic quantity, dependent on a particular realization of the stochastic trajectory $\mathbf{x}(t)$. This implies that a non-equilibrium process may lead to a *negative* change in the entropy. While this may appear to violate the Second Law, it is important to note that macroscopic thermodynamics only refers to averages in large systems and ignores fluctuations. Perhaps surprisingly, the fluctuations induced by the heat bath obey precise statistical laws themselves. In microscopic systems, the probability distribution for functionals such as $W[\mathbf{x}(t)]$ and $S[\mathbf{x}, t]$ obey *fluctuation theorems.* The “detailed fluctuation theorem” for a path dependent quantity ω takes the form [31]

$$\frac{P(\omega)}{\widetilde{P}(-\omega)} = \exp(\omega) \tag{1.29}$$

where $\widetilde{P}$ is the distribution under some conjugate dynamics, typically time-reversal. This implies the "integral fluctuation theorem" [32]

$$\langle \exp(\omega) \rangle = 1 \tag{1.30}$$

The most famous example is the Jarzynski equality, which identifies ω with work [33]. Beginning and ending in equilibrium distributions with free energy difference ΔF, the amount of work done in transitioning between the initial and final states will obey the following equality:

$$\langle \exp(-\beta W) \rangle = \exp(-\beta \Delta F), \tag{1.31}$$

where $\langle \rangle$ is an ensemble average taken over many instanaces of the same procedure. Thus, a non-linear averaging of a non-equilibrium quantity, W, allows one to recover an equilibrium quantity, ΔF [34]. This requires that some individual realizations obey $W < 0$, but Jensen's inequality ensures $\langle W \rangle \geq \Delta F$, as required in macroscopic thermodynamics.

1.2.2 Fokker-Planck equation and phase space fluxes

While the Langevin equation describes the equation of motion for a single Brownian particle, one could also ask how an ensemble of Brownian particles evolve in time. More precisely, can we predict how likely we are to find a Brownian particle at a position $\mathbf{x}$ after evolving for a time t, given that it started at the origin? The Fokker-

Planck equation describes the temporal evolution of precisely our quantity of interest, the probability distribution function, or phase space density, for the position over time, $\rho(\mathbf{x}, t)$. Given a Langevin equation, Equation 1.22, the corresponding Fokker-Planck Equation is [35]

$$\frac{\partial \rho(x(t), t)}{\partial t} = \boldsymbol{\nabla} \cdot \left(\gamma^{-1} \mathbf{F} \rho - D \nabla \rho\right). \tag{1.32}$$

The Fokker-Planck equation has the form of a conservation law, $\partial_t \rho + \boldsymbol{\nabla} \cdot \mathbf{J} = 0$, where the current is given by

$$\mathbf{J} = \gamma^{-1} \mathbf{F} \rho - D \nabla \rho. \tag{1.33}$$

One can further identify a phase space velocity $\mathbf{v} = \mathbf{J}/\rho$. The simplest Fokker-Planck equation is the case with $\mathbf{F} = 0$, which reduces to the diffusion equation, $\partial_t \rho = D \nabla^2 \rho$. The Fokker-Planck equation is a generalization of Liouville's theorem, which states that the phase space density is conserved under Hamiltonian dynamics, to stochastic trajectories containing dissipative terms.

With an expression for the evolution of ρ, one can identify an entropy associated with the evolving phase space density. The "stochastic entropy" measures the change in entropy of the system, not the environment [32],

$$S_{\mathrm{sys}}[x(t)] = -k_{\mathrm{B}} \ln \rho(x(t), t) \tag{1.34}$$

This is simply the quantity that gets averaged over in the Gibbs entropy, Equation 1.14. The total entropy production is the sum of the contributions from the system and the environment, $S_{\mathrm{tot}} = S_{\mathrm{env}} + S_{\mathrm{sys}}$. Taking the time derivative of Equation 1.34, in combination with Equations 1.33 & 1.28, gives the mean total entropy production rate

$$\left\langle \dot{S} \right\rangle_{\text{tot}} = k_{\text{B}} \int \mathrm{d}\mathbf{x}\, \frac{\mathbf{J} \cdot \mathbf{J}}{D\rho(\mathbf{x}, t)} = k_{\text{B}} \frac{\langle \mathbf{v} \cdot \mathbf{v} \rangle}{D}. \tag{1.35}$$

Like in Onsager's formulation of linear irreversible processes, we see that $\dot{S}$ is a positive definite, quadratic form of a current. Here, the current occurs in phase space. With a steady state, the evolution of ρ ceases, and the Fokker-Planck equation tells us that $\boldsymbol{\nabla} \cdot \mathbf{J} = 0$. In equilibrium, all currents are identically 0. However, in a NESS, $\mathbf{J} \neq 0$, requiring the current to be purely circulatory [36].

1.2.3 Path integrals and irreversibility

Rather than attempting to describe the evolution of $\rho(\mathbf{x}(t), t)$, one may instead be interested in the probability of observing a particular trajectory. The approach for this description of stochastic dynamics uses techniques from statistical field theory to use a path integral for stochastic processes [37, 38]. The path probability functional of observing a path $\mathbf{x}(t)$ is obtained by writing the expression for the Gaussian distribution for the white noise in a Langevin equation, and performing a change of variables, giving

$$P[\mathbf{x}(t)] = \frac{1}{Z} \exp(-\mathcal{A}[\mathbf{x}(t)]) \tag{1.36}$$

where Z is a normalization constant and $\mathcal{A}$ is the "action" associated with the trajectory [39],

$$\mathcal{A}[\mathbf{x}(t)] = \int_0^t \mathrm{d}\tau \left[\frac{1}{4D} \left(\gamma \frac{\partial \mathbf{x}}{\partial \tau} - \mathbf{F} \right)^2 + \frac{1}{2\gamma} \boldsymbol{\nabla} \cdot \mathbf{F} \right]. \tag{1.37}$$

The last term in the action results from the Jacobian when performing the change of variables and is symmetric under time-reversal.

The total entropy produced along a trajectory is related to the difference between observing a path forward in time up to a total time t, $\mathbf{x}(\tau)$, compared to the probability of observing the reverse path $\mathbf{x}(t-\tau) = \widetilde{\mathbf{x}}(\tau)$. As stated previously, irreversibility necessitates a production of entropy. This becomes explicit when writing the total entropy produced along a trajectory as [40]

$$\Delta S = k_{\mathrm{B}} \ln \frac{P[\mathbf{x}]}{P[\widetilde{\mathbf{x}}]} = k_{\mathrm{B}} \left(\mathcal{A}[\widetilde{\mathbf{x}}] - \mathcal{A}[\mathbf{x}] \right). \tag{1.38}$$

This equates the entropy produced to the portion of the action $\mathcal{A}$ that is asymmetric under time-reversal.

Taking the average of this quantity over the probability of the forward trajectories and finding it's slope gives an expression for the mean entropy production rate [41, 42, 43]

$$\left\langle \dot{S} \right\rangle = k_{\mathrm{B}} \lim_{t \to \infty} \frac{1}{t} \left\langle \ln \frac{P[\mathbf{x}]}{P[\widetilde{\mathbf{x}}]} \right\rangle_{P[\mathbf{x}]} = k_{\mathrm{B}} \lim_{t \to \infty} \frac{1}{t} D_{\mathrm{KL}}(P[\mathbf{x}] || P[\widetilde{\mathbf{x}}]). \tag{1.39}$$

$D_{\mathrm{KL}}(f(x)||g(x))$ is the Kullback-Leibler divergence, or the relative entropy, which measures the distinguishability between two probability distributions $f(x)$ and $g(x)$. D_{KL} is used throughout information theory and is defined as [44]

$$D_{\mathrm{KL}}(f(x)||g(x)) = \int \mathrm{d}x\, f(x) \ln \frac{f(x)}{g(x)}. \tag{1.40}$$

Remarkably, Equation 1.39 connects a thermodynamic quantity, entropy production which can presumably be measured using a thermometer, to an information theoretic quantity, D_{KL} which measures the statistical irreversibility of a trajectory. This exemplifies the deep connections between information and non-equilibrium thermodynamics [45].

1.2.4 Master equation and broken detailed balance

Our final description of stochastic dynamics is perhaps the simplest and most fundamental. While all our previous descriptions involved continuous degrees of freedom, one can also consider a system making random transitions between discrete states [46]. Examples include random walks on a lattice or chemical reaction networks. The evolution for the probability to be found in state n is governed by the Master Equation,

$$\frac{\partial p_n(t)}{\partial t} = \sum_m W_{nm} p_m(t) - W_{mn} p_n(t). \tag{1.41}$$

W is a matrix of transition rates whose elements W_{nm} give the rate of transitioning from state m to state n.

The Master Equation states that the total rate of change of the probability of occupying state n is the influx of probability from all other states m, $j_n^+ = \sum_m W_{nm} p_m$, minus the efflux to all other states m, $j_n^- = \sum_m W_{mn} p_n$. A system is said to obey detailed balance if the steady state solution obeys $j_n^+ = j_n^-$ for all states n. For chemical reactions that break detailed balance, the driving force is a chemical potential difference, $\Delta\mu$, related to the fluxes as [47]

$$\Delta\mu = k_{\mathrm{B}} T \sum_n \ln \frac{j_n^+}{j_n^-} \tag{1.42}$$

For systems obeying the first order kinetics given by Equation 1.41, Onsager's flux × force relationship for the entropy production rate remains valid arbitrarily far from equilibrium [48]. Here the total flux at state n is $j_n = j_n^+ - j_n^-$, and the entropy production rate is

$$\left\langle \dot{S} \right\rangle = k_{\mathrm{B}} \sum_n (j_n^+ - j_n^-) \ln \frac{j_n^+}{j_n^-}. \tag{1.43}$$

Much like Equation 1.39, this directly implicates irreversibility, via broken detailed balance, with entropy production. All other descriptions of stochastic dynamics can be derived as a limiting case of a Master Equation. For example, the diffusion equation arises from nearest neighbor hopping dynamics on a lattice. For this reason, non-equilibrium behavior seen in continuous variables often have their origins in the breaking of detailed balance at a smaller length scale. In living matter, this breaking of detailed balance often stems from a chemical reaction by name of ATP hydrolysis.

1.3 ATP and actomyosin dynamics

Adenosine triphosphate (ATP) is a molecule that all cells use to power the microscopic, protein-based machines that carry out vital life processes such as muscle contraction [49], DNA transcription into RNA [50], protein synthesis [51], and signal transduction [52]. By reacting with water, one of the three phosphate groups (P_i) in ATP is released to transform ATP into the lower energy adensine diphosphate (ADP), $ATP + H_2O \rightarrow ADP + P_i$. This hydrolysis reaction results in a free energy change on the order of 10 $k_\mathrm{B}T$ per ATP molecule in physiological conditions (BNID 101989)[7]. This process is then reversed by dedicated molecular machines called ATP synthases [54], which utilize proton gradients across a membrane to reattach phosphates to ATP to reform the higher energy ATP, maintaining a ratio of ATP/ADP $\sim$ 1000 (BNID 100773), establishing a chemical potential between ATP and ADP, $\Delta\mu_\mathrm{ATP}$. From $\Delta\mu_\mathrm{ATP}$ flows all of the behaviors exhibited by living matter[8].

A key question then becomes, how does this microscopic chemical driving translate into large scale dynamical and mechanical behaviors of living matter? Here, we

---

[7] When referring to numerical values in biology, rather than giving specific references, we will link to a BioNumber ID (BNID), which can be accessed at `https://bionumbers.hms.harvard.edu/`. BioNumbers is a public repository of quantitative measurements made throughout biology that provides sources and the experimental conditions used to attain the result [53].

[8] This is an oversimplification. Guanosine triphosphate (GTP) is vital for biopolymer stability [55] and signaling networks [56], and ion gradients power the recombination of ADP and P_i by ATP-synthase [57].

focus on the actin-myosin cytoskeleton, responsible for the production of mechanical forces that drive cell shape changes, cell division, and motility [58, 55, 59, 60]. The cytoskeleton comprises semiflexible protein polymers called *actin* [61], that are subject to forces driven by ATP hydrolysis by molecular motors called *myosin* [62]. Systems composed of actin and myosin have become protyptical examples of biological *active matter* [63, 64], defined as many-body systems where microscopic injections of energy lead to self-propulsion of the individual constituents. We take the cell cytoskeleton as a model system representing a more general class of living, active, adaptive matter [65], and try to expand the domain of our discussion and results where possible.

1.3.1 Active stress

Principal among the processes powered by $\Delta\mu_{\mathrm{ATP}}$ is the generation of forces by molecular motors embedded within the cell cytoskeleton. These enzymatically produced forces are termed “active stress”, as they arise purely from the consumption of ATP. Many phenomenological models exist for molecular motors [66], but they all result in net motion of a motor along a preferred direction on a structurally polarized cytoskeletal filament. When bound to two anti-parallel filaments, this walking results in forces that slide the filaments relative to each other. In a network of actin, myosin and other passive proteins can cross-link the polymers, propagating active stresses over length scales much larger than that of a single filament, leading to large scale fluctuations and flows of the network [67, 68, 4, 69].

In recent years, mixtures of purified proteins have provided a simplified system within which to study the non-equilibrium properties of actin networks [70, 71, 72]. Early examples include measuring violations of the fluctuation-dissipation theorem, Equation 1.21, for colloids embedded within a reconstituted actomyosin network [73]. By measuring $C(\omega)$ and $\widetilde{\chi}$ independently using two separate techniques, the authors inferred the distance from equilibrium the violation of the equilibrium fluctuation-dissipation theorem. This is tightly related to the idea of a frequency dependent "effective temperature", which has been used in other biological [74] and non-biological [75] contexts as a measure of a distance from equilibrium, defined as

$$T_{\text{eff}} = \frac{\omega C(\omega)}{2k_{\text{B}}\widetilde{\chi}(\omega)}. \tag{1.44}$$

Despite the simplicity of this approach, the use of T_{eff} remains controversial – for example, T_{eff} can become negative [74] while some non-equilibrium systems can be mapped to an apparent equilibrium system that obeys a fluctuation-dissipation theorem [76].

Recent efforts have focused instead on measuring entropy production as a measure for how far biopolymer systems are from equilibrium. In particular, these techniques use the bending fluctuations of exogenous probe filaments embedded within a cross-linked network as a probe for non-equilibrium activity [72, 77, 78, 79]. These approaches have used the identification of phase space circulation, the basis for the Fokker-Planck entropy production rate in Equation 1.35.

While providing a more rigorous metric determining whether a system in or out of equilibrium, these previous works only detect the presence of phase space circulations, making a binary determination of whether the system is in equilibrium or not. Furthermore, they do not tie the non-equilibrium behaviors to any biologically relevant outcomes. For example, while myosin activity seems to always lead to flow in experiments of purified proteins, the cell cortex, a thin shell of actomyosin just inside of the cell membrane, endows cells with surface tension that increases with myosin motor activity [80]. How can we reconcile these two views of myosin activity?

In Chapter 2, we extend these methods of measuring phase space fluxes to provide the first quantitative measurement of the entropy produced in a living system at different levels of activity. We find that the entropy production rate of filament fluctuations is maximized in the mechanically stable state, and use it to identify a new class of interactions between actin and myosin. This work thus unifies the two effects myosin has on actin networks, inducing stability and flow, along the single axis spanned by phase space fluxes.

1.3.2 Mechanosensitive binding kinetics

Living matter not only produces forces, but also responds to them. Many biological proteins are *mechanosensitive*, altering their behavior in response to an applied force [81]. An important class of mechanosensitive proteins are involved in binding and adhesion. Cells dynamically regulate adhesion proteins to regulate cell migration and maintain tissue integrity by coupling the actin cytoskeleton to extracellular substrates or to other cells, respectively [82]. Adding another level of complexity, cross-linking proteins within the actin cytoskeleton are also mechanosensitive, including that myosin motors that are the origin of active stress.

While most engineered materials contain bonds that weaken under load, mechanosensitive biological bonds such as myosin and the actin cross-linker α-actinin, strengthen under load. They decrease their unbinding rate in response to force [83, 84]. Bonds with this characteristics are known as “catch bonds” [85, 86]. This brings new questions into the role of myosin motors in the remodeling of the actin network. The actin cytoskeleton reorganizes itself rapidly due to myosin stresses [87], with evidence pointing towards myosin-driven rearrangement and detachment of bonds towards a critical point in the network connectivity that leads to an increased flow of actin [88]. However, the ability of active stress to strengthen and solidify an actin network, as seen in engineered polymer networks containing synthetic biomimentic catch bonds [89, 90], has remained unexplored.

In Chapter 3, we address these questions using simulations of actomyosin networks while explicitly calculating the irreversibility due to binding using a variant of the measure of irreversibility for discrete dynamics obeying a Master equation, Equation 1.43. We find that weak catch bonds lead to an increase in network fluidity without much change in binding irreversibility. Beyond a threshold in the strength of the catch bond, the actomyosin network transitions to a solid-like state where the binding irreversibility changes rapidly. Thus, while the work of in Chapter 2 studied the role of actin filament fluctuations in transitions from a stable to a flowing state, here we find a novel role for myosin binding in driving a similar dynamical and mechanical transition.

1.3.3 Assembly and disassembly

One of the most striking characteristics of living matter is its ability to dynamically assemble and disassemble many of its components reliably while maintaining structural stability. For example, actin filaments can polymerize up to a rate of 10 μm$/s$ (BNID 111090), the length scale of a eukaryotic cell, but maintain a length on the order of 100 nm inside of cells (BNID 109294). The assembly and disassembly of actin filaments can occur in many ways [59]. One is polymerization and depolymerization, each of which occurs at a preferred end of an actin filament as a function of the phosphorylation state of the actin monomers. Polymerization dynamics leads to actin treadmilling, an important factor in cell motility [61]. Another mode of (dis)assemby is the breaking of actin filaments due to myosin induced stresses [71] or actin binding proteins that induce severing [91].

At large length scales, these (dis)assembly dynamics can appear to induce diffusive behavior. When coupled to other regulatory proteins in the cell, a reasonable description of the process is that of multi-species reaction-diffusion [92]. In general, reaction-diffusion equations have the form [93]

$$\frac{\partial \rho_i(\mathbf{x}, t)}{\partial t} = D_i \nabla^2 \rho_i + f_i(\{\rho_j\}), \tag{1.45}$$

where $\rho_i(\mathbf{x}, t)$ is the chemical concentration of species i across space and time, D_i is the diffusion constant of species i, and $f_i(\{\rho_j\})$ is a possibly non-linear function that describes the reactions that species i is subject to due to all other chemical species in the system.

Alan Turing proved that these reaction-diffusion systems are capable of establishing static, spatial patterns that are known today as Turing patterns [94]. Since this pioneering work, reaction-diffusion systems have been found to also induce dynamic patterns such as oscillations, waves, and excitability [95]. Such spatiotemporal dynamics are critical to biological processes such as cell division, signal transduction, and migration [96]. While much work has focused on understanding reaction-diffusion system dynamics alone, only recently has work turned towards the energetics behind these non-equilibrium patterns [97, 98]. However, while work on individual models has progressed, general tools are lacking.

In Chapter 4, we introduce a general method for estimating irreversibility directly from data of spatiotemporal dynamics using the path integral formulation of the entropy production rate, Equation 1.39. Our work not only provides a way to measure the total irreversibility, but also introduces the *entropy production factor*, which quantifies irreversibility for every time and length scale in the system. By analyzing simulations of a 1-dimensional reaction-diffusion oscillator, we find signatures of the dynamical phase transition that marks the onset of oscillations in the total irreversibility, but signatures of the separate transition towards synchronization are found in the entropy production factor. This work will allow researchers to probe previously inaccessible degrees of freedom, providing new insight into the energetic origins of the non-equilibrium, spatiotemporal patterns found throughout biology.

Chapter 2

Energetics of mechanical stability

2.1 Motivation

The actomyosin cytoskeleton exerts contractile stresses in order to drive shape change and motion across length scales to regulate diverse physiological processes. It generates the forces required for cell division by the cytokinetic ring [99], it coordinates contractility and focal adhesion dynamics to drive cell migration [82], and creates forces that guide the formation of multicellular tissues during morphogenesis [100]. These contractile forces are the result of myosin molecular motors hydrolyzing ATP and walking along multiple F-actin polymers that it is connected to, as first illustrated in muscle cells [49, 101, 102]. Contractility induced flows are also seen in reconstitution experiments, where actin and myosin are purified from a cell and deposited onto a substrate within a buffer that contains ATP to activate the molecular motors [103, 67, 6, 4].

Antagonistic to actomyosin's propensity to flow is its role in maintaining structural stability for the cell. The rheological properties of cells stem from the properties of the actin cytoskeleton, resulting in remarkably consistent scaling laws for the cell's elastic and viscous properties under a wide range of time scales and perturbations

[104]. Further, diseases such as cancer are correlated with qualitatively distinct rheological properties [105]. Understanding the mechanism by which actomyosin produces stable states would therefore provides an understanding of the design principles that biological matter uses to balance the need to maintain mechanical stability while preserving the ability to flow in response to an external or internal signal. Further complicating the matter is that the constituents of the cytoskeleton are subject to thermal fluctuations and persistently turning over.

In this chapter, I analyze experimental data gathered in the Murrell Lab in order to measure entropy production rates in actin filament motions by myosin-induced stresses, quantitatively establishing that an active stable state dissipates the most energy due to non-equilibrium forces. We further uncover the molecular interaction between myosin and actin that leads to this maximal energy dissipate rate that we term “plucking” by myosin motors. When a myosin motor plucks an actin filament, it produces large bends but does not result in center-of-mass transport, allowing myosin stresses to be dissipated without rearranging the entire network.

My contribution to this work comprises the implementation of the entropy production rate, bending energy, and velocity autocorrelation analyses, and interpretation of all results. The work presented here has been adapted from the following paper:

- **D.S. Seara**, V. Yadav, I. Linsmeier, A.P. Tabatabai, P.W. Oakes, S.M. Ali Tabei, S. Banerjee, and M.P. Murrell. Entropy production rate is maximized in non-contractile actomyosin. *Nature Communications*, 9, 4948 (2018).

2.2 Introduction

The eukaryotic cytoskeleton is an active, viscoelastic material that exhibits a wide range of dynamic responses to both its internal and external environment, such as polarizing contractile flows during embryonic development [106, 107] and cell division in the adult [108]. By contrast, there are dynamic steady states that do not result in flows, including ratcheting in the *Drosophila* wing [109], excitable wave patterns in the *Xenopus laevis* oocyte [110], and fluctuations in the mitotic spindle [111]. It is generally accepted that the driving force for many of these processes originate from both filament turnover and the relative sliding between molecular motors and cytoskeletal polymer along their long axis [49, 101, 102]. For example, reconstituted networks of microtubules that flow under the influence of kinesins [112, 113], allowing microtubule networks to retain their density and structural properties under the influence of extensile forces [111]. By contrast, actin networks activated by myosin molecular motors lead to filament buckling [71, 114] and severing at high curvatures [115, 5]. As a result, F-actin networks experience macroscopic architectural changes and large strains during destabilizing contractile flows [116, 117]. It remains unclear how networks of semi-flexible polymers can maintain a dynamic steady state in the presence of active stresses. More generally, the relationship between the out-of-equilibrium accumulation and dissipation of mechanical stresses and the stabilization of active materials is unknown.

In this work, we characterize the thermodynamic criteria for the maintenance of dynamic stability in an active biomimetic material composed of semi-flexible F-actin through determination of the rate of entropy production as a function of molecular motor activity. First, we systematically identify the range of motor activity that differentiates macroscopic contractility (unstable) from steady-state non-contractile behavior (stable). Next, we determine the effect of activity on the microscopic balance of mechanical work and the production of entropy from the myosin-induced bending of individual F-actin. This provides a quantitative relationship between how far the system is from equilibrium with its propensity to dissipate mechanical energy. We then correlate network and filament properties to associate the accumulation of mechanical work and the production of entropy with the mechanical stability of the bulk material. Finally, we compute the entropy produced in the actin network in time and per individual myosin filament and correlate the motions of myosin filaments with the bulk dissipation that stabilizes the material.

2.3 Results

2.3.1 F-actin self-assembles into a 2D nematically ordered network

Using previously described methods [6], solutions with purified filamentous (F) actin are crowded onto a lipid bilayer using methylcellulose on top of a glass slide, creating a quasi-2D synthetic model of a cellular cortex (Fig. 2.1a). In the absence of adhesion between the actin filaments and membrane, the filaments change their spatial orientation to establish a net direction upon reaching the membrane surface. This reorganization generates local domains of nematic alignment, quantified by the coarsgrained nematic order parameter, $q = 2\left\langle \cos^2\theta - 1/2 \right\rangle$ (Fig. 2.1a-d). The nematic domains originate from and terminate in regions of disorganized F-actin containing topological defects with charge $\pm 1/2$. $-1/2$ defects are formed by moderate F-actin bending in radial directions around a central void, whereas $+1/2$ defects form due to highly bent F-actin oriented along a single direction (Fig. 2.1e,f).

While the F-actin network exhibits the same defects and symmetries as a tradi-

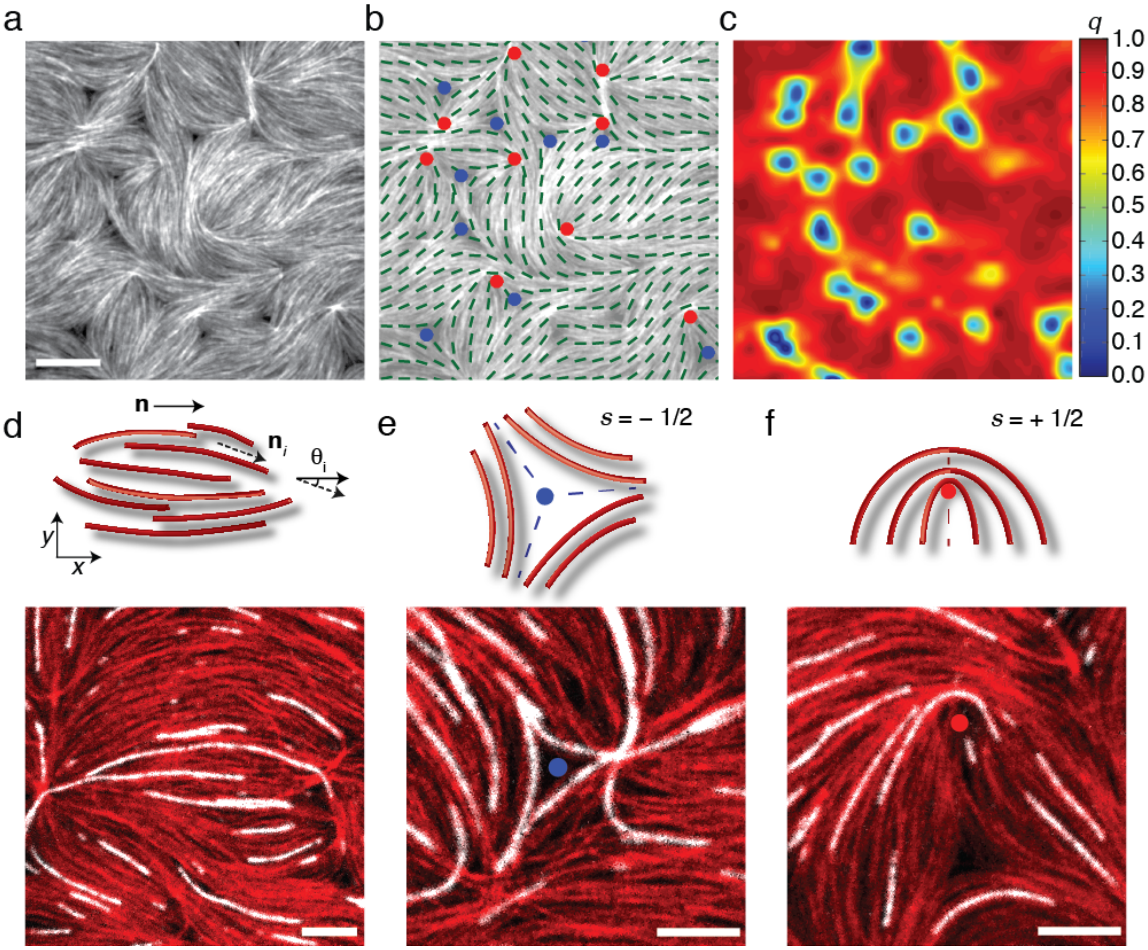

Figure 2.1: **Reconstituted actin cortex forms nematic domains.** (a) Image of crowded *in vitro* F-actin cortex. Scale bar is 10 μm. (b) Local nematic director field (green) overlaid on the same image as (a). Red and blue dots indicate the $+1/2$ and $-1/2$ topological defects, respectively. (c) Nematic order parameter field shown for the same image as (a). (d) (top) Schematic of a nematically ordered domain comprised of many actin filaments, where $\mathbf{n}$ is the nematic director of the entire domain, $\mathbf{n}_i$ is the local alignment of a single F-actin, and θ_i is the angle between them and (bottom) image of a single nematic domain. Both red and white show actin filaments labeled with different fluorophores, polymerized separately, and combined at a $1:50$ ratio prior to crowding to visualize individual filaments within the larger network. (e) Schematic (top) and image (bottom) of a 1/2 disclination defect and local nematic ordering in quasi 2D F-actin. (f) Schematic (top) and image (bottom) of a $+1/2$ disclination topological defect and local nematic ordering in quasi 2D F-actin network. Scale bars in (d–f) are 5 μm.

tional nematic liquid crystal composed of short, rigid rods [118], the average F-actin length in our experiments is $\sim 10\ \mu$m, comparable to their persistence length [119]. As a result, defects form due to bending and entanglement of individual actin filaments (Fig. 2.1e,f bottom). We do not observe defect motion or annihilation, reported in other biopolymer nematic liquid crystals [112, 113, 120, 121].

2.3.2 Myosin activity destabilizes nematic order in F-actin networks

Previous work in the Murrell lab showed that contractile flow occurs in a cooperative manner above a critical myosin thick filament density, ρ_c [4, 5]. For $\rho > \rho_\mathrm{c}$, filament buckling coincides with network contraction as it shortens the filament end-to-end length [122]. However, the impact of sub-contractile densities of myosin ($\rho < \rho_\mathrm{c}$) on the dynamics of F-actin is unclear. To this end, we compare and contrast the impact of activity on actomyosin network dynamics above and below ρ_c.

To assemble the actomoysin network, myosin dimers are added at $t = 0$, accumulating and forming myosin thick filaments within ~ 100 s. After the addition of myosin, we obtain the F-actin velocity field, $\mathbf{v}(\mathbf{r}, t)$, using particle image velocimetry [123] and define the macroscopic strain rate as its divergence, $\psi(t) = \langle \boldsymbol{\nabla} \cdot \mathbf{v} \rangle_\mathbf{r}$. We simultaneously quantify the F-actin network structure by the spatially averaged nematic order parameter, $\langle q \rangle_\mathbf{r}(t)$. For $\rho > \rho_\mathrm{c}$, ψ decreases during contraction until it reaches a maximum in its magnitude, ψ_max. $\langle q \rangle$ also decreases over time, representing a loss in F-actin alignment due to myosin activity. the decrease in $\langle q \rangle$ precedes the decrease in ψ, suggesting there may be dynamics of actomyosin ($\delta \langle q \rangle \neq 0$) that are non-contractile ($\psi \approx 0$) (Fig. 2.2a,b). For $\rho < \rho_\mathrm{c}$, ψ fluctuates around zero, although $\langle q \rangle$ still decreases by up to 30% of its original magnitude (Fig. 2.2c, d). This non-contractile state ($\psi \approx 0$) is observed experimentally for up to 1 h.

In summary, myosin activity can drive the establishment of a steady-state defined by changes in F-actin structure dynamics, absent contractile flows. As myosin is indeed active in the stable steady state, we asked how the stresses are being dissipated if they are not resulting in the flow of actin? To answer this question, we estimate energy dissipation using the tools of stochastic thermodynamics [12].

2.3.3 Activity-dependent dissipation is maximized in stable state

When driven out of equilibrium, microscopic systems obey fluctuation theorems that relate the irreversibilty of a process to the amount of entropy produced by that process [124, 32]. Myosin motors operate far from equilibrium by hydrolyzing ATP to generate forces on F-actin, as previously quantifed by devaition from teh fluctuation-dissipation theorem [73]. Here, we show that energy is dissipated by F-actin bending in the stable steady state defined above.

Using experiments where only 2% of filaments are fluorescently labeled, individual filaments are tracked over time (Fig. 2.3a). Filament shape is specified by its tangent angle along its arc length at each time, $\theta(s,t)$ (Fig. 2.3b). This function is decomposed into a set of orthogonal bending modes [125], $\theta(s,t) = \sum_q a_q(t) f_q(s)$ (Fig. 2.3c), see Appendix A.2). Filament dynamics are represented by the trajectory of a point in a phase space spanned by the mode coefficients, $\mathbf{a}(t) = (a_1(t), a_2(t), \ldots)$ (Fig. 2.3d). Such phase space trajectories have been used to identify broken detailed balance in mesoscopic biological systems via circulation within the phase space, a signature of broken detailed balance[77, 78, 79].

We extend these previous works by not only identifying a non-equilibrium state, but by quantifying how far from equilibrium the state is by measuring the entropy produced using the phase space trajectories of $\mathbf{a}(t)$, using a formulation based on a

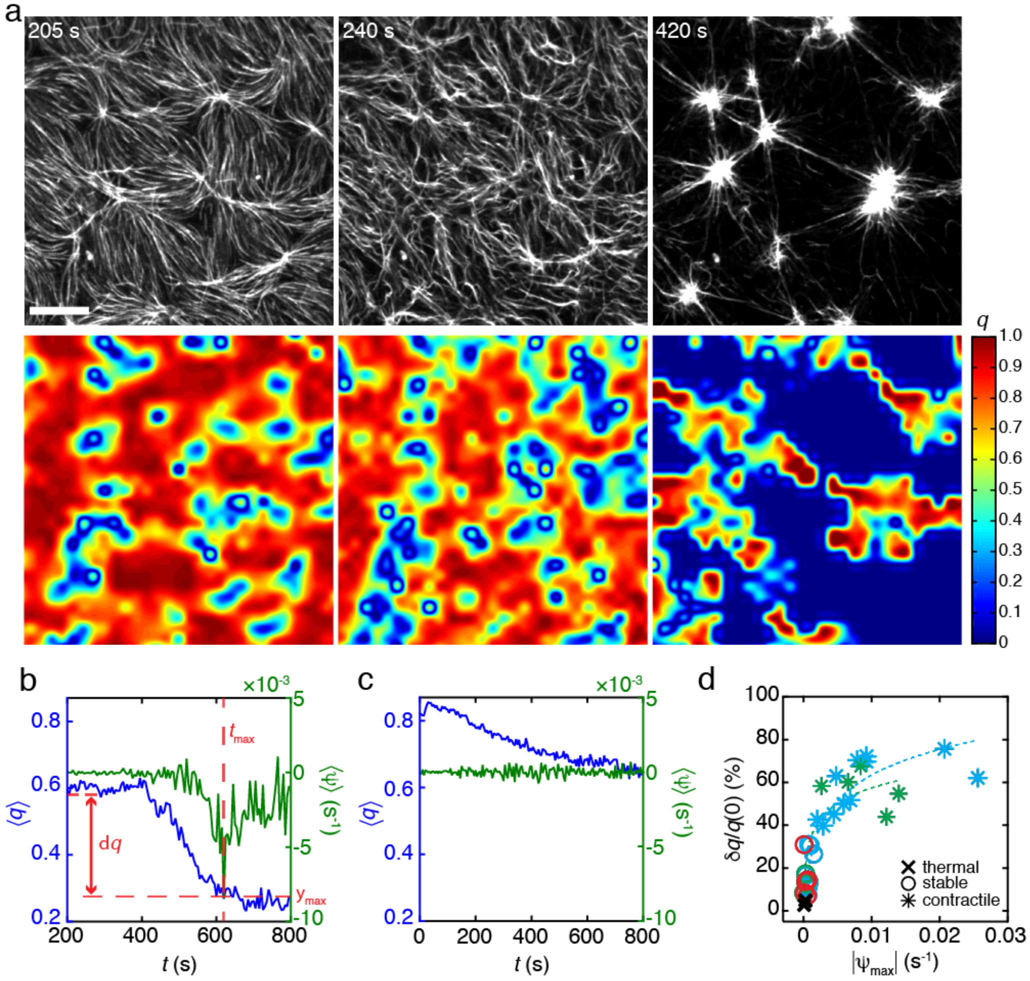

Figure 2.2: **Myosin density affects F-actin nematic order in both contractile and stable states** (a) (top) Fluorescent F-actin network undergoing contraction. Scale bar is $10\mu m$. (bottom) Heat map of scalar nematic order parameter, q. Myosin dimer added at $t = 0$. (b) Spatially averaged F-actin nematic order parameter measured ($\langle q \rangle$, blue) and F-actin strain rate (ψ, green) 200 seconds after the onset of myosin addition when $\rho > \rho_c$. Time of maximum magnitude of divergence ($t_{\max}$) indicated by vertical dotted red line. Difference between nematic order at $t = 0$ and at time of maximum divergence ($\delta q = q(0) - q(t_{\max})$) indicated by horizontal dotted red line. (c) Spatially averaged nematic order (blue) and strain rate (green) for a stable actomyosin network, $\rho < \rho_c$ where myosin is added at t = 0. (d) Percent change in nematic order ($\delta q / q(0)$) for thermal ($\times$), stable ($\circ$), and contractile ($*$) network states. The marker color denotes the myosin isoform added to each experiment (SkMM= blue, SmMM = green, NMM = red, no myosin = black). We define non-contractile, stable (S) networks as those with $\psi_{\max} < \psi_c = 2 \times 10^{-3} s^{-1}$, contractile networks (C) for $\psi_{\max} > \psi_c$, and networks for which no myosin added as thermal networks (T).

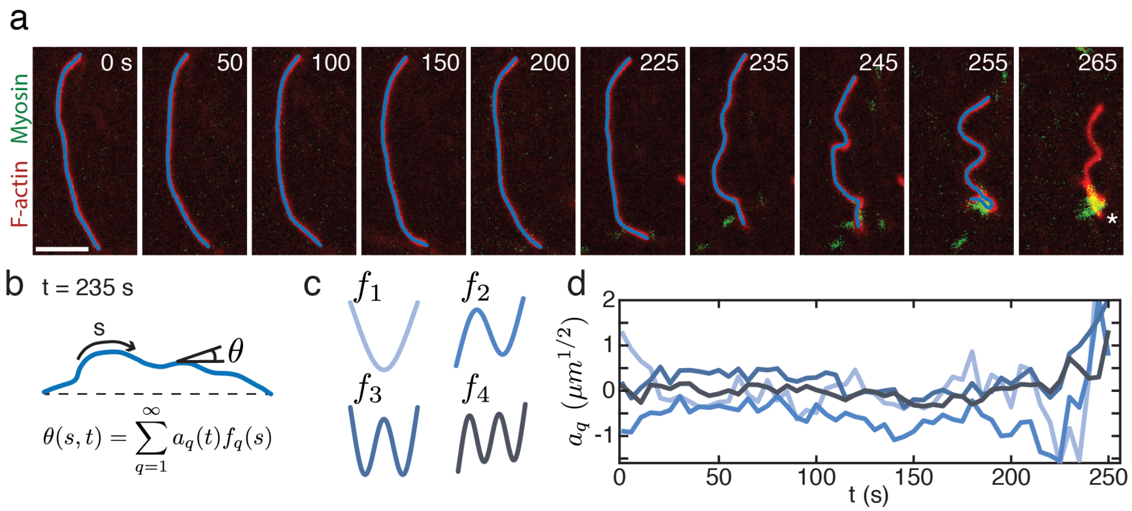

Figure 2.3: **Quantification of filament bending modes** (a) Example of experiment with 2% labeled filaments (red) as myosin accumulates (green). Filaments are tracked (blue line) until a severing event, indicated by white asterisk. Scale bar is $4\mu m$. (b) Illustration of normal mode analysis done on filament traces at each time point. The tangent angle, θ, is found along the arc length, s, of the filament at each time, t. These functions are then decomposed into a set of orthogonal normal modes, $f_q(s)$, whose coefficients $a_q(t)$ are tracked in time. (b) First four normal modes. (c) Time series of first four normal modes for the filament shown in (a).

Langevin equation for the bending modes [126] (see Appendix A.3). Using natural units, the total entropy produced up to a time t is given by

$$\Delta S(t) = \int_0^t \mathrm{d}\tau \, \dot{\mathbf{a}}^T(\tau)\mathbf{D}^{-1}\mathbf{v}^{\mathrm{ss}}[\mathbf{a}(\tau)] \tag{2.1}$$

where $\mathbf{v}^{\mathrm{ss}}[\mathbf{a}(\tau)]$ is the steady state phase space velocity estimated using the entire trajectory, and $\dot{\mathbf{a}}(\tau)$ is the instantaneous phase space velocity. $\mathbf{D}$ is the diffusion matrix that enters the Fokker-Planck equation associated with the underlying Langevin equation for the mode amplitudes. For simplicity, we estimate $\mathbf{D}$ from the drag coefficients of a slender rod [127]. We verify our calculations and approximations by checking that a control system obeys the detailed fluctuation theorem [128] (see Appendix A.4).

Using the above formalism, we measure the total energy dissipated per unit filament length as $\overline{\Delta s}(t)T$, where T is the temperature of the surrounding medium, $\Delta s = \Delta S(t)/L$ with L the filament length, and the bar denotes an ensemble average taken across filaments at each time point. We find that the actomyosin system shows three distinct phases of energy dissipation that correspond to the three phases of actomyosin in Fig. 2.2d. In these experiments, myosin accumulates over time and the three states coincide with changes in the number of tracked myosin thick filaments over time. The first state is a passive state distinct from thermal states due to the presence of myosin dimers that have not yet formed myosin thick filaments (S_0). The second is an active, non-contractile state as myosin thick filaments begin to appear (S_1). The third is the contractile state (C) where myosin thick filaments begin to aggregate and thus the number of tracked thick filaments decreases (Fig. 2.4a, black). Although an individual experiment will be in each state over time, we assume the system to be in a steady state due to the fact that the transition to the contractile state occurs at the same myosin concentration as found in experiments with fixed myosin concentration [4].

State S_0 shows a small increase in energy dissipated, followed by a large increase in the rate of energy dissipation during state S_1. State C shows a decreased energy dissipation rate (Fig. 2.4b). Within state S_1, total energy dissipation as a function of myosin number density across experiments collapses along a single curve until the system gets close to the contractile regime, indicating that myosin filaments dissipate energy uniformly below a number density, beyond which they do not behave identically (Fig. 2.4c). These results are replicated using agent-based simulations using Cytosim [129] (Fig. 2.4, insets).

Having investigated the role that activity plays in dissipating mechanical energy, we next sought to understand how activity also stores mechanical energy in the system via filament bending. To this end, we measured the change in bending energy per unit filament length as myosin accumulates, $\overline{\Delta\varepsilon_{bend}} = \overline{\Delta E_{bend}/L}$ (Fig 2.4d). The bending energy is given by

$$E_{bend} = \frac{EI}{2}\int_0^L \kappa^2(s)\,\mathrm{d}s\,, \tag{2.2}$$

where $\kappa(s)$ is the local filament curvature and EI is the flexural rigidity of a thin rod [119]. As with the dissipation energy, we take the ensemble average across filaments at each time point. We again see three distinct regimes, where the actin bending energy does not change during state S_0 and increases rapidly in state S_1 (Fig 2.4d). In state C, bending energies are elevated but decreasing nominally. This may be attributed to filament severing [71], although it is not necessary as simulations without severing show similar results (Fig 2.4 d,e, insets). In simulation, it can be observed that upon the cessation of contractile flow, filaments are polarity sorted with motors at filament barbed ends and bends are released. Again, plotting bending energy as a function of myosin number density in state S_1 collapses experiments along a single curve as the system approaches contractility (Fig 2.4f).

In summary, the non-contractile state (S) dissipates the most energy per unit time as measured through the rate of entropy production of filament bending modes. As the stable and contractile states have different entropy production rates, we sought to determine if there was a difference in the underlying actomyosin interactions that produce these rates.

2.3.4 Transverse actomyosin motions underlie maximal dissipation

Active transverse fluctuations and F-actin bending may suggest that myosin and F-actin are not aligned, in contrast to the canonical model for their interaction of anti-parallel filament sliding. To explore this, we quantify the extent of axial vs. perpendicular actin motions and compare them to myosin motions.

To quantify the extent to which non-contractile networks exhibit perpendicular bending motions, we measure an anisotropic velocity autocorrelation function, defined as (see Appendix A.5)

$$\delta C_{vv} = \left\langle \frac{C^{\perp}_{vv}(r,t)}{C^{\perp}_{vv}(0,t)} \right\rangle_t - \left\langle \frac{C^{\parallel}_{vv}(r,t)}{C^{\parallel}_{vv}(0,t)} \right\rangle_t . \tag{2.3}$$

Positive values indicate enhanced perpendicular fluctuation autocorrelations; negative values indicate enhanced parallel fluctuation autocorrelations. We find that all stable systems, regardless of myosin isoform, exhibit greater fluctuations perpendicular to the filament axis. This stands in stark contrast with contractile systems that show larger autocorrelations parallel to the filament's axis as would be expected for

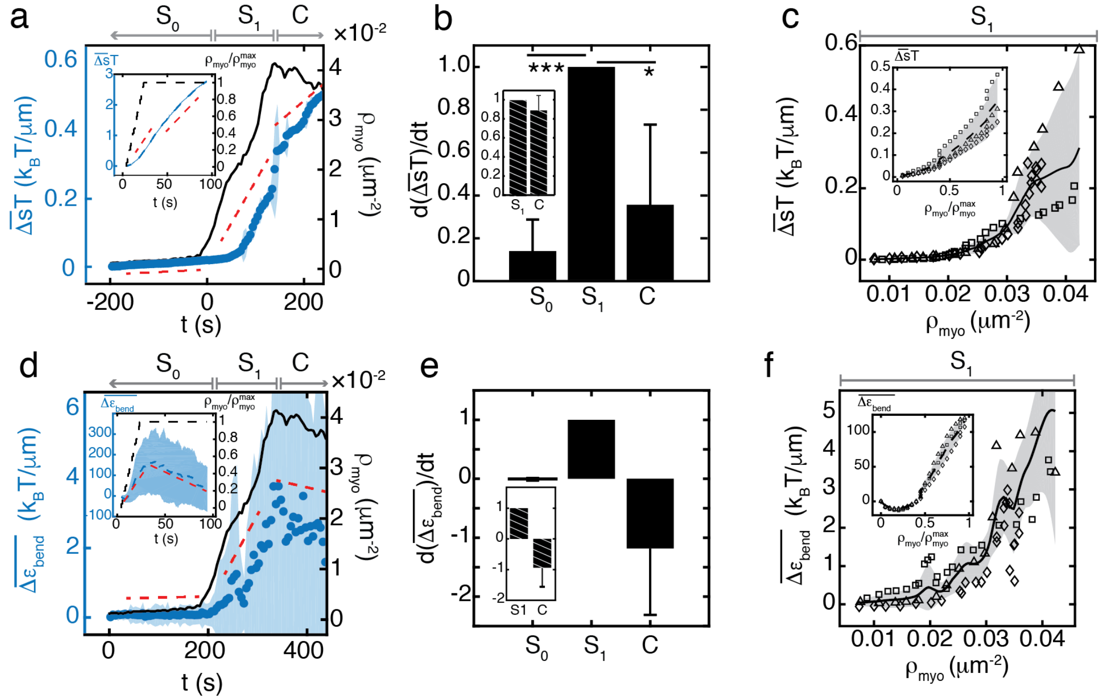

Figure 2.4: **Dissipation and storage of energy in actomyosin** (a) Ensemble averaged energy dissipated per unit length, $\overline{\Delta s}T$, as a function of time (blue) and number density of myosin thick filaments counted as a function of time (black). Blue dots and shaded areas are mean ± standard deviation of $n = 19$ filaments tracked in a single experiment. Experiment is broken into three phases, S_0, S_1, and C. Red dashed lines indicate slopes measured in each state. (b) Means ± standard deviation for slopes of entropy in states S_0, S_1, and C for $n = 4$ experiments. Each experiments slope is normalized to the slope of S1 in that experiment. $p < 10^{-4}$ between slopes S_0 and S_1, and $p = 0.014$ between slopes S_1 and C. (c) Dissipation energy density as a function of myosin number density in state S_1 for $n = 3$ experiments, indicated by different symbols. Black line and shaded area are mean standard deviation across experiments. (d) Similar to (a), but showing filament bending energy per unit length, $\overline{\Delta\varepsilon_{\mathrm{bend}}}$, in blue. (e) Similar to (b), but for filament bending energy slopes. $p < 10^{-5}$ between slopes S_0 and S_1, and $p = 0.001$ between slopes S_1 and C. (f) Similar to (c) but for filament bending energy. All insets for b-g show recapitulation of data in main figure by agent-based simulations for $n = 3$ simulations. In the simulations, there is no S_0 phase because myosin is added immediately at $t = 0$.

sarcomeric contraction [49, 101] (Fig. 2.5a, b). We name these reversible, myosin-derived transverse fluctuations “plucking”.

Using a light-activation assay [4] with skeletal muscle myosin II (SkMM), contractility is induced at a constant myosin density. 405 nm light inactivates blebbistatin, an ATPase inhibitor, thereby activated myosin in the area of illumination. During contraction, we measure the relative angle between SkMM thick filaments and the actin it decorates (Fig. 2.5c). The extend of contractility is measured by an increase in the strain rate, ψ. We find that as the magnitude of ψ increases, we see a rapid change in the relative angle betwen actin and myosin (Fig. 2.5d). As a result, we attribute the enhanced perpendicular fluctuations of actin in a non-contractile state, and therefore the enhanced entropy production rate, to the variation in the relative angles between individual myosin thick filament assemblies and F-actin. This indicates that the total “activity”, ζ, in actomyosin networks depends not only on the myosin density, ρ, but also on the relative angle between the motors and filaments, θ, i.e. $\zeta = \zeta(\rho, \theta)$.

2.4 Conclusion

By engineering an active biomimetic cortex, we identify a structurally dynamic phase of actomyosin absent of contractile flow or filament turnover at an intermediate level of activity. We quantify the entropy production rate, a metric for a system’s distance from equilibrium [12] and the extent to which energy is dissipated. As bending energies increase immediately upon sequential addition of individual myosin thick filaments, and the density of myosin that marks the onset of the contractile state is the same for experiments done over time as done across separate experiments, we assume the system to equilibrate quickly and therefore apply a steady state framework. Unexpectedly, we find that the rate of entropy production is non-monotonic

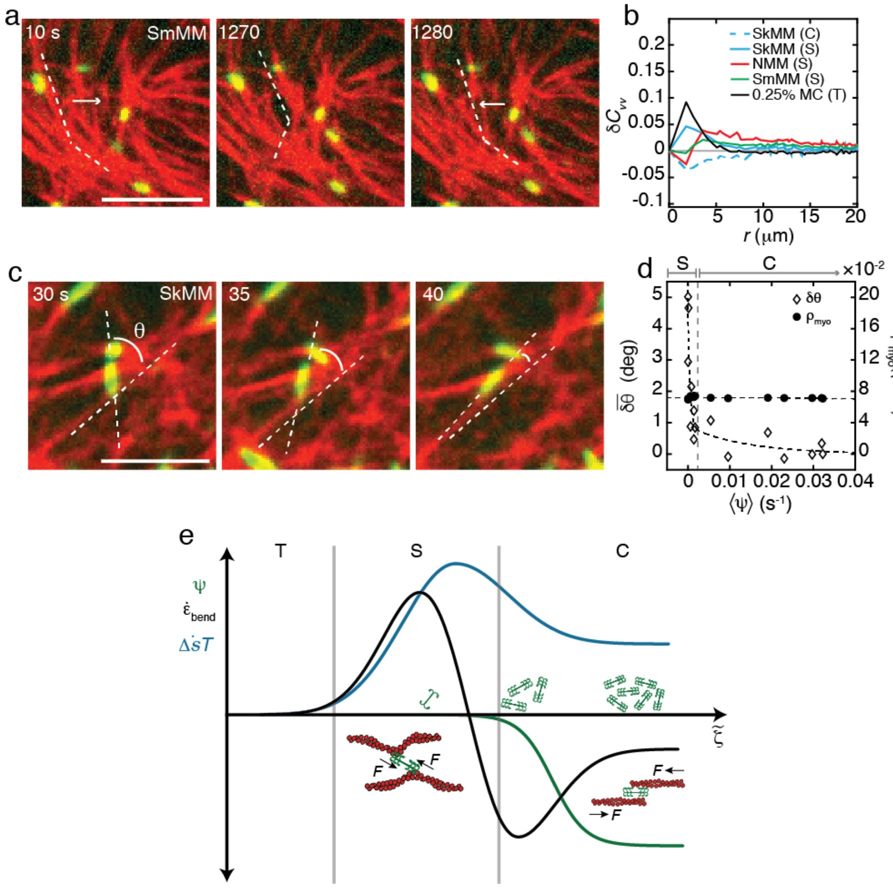

Figure 2.5: **Misaligned myosin plucks F-actin in stable state** (a) motions of F-actin within an actomyosin network. Images of 40 nM smooth muscle myosin (green) embedded within ~ 2 μM F-actin network (red). White dotted lines indicate alignment of F-actin. White arrows indicate direction of motion of F-actin. Scale bars are 5 μm. (b) Anisotropic velocity-velocity autocorrelation, δC_{vv}. Averages are taken across several experiments ($N_{\mathrm{SkMM}} = N_{0.25\%\mathrm{MC}} = N_{0.15\%\mathrm{MC}} = 3$, $N_{\mathrm{SmMM}} = 5$, $N_{\mathrm{NMM}} = 2$). Colors represent different experimental conditions. (c) Images of ~ 2 μM actin and 40 nM skeletal muscle myosin, showing evolution of the angle θ between the myosin and the underlying F-actin. Scale bar is 5 μm. (d) Ensemble average change in angle of myosin, $\bar{\delta\theta}$ (open diamonds), and mean myosin number density (filled dots) as functions of strain rate, ψ. Dotted lines are guides for the eye. Stable (S) and contractile (C) states indicated above plot. (e) Schematic of phase diagram showing how dissipation rate (blue), bending energy rate (black), and strain rate (green) all change as a function of the total activity, $\widetilde{\zeta}$. An increase in $\widetilde{\zeta}$ coincides with an increasing myosin density, indicated by the green myosin cartoons. Thermal, stable, and contractile states are indicated by T, S, and C, respectively. In the stable state, a schematic representation of myosin's perpendicular effects on F-actin are shown.

with increased activity. As the system is driven from equilibrium, the dissipation rate first increases in the stable state and then attenuates in the contractile state. In addition, the work applied, as indicated by the filament bending energy, increases and then decreases in the contractile state. This is likely due to mechanical relaxation via polarity sorting and filament severing. Thus, while the contractile state has the highest entropy, it is the stable state in which the *rate* of entropy production is maximized (Fig. 2.5e).

While we find that axial motions of F-actin, consistent with the canonical sliding of F-actin in muscle, are associated with contractility, stable fluctuations are dominated by transverse filament deformations (Fig. 2.5b). Furthermore, these transverse motions occur regardless of myosin isoform, suggesting the generality of these dynamic modes in the active stable state. These reversible F-actin plucking events arise from transient and diverse interactions between non-aligned myosin and F-actin and have been implicated as a source of stress amplification in disordered fiber networks [130]. A lack of alignment or overlap between myosin and actin filaments would imply that fewer myosin heads may be involved in the generation of active mechanical stress. Thus, this work challenges the prevailing model of molecular motors as dipoles oriented parallel to F-actin, that always yield to contractility. Likewise, the definition of motor-based activity is now more complex; there is a spectrum of interactions that occur in disordered assemblies of myosin and F-actin at the molecular level. That spectrum in turn, may determine network level entropy production and dissipation that stabilizes actively driven materials.

The relationship between motor activity and the accumulation and dissipation of mechanical energy, which determines material stability is complex. The complexity arises from a diversity of motor-filament interactions, and the impact of those interactions on the dissipation of mechanical energy. Our multi-length scale identification and characterization of active stability presents a comprehensive understanding for the dynamics of active biological materials.

Chapter 3

Energetics of non-equilibrium binding

3.1 Motivation

Biological assembly is predicated on the binding of various components. Within the cell cytoskeleton, this is primarily accomplished via crosslinkers, proteins that bind multiple cytoskeletal filaments [131, 132, 133, 134, 61], and molecular motors, which not only bind multiple filaments, but also exert active stresses upon the filaments they are bound to by the consumption of ATP [60]. While much work has been done on the non-equilibrium dynamics and forces generated by molecular motors [66, 135, 73, 67, 88, 4, 136], there has been considerably less work has focused on the energetic cost incurred by the (un)binding of crosslinkers themselves. This is due to an implicit assumption on the dynamics of cross-linker binding, namely that they obey detailed balance [137, 138, 129].

Binding kinetics that obey detailed balance ensures thermodynamically equilibrated dynamics of crosslinkers. This assumption has generally been considered correct because most crosslinkers cannot hydrolyze ATP or GTP, suggesting that they must obey equilibrium kinetics. While this is true for the binding rate of crosslinkers, the same is not true for the unbinding rate. Researchers have observed an increase in bond lifetime for crosslinkers under tension, a behavior dubbed a "catch bond" [139, 85, 86, 140]. This goes against the intuition that a bond would dissociate more quickly under tension, forming a so-called "slip-bond" [139]. Despite their counter-intuitive nature, catch bonds have been observed throughout biology, first in adhesion molecules of rolling leukocytes [141], then found in bacterial adhesion molecules [142], and also in actin binding proteins such as α-actinin [2] and myosin [83].

The presence of a force-dependent unbinding rate, and the lack of a reciprocal force-dependent binding rate, cause catch bonds to break detailed balance and introduce a source of irreversibility at the microscopic scale of hierarchically constructed biological materials. The extent to which a material constructed from catch bonds is driven away from equilibrium remains an open question. Further, the large-scale effects on the properties of such a material due to the presence of catch bonds is also unknown. In this chapter, I attempt to provide an answer to these questions by running molecular dynamics simulations of an actomyosin network, where myosin motors not only exert active stresses on an actin network, but also exhibit catch bond binding kinetics. We quantify the relative effects of motor walking and binding on the network's distance from equilibrium, the resulting material properties, and the time-reversal symmetries of the non-equilibrium quantities governing the system's distance from equilibrium.

My contribution to the below includes implementing the catch bond kinetics and irreversibility measurements in the simulations used throughout, running simulations, and interpretation of all results. The work presented here has been adapted from the following paper:

- A.P. Tabatabai†, **D.S. Seara**†, J. Tibbs, V. Yadav, I. Linsmeier, M.P. Murrell, Detailed Balance Broken by Catch Bond Kinetics Enables MechanicalAdaptation in Active Materials. *Advanced Functional Materials* 2020, 2006745.

3.2 Introduction

A nearly universal feature of natural and engineered materials is that the strength of molecular bonding weakens under externally applied mechanical load [118, 143, 144]. Referred to as slip bonds, load alters the bonds equilibrium free energy landscape and increases the rate of unbinding compared to the stress-free state [145, 146, 147]. The resulting destabilization of bonds leads to diverse material dynamics and properties, from the flow of defects and the emergence of yield stress in crystalline materials to viscoelasticity and creeping flows in amorphous materials [148, 149, 150, 151, 152, 153]. In rare cases, however, bonds may be reinforced, rather than weakened under load. Referred to as catch bonds, binding kinetics are altered to introduce feedback between applied mechanical load and the mechanical properties of the material itself [86]. In synthetic systems, mechanical load is applied externally and catch bonds can increase the mechanical toughness of the material in response, enabling several-fold increase in allowable strain [90, 154, 155, 89, 156]. While catch bonds in biological systems are also subject to external forces [86], active stresses in living matter are generated internally and the force generating units, in turn, sense and adapt to applied load [65]. If the source of the endogenous stress also acts as a catch bond, biological activity creates an adaptive feedback between macroscopic mechanical properties and microscopic, internal stress generation. Active stresses and catch bond kinetics may coordinate to drive a large spectrum in dynamic mechanical changes, better informing on the design of active materials.

The cell cytoskeleton is an active out-of-equilibrium system [157, 158] that can alter its rigidity or fluidity in order to maintain or change cell shape [159]. The cytoskeleton is comprised of protein polymers and enzymes that irreversibly convert chemical energy into mechanical work internally [160, 161, 162]. Specifically, the molecular motor myosin induces relative sliding of the actin polymers through binding, walking, and unbinding. The unbinding stage occurs at a rate that is itself dependent upon the magnitude of mechanical load the motor experiences [163, 164, 165, 166, 167, 168] and is therefore considered a catch bond [169, 170, 83]. As a result, unbinding kinetics break detailed balance and do not obey Boltzmann statistics [140, 171, 172, 173, 114, 174, 137]. However, the relative extent to which active stresses, catch bond kinetics, and their interactions contribute to the cytoskeleton's distance from equilibrium. Further, the general impact of broken detailed balance on the rigidity or fluidity of active materials is unknown.

In this work, we evaluate the impact of the combination of active stress and catch bond kinetics in the actomyosin crossbridge on the non-equilibrium thermodynamics and mechanics of a coarse-grained computational model of the cytoskeleton, as a model of an active material. To do so, we simulate disordered actomyosin networks and measure the actin flows induced by motors with varying load-dependence of the myosin unbinding rates. In parallel, we measure the breaking of detailed balance at the molecular scale and compare it to the propensity for the material to flow on the network scale. In doing so, we associate non-equilibrium quantities with different symmetries under time reversal with material phases in actomyosin.

3.3 Results

3.3.1 Catch strength controls force-dependent binding

To isolate the effects of catch bond behaviors in filament networks, we use the coarse-grained molecular dynamics simulation package AFINES [137]. As contractility has been shown to occur in the absence of actin crosslinking proteins [71, 5, 6], we study only the interactions between motors and filaments, respectively shown in black and red in Fig. 3.1a,b. Motors are modeled as two beads coupled by a spring and undergo Brownian motion when unbound. Motors can bind to actin filaments and walk along the filament once bound. The motor walks towards the barbed end of the actin filament with a force-dependent velocity, $v(F) = v_0(1 - F/F_{\text{stall}})$. When bound to two filaments, the motor walking transmits stress between the two filaments and throughout the rest of the actin network, provided the existence of sufficient network connectivity. See Appendix B.1 for full simulation details

Catch bond binding kinetics are generally modeled as an initial increase in bond lifetime, followed by a decrease at high forces [175, 83, 86]. The bond lifetime is given by the inverse of the unbinding rate, given by

$$k_{\text{off}}^{\text{eff}}(F) = k_{\text{off}}^{\text{c}} \exp(F\xi_{\text{c}}\beta) + k_{\text{off}}^{\text{s}} \exp(F\xi_{\text{s}}\beta), \tag{3.1}$$

where β is the inverse temperature, F is the force felt by the bond (in our simulations, the stretch of the spring that binds the two heads of a myosin filament), $\xi_{\text{c}} < 0$ and $xi_{\text{s}} > 0$ are parameters with units of length that give the strength of the force-dependence of the catch and slip pathways, leading to an exponential suppression and amplification of $k_{\text{off}}^{\text{eff}}$ respectively, and $k_{\text{off}}^{\text{c}}$ and $k_{\text{off}}^{\text{s}}$ are the basal unbinding rates for the catch and slip pathways, respectively. This catch-slip behavior replicates data seen from single molecule pulling experiments [83], where high force are applied to single molecules via beads trapped by optical tweezers [176]. However, there is a lack of evidence that catch bonds experience high enough forces to transition into the slip regime in their endogenous environment. We therefore use a low-force approximation to Equation 3.1 when defining a force dependent unbinding rate

$$k_{\text{off}}^{\text{eff}}(F) = k_{\text{off}}^{0} \exp(F\xi\beta). \tag{3.2}$$

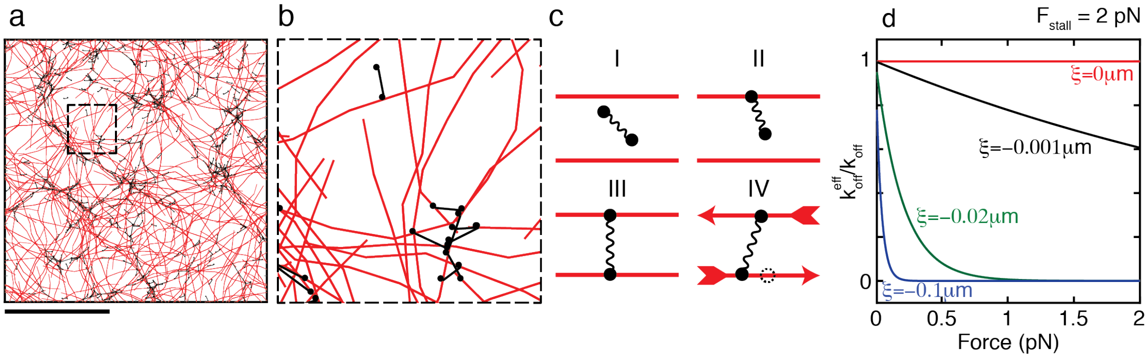

Figure 3.1: **Simulation and catch bond definitions** (a) A snapshot of a typical configuration for AFINES simulations, showing actin filaments (red) and myosin motors (black) randomly distributed in a box with periodic boundary conditions. Scale bar is 10 μm. (b) Zoomed in section of the same simulation as (a). (c) Illustration of the four states of a single simulated myosin motor: I. unbound, II. bound to a single actin filament, III. bound to two different actin filaments, IV. motor walking towards the "barbed" end of an actin filament. (d) Ratio of effective to basal off-rates as given in Equation 3.2, shown for various values of catch strength ξ (different colors), with stall force of $F_{\mathrm{stall}} = 2$ pN.

In what follows, we call ξ the catch strength. We vary $\xi \in [-0.5\mu\mathrm{m}, 0]$, corresponding to an energy range of $[-125\ k_{\mathrm{B}}T, 0]$ at a tensile force of $F = 1$ pN. We leave binding rate, k_{on}, independent of F, and thereby break detailed balance at the level of individual motor (un)binding events.

3.3.2 Catch bond kinetics alone switch (un)binding favorability

Before investigating the effects of catch bonds in a full network, we investigate the thermodynamic effects from binding kinetics alone. We simulate a simplified system with one motor within a circular array of immobile filaments. One motor head is fixed at the origin and the other head is free to diffuse (Fig. 3.2a). The thermally diffusing head stochastically binds and unbinds to filaments within the array with probabilities p_{B} and p_{U}, respectively, that are determined in part by the thermally fluctuating motor length L. Note that the rest length of the motor is less than the minimum distance to bind to a filament, therefore the motor will be stretched in the bound state. This system is further simplified by using a motor with zero walking speed, eliminating the traditional source of irreversibility from energy input via ATP dependent motor motility. We quantify the thermodynamic irreversibility, $\lambda(t)$, generated by the motor using a standard measure of the entropy production of a trajectory over a discrete state-space [177, 40, 31] (see Appendix B.4).

In our simulations, motors transition between only two states: bound and unbound. The total irreversibility is the cumulative sum over time of the contributions from binding and unbinding $\lambda(t) = \lambda_{\text{bind}}(t) + \lambda_{\text{unbind}}(t)$. In this simple system, without motor walking or network rearrangement, $\lambda(t)$ measures the deviation from the equilibrium binding affinity of the motor. The irreversibility from binding and unbinding varies with increasing catch strength (Fig. 3.2b,c). Both the number of (un)binding events and the relative probabilities of (un)binding contribute to changes in irreversibility. Using a microscopic detailed balance assumption we interpret negative values of $\lambda_{\text{bind}}(t)$ and $\lambda_{\text{unbind}}(t)$ as transitions that require heat to be absorbed from a temperature bath [178]. Within this configuration, the average total irreversibility, $\langle\lambda\rangle$, increases with catch strength (Fig. 3.2d). Interestingly, $\lambda_{\text{bind}}(t)$ and $\lambda_{\text{unbind}}(t)$ both change sign as $|\xi|$ increases. Specifically, unbinding begins as an energetically favorable transition, indicated by a net positive λ_{unbind}, and vice-versa for binding. As $|\xi|$ increases, unbinding becomes energetically costly due to the decreased probability of unbinding.

To investigate this differential effect of ξ on large scale mechanical properties in the presence of motor walking, we simulate fully mobile actomyosin networks while varying ξ to measure network flow and energy storage.

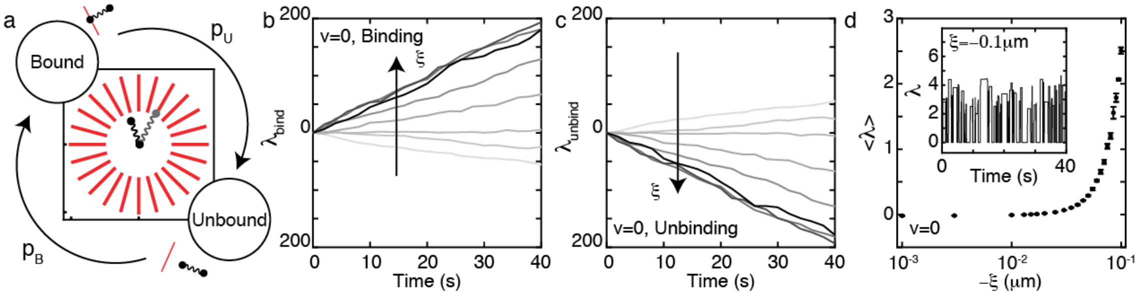

Figure 3.2: **Irreversibility switches due to broken detailed balance by catch bonds** (a) Illustration of the circular array of actin filaments (red) and diffusing myosin motor with one head anchored at the origin in bound (black) and unbound (gray) states. Circles and arrows show a schematic of a motor switching from a bound state to an unbound state with probability p_{U}, and similar for a motor switching from the unbound to the bound state. Box is 2.1 μm wide. (b) Irreversibility due to binding, λ_{bind} as a function of time for increasing $|\xi|$. (c) Irreversibility due to unbinding, $\lambda_{\mathrm{unbind}}$ as a function of time for increasing $|\xi|$. (d) Mean total irreversibility, $\langle\lambda\rangle$, as a function ξ. Inset shows a prototypical example of the total irreversibility over time, $\lambda = \lambda_{\mathrm{bind}} + \lambda_{\mathrm{unbind}}$, for $\xi = -0.1$ μm.

3.3.3 Detailed balance broken by catch bonds underlies a fluid-solid transition

To understand how the breaking of detailed balance by catch bonds affects network mechanics, we observe the evolution of fully mobile disordered networks with motor velocity 1 μm/s. Ideal motors ($\xi = 0$ μm) at a number density of $\rho = 0.8$ $\mu\mathrm{m}^{-2}$ contract and condense actomyosin network into regions of high density asters, as previously observed (Fig. 3.3a) [179, 180, 138]. Changes in the catch strength lead to dramatic changes in network evolution: intermediate catch strength ($\xi = -0.01$ μm) network also condense into asters (Fig. 3.3b), however high catch strength ($\xi = -0.1$ μm) results in arrested flow and limited reorganization of actin (Fig. 3.3c).

We quantify the mechanical effects of catch bonds by calculating the energy density of each network, $\omega(t) = \sum_i U_i/L^2$, where U_i is the potential energy of the i^{th} component of both the actin filaments and myosin motors and L^2 is the area of the simulation box (Section B.3). We observe that networks at low to intermediate values of ξ exhibit an increase and subsequent decrease in $\omega(t)$. However, networks with large catch strengths do not have the decrease in ω at late times (Fig. 3.3d). In addition, we quantify actin flow during contraction by calculating the cumuluative displacement field $\mathbf{x}$ of the actin filaments interpolated onto a grid (Fig. 3.3e, see Appendix B.2 for details). We use $\mathbf{x}$ to define a network strain, $\varepsilon(t) = \langle \boldsymbol{\nabla} \cdot \mathbf{x}(t) \rangle$, and quantify the extend of the network's evolution by the maximum strain, $\varepsilon_{\max}$ and the rate of contractility by the strain rate, $\dot{\varepsilon}$, measured in the times when $\varepsilon \in [(1/4)\varepsilon_{\max}, (3/4)\varepsilon_{\max}]$ [4].

We find that an increase in $|\xi|$ generates a non-monotonic response in the maximum energy density $\omega_{\max}$, the maximum strain $\varepsilon_{\max}$, and strain rate $\dot{\varepsilon}$ (Fig. 3.3g-i). All non-monotonic behaviors occur over the same range of catch strength, $\xi \in [-10^{-3}, -10^{0}]$. This non-monotonic is not observed for ideal motors (insets of Fig. 3.3g-i), indicating that a force-dependent unbinding rate, not active stress, is essential to get the non-monotonic behavior.

We define a liquid-like regime for $|\xi| < 0.01$ μm, where increases in $|\xi|$ increase contraction rate and the total accumulated strain. By contrast, we define a soid-like regime for $|\xi| > 0.01$ μm, where increases in $|\xi|$ do not increase actin flow. By this definition, the catch strength of the actomoysin crossbridge mediates an fluid-solid dynamical phase transition that is not observed with force independent binding kinetics of the active molecular motors.

3.3.4 Network connectivity is insufficient to drive solid-like behavior

Previous works have suggested that network percolation drives a rigidity transition in cytoskeletal networks [181, 182, 88]. Here, we test the influence of connectivity and binding kinetics to understand the origin of the observed fluid-solid transition.

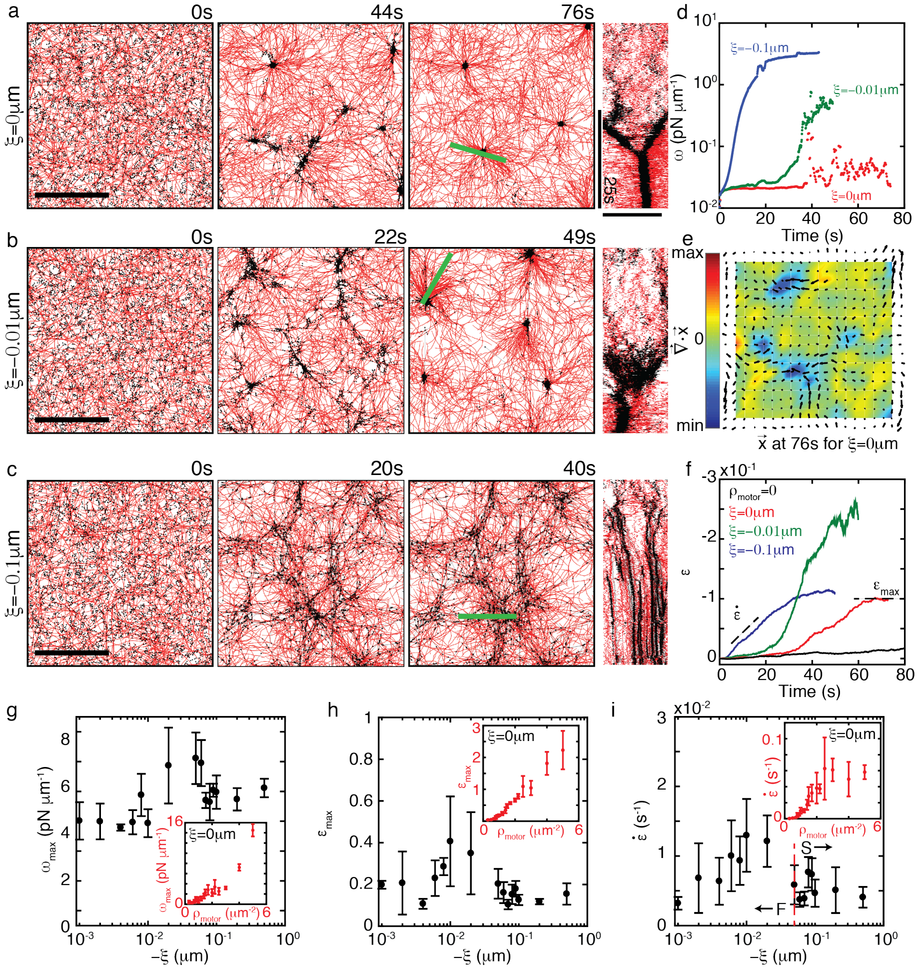

Figure 3.3: **Catch bonds mediate a fluid-solid transition** (a) Snapshots of a typical simulation containing actin (red) and myosin (black) with $\xi = 0$ μm. The rightmost plot shows a kymograph of the dynamics around an eventual aster along the green line. (b) Similar to (a), but with motors of intermediate catch strength, $\xi = -0.01$ μm. (c) Similar to (a), but with motors of high catch strength, $\xi = -00.1$ μm. (d) Typical temporal evolution of energy density, ω, for simulations with various catch strengths ($\xi = 0$ μm, red; $\xi = -0.01$ μm, green; $\xi = -0.1$ μm, blue). (e) Strain field $\mathbf{x}$ (black arrows) and resulting strain, $\boldsymbol{\nabla} \cdot \mathbf{x}$ (colormap) shown for the final snapshot in (a). Arrow sizes are scaled relative to the maximum vector at $t = 76$ s. (f) Typical temporal evolution of the strain, ε for various catch strengths ($\xi = 0$ μm, red; $\xi = -0.01$ μm, green; $\xi = -0.1$ μm, blue). Black line shows the strain measured for actin filaments subject to only thermal fluctuations. (g-i) Maximum energy density $\omega_{\max}$ (g), maximum strain $\varepsilon_{\max}$ (h), and strain rate $\dot{\varepsilon}$ (i) averaged over $N \geq 4$ simulations as a function of catch strength ξ. Insets in (g-i) contain the same information but for ideal motors ($\xi = 0$ μm) as a function of ρ.

First, we observe that catch bonds give rise to an increase in bound motor population within a network (Fig. 3.4a), suggesting that the overall connectivity may be causing the observed mechanical response. Since an increase in bound motors is also observed by increasing the concentration of ideal bonds, we calculate the network connectivity for networks composed of ideal and catch bonds separately in order to isolate the effects of binding kinetics on the mechanical transition. Network connectivity is calculated by counting the average number of neighboring filaments that each filament is connected to through a motor by $\langle z \rangle = 2N_\mathrm{m}/N_\mathrm{f}$, where N_m is the number of motors connecting each actin filament to other filaments and N_f is the total number of actin filaments within the system (Fig. 3.4b). These values are independent of the measured time and redundant connections are not counting.

Both increasing catch strength and increasing ideal motor concentration lead to a smoothly increasing connectivity over the range $3 < \langle z \rangle < 4$. However, ideal motors never exhibit the decrease in contractility, as quantified by ε_max, seen in networks containing catch bond kinetics (Fig. 3.4c). From this we conclude that connectivity alone cannot explain the transition to a solid-like regime. Furthermore, this provides yet another regime where the Maxwell criterion for mechanical stability [183] does not hold. Maxwell's counting argument says that 2D structures need a connectivity of $z_\mathrm{c} = 4$ to resist a shear. Previous work has shown that filament bending rigidity can lower the threshold needed for the onset of mechanical rigidity [68]. Here, we show that non-equilibrium kinetics of bonds can also lower the threshold for the onset of stability.

We observe a sharp decrease in motor walking speed concomitant with the increase in connectivity for catch bonds, indicating that motors are under load and force-dependent binding kinetics are engaged in the solid regime. To further investigate the difference in load in the fluid and solid regimes, we calculate the bond lifetimes as a function of ξ. Consistent with the increase in bound motors and the

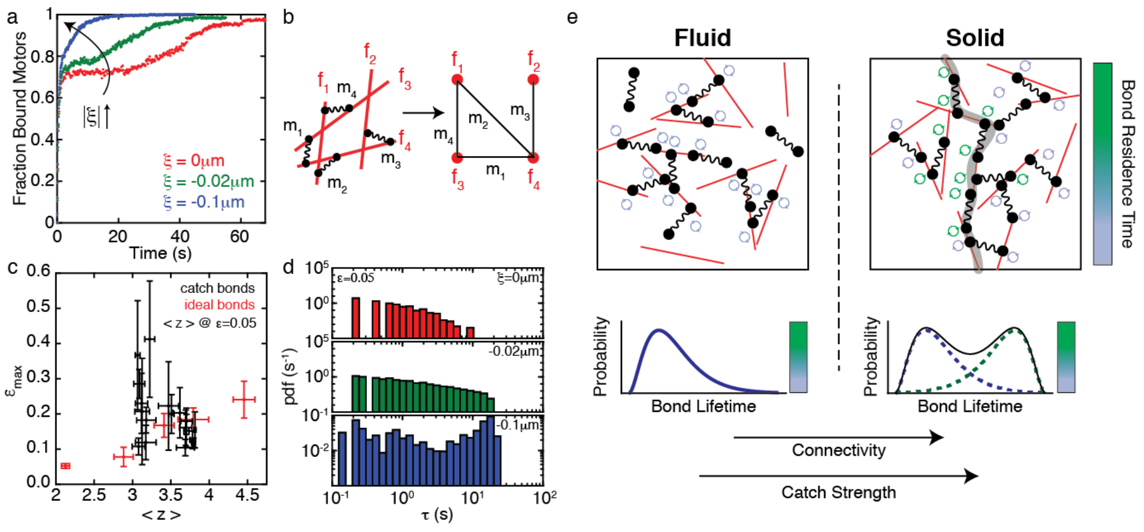

Figure 3.4: **Active stress is necessary but insufficient to induce the fluid-solid transition** (a) Typical time series for the fraction of bound motors shown for various catch strengths ($\xi = 0$ μm, red; $\xi = -0.02$ μm, green; $\xi = -0.1$ μm, blue). (b) Schematic showing an example of how network connectivity is calculated. We map filaments (red) and motors (black) to nodes and edges, respectively, of a graph. We then calculate the average connectivity of the nodes in the resultant network. (c) Maximum strain, $\varepsilon_{\mathrm{max}}$, against average network connectivity, $\langle z \rangle$, for ideal motors (red) and catch bonds with various values of ξ (black). Connectivity is calculate at a strain of $\varepsilon = 0.05$. (d) Probability distribution function of bond lifetimes, τ, that have contracted to a strain of $\varepsilon = 0.05$. (e) Schematic of network properties that differentiate the fluid and solid phases. Circular arrows indicate the lifetime of bound motors, the distribution of which is given by the distributions on the bottom of the cartoon. In the solid phase, there exists at least one system spanning path, illustrated by the gray path. All data with error bars are plotted as mean ± standard deviation.

change in motor speed, we observe that the distribution of bond lifetimes broadens due to the emergence of a long-lifetime population of bound motors in the solid state (Fig. 3.4d,e). A decrease in motor speed generates less stress per unit time and may underlie the decrease in energy density seen at high $|\xi|$ (Fig. 3.3g).

3.3.5 Time-reversal symmetries correlate to material phases

As catch bonds break detailed balance, as shown previously for a simplified configuration, we next calculate the irreversibility for binding kinetics for full networks in order to understand the role of non-equilibrium thermodynamics in the observed fluid-solid transition. Contributions to irreversibility from binding and unbinding, λ_{bind} and λ_{unbind}, accumulate over time, even in the absence of walking (Fig. 3.5a, b). We define a characteristic irreversibility, λ^*, while the system is in a steady state at early times ($t < 20$ s) to characterize the flow of energy. λ^* increases with increasing catch strength, showing two separate regimes that coincide with the fluid and solid behaviors (Fig. 3.5c). When increasing catch strength leads to an increase in network fluidity ($|\xi| < 0.01$ μm), there are small changes in λ^*, but when increasing catch strength leads to network solidification ($|\xi| > 0.01$ μm), λ^* increases rapidly.

The irreversibility is a cumulative measure and can increase either due a changing number of total (un)binding events, or due to changes in the irreversibility of each individual contribution. To differentiate these effects, we report the total number of binding events, N^*, measured at the same time chosen to measure λ^*, calculate the mean irreversibility given by λ^*/N^*. This mean irreversibility is independent of the number of transitions and thus measures purely the time-reversal asymmetric contribution of the irreversibility, while N^* measures time-reversal symmetric non-equilibrium contributions to the irreversibility. We find that λ^*/N^* is invariant in the fluid phase, and increases significantly in the solid phase. By contrast, N^* exhibits a slow decrease in the liquid regime, and a steeper decrease in the solid regime. This reflects that changes in time-reversal symmetric quantities contribute to the network's fluidity, but a change in time-reversal asymmetric quantities underlie the transition to a solid phase.

3.4 Conclusion

Naturally occurring in biological systems [184, 185, 186], catch bonds are fundamental building blocks for the assembly of non-equilibrium materials. The irreversible

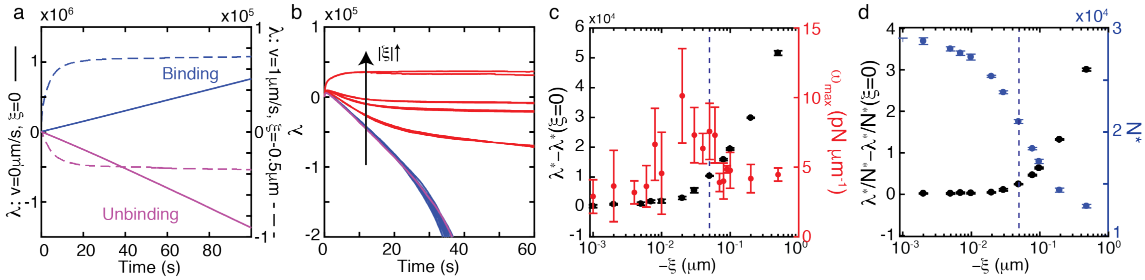

Figure 3.5: **Symmetries of contributions to irreversibility correlate with fluid and solid phases** (a) Representative time series for irreversibility due to binding (blue) and unbinding (magenta). Solid lines show the result for ideal motors ($\xi = 0$ μm with zero walking velocity ($v = 0$ μm/s). Dotted lines show the result for catch bond motors ($\xi = -0.5$ μm) with a non-zero walking velocity ($v = 1$ μm/s). (b) Total irreversibility over time for motors with $v = 1$ μm/s as a function of ξ. Blue and red lines correspond to catch strength values in the fluid and solid regimes of Fig. 3.3, respectively. Magenta line shows λ for $\xi = 0$ μm. (c) Irreversibility at $t = 5$ s, λ^*, and maximum energy density, ω_{max} (same data as Fig. 3.3g). (d) Mean irreversibility, λ^*/N^* and total number of binding events, N^*, at $t = 5$ s. Vertical dashed lines in (c) and (d) delineates fluid (left of dashed line) and solid (right of dashed line) behavior of the network..

conversion of chemical energy into mechanical work has two components, in the generation of active stresses through motor walking, and the load-dependent unbinding of the motor. Using actomyosin as a model of active materials in general, we delineate their relative impact on the breaking of detailed balance at the microscopic scale, and further investigate how ti translates to large-scale mechanical phenomena.

The interplay between motor walking and catch-bond kinetics drives the system away from equilibrium and determines the material properties of the actomyosin network. Near equilibrium, the material is an active fluid, where small changes in λ lead to large changes in the actin flow rate. Further, changes in the thermodynamic irreversibility in this regime are dominated by changes in N^* (Fig. 3.5c, d), the total number of transitions made by the system. This is a time-symmetric non-equilibrium property that can be related to quantities such as an effective temperature [73] or "frenesy" and "traffic" as introduced in other works [187, 188]. Thus, fluidity is driven by motor walking that is allowed to propagate for longer distances and times as the number of unbinding events decreases, but the irreversibility of the unbinding itself remains unchanged. By contrast, changes in λ are dominated by the mean irreversibility, λ^*/N^*, at high values of ξ, making the network an active solid. While increases in ξ lead to large changes in λ^*/N^* (Fig. 3.5), material flow is suppressed to a lower state than at lower values of ξ, and become arrested in time (Fig. 3.3). Time-reversal asymmetric quantities govern the transition to a solid regime, highlighting that catch bond kinetics, not motor activity, dominate the system's thermodynamics far from equilibrium, in contrast to previous works [189]. We also observe the emergence of a bimodal distribution of bond lifetimes in the solid state, reflecting heterogeneity in the network connectivity and network stress. Thus, large scale mechanical properties and phases adapt to the breaking of detailed balance at microscopic scales.

These results highlight the role of catchbonds on fluidity, as well as rigidity, as the latter is principally observed in synthetic systems [90, 154, 155, 89, 156]. Furthermore, the nonmonotonic change in material fluidity is also observed in biochemical reconstitution experiments that closely resemble our simulations. In the experiments, we alter an effective catch strength through the increase in motor content or Factin crosslinking by α-actinin (Figures B.1 & B.2) [167, 186, 190, 191].

In summary, active stress drives the system away from thermodynamic equilibrium, but requires non-equilibrium binding kinetics to mount an adaptive mechanical response. These results highlight fundamental design principles and energetic costs for the assembly and actuation of active materials, where multiple sources of non-equilibrium driving can compete to produce diverse material properties.

Chapter 4

Energetics of biochemical oscillations

4.1 Motivation

The previous chapters investigated how interactions at the single protein level endows actomyosin networks with their mechanical and dynamical properties. In Chapter 2, we discovered how myosin motions can dissipate myosin induced stresses in order to maintain mechanically stable steady state dynamics. In Chapter 3, we discovered how the binding kinetics of individual myosin motors can control a transition between states with a propensity for flow and states with arrested mobility. These works provide a bottom-up approach to active materials design, where tuning dissipation at the microscale leads to emergent macroscopic phenomena. In this chapter, we invert this perspective to take a top-down approach towards addressing another fundamental tool used by living matter – reaction-diffusion dynamics.

At single cell length scales and above, continuum approaches have been successful in describing protein dynamics [192, 193, 63, 194, 64, 65]. In these cases, proteins are described by fields that undergo inter- and intra-species chemical reactions and are subject to diffusion by thermal forces. Drawing on techniques found throughout condensed matter physics, models for these dynamics are often phenomenological, containing all terms allowed by the symmetries present in the problem that replicate the dynamics seen in experiments [195, 93].

In particular, oscillatory dynamics are ubiquitous in biology [196], from ion-mediated electrical signal transmission down neurons [197] to phosphorylation-driven circadian rhythms [198, 199] to reaction-diffusion based oscillations critical for cell division in both bacteria [200] and eukaryotes [110, 201]. Models that replicate these dynamics break time-reversal symmetry and are thus manifestly non-equilibrium models. However, quantifying the energy dissipated across space, and how the total energy dissipation can tune the observed dynamics, remains unclear. In order to address these challenges, I developed a method for estimating irreversibility directly from spatiotemporal data, without requiring knowledge of the underlying dynamics. This method is widely applicable to dynamics in any number of spatial dimensions, and is used to study the thermodynamics of a dynamical phase transition in a popular model for biochemical oscillators.

My contribution in the following is the development of the theory, writing and analyzing all simulations, and interpretation of the results. The work presented here has been adapted from the following paper:

- **D.S. Seara**, B.B. Machta, M.P. Murrell, Irreversibility in dynamical phases and transitions *Nature Communications* 12, 392 (2021).

4.2 Introduction

In many-body systems, collective behavior that breaks time-reversal symmetry can emerge due to the consumption of energy by the individual constituents [192, 194, 63]. In biological, engineered, and other naturally out of equilibrium processes, entropy must be produced so as to bias the system in a forward direction [39, 202, 12, 203, 204, 205]. This microscopic breaking of time reversal symmetry can manifest at different length and time scales in different ways. For example, bulk order parameters in complex reactions can switch from exhibiting incoherent, disordered behavior to stable static patterns [94, 206] or traveling waves of excitation [207, 93] that break time reversal symmetry in both time and space simply by altering the strength of the microscopic driving force. Recent advances in stochastic thermodynamics have highlighted entropy production as a quantity to measure a system's distance from equilibrium [208, 76, 136, 209, 210, 211]. While much work has been done investigating the critical behavior of entropy production at continuous and discontinuous phase transitions [212, 213, 214, 215, 216, 217, 218, 219, 220], dynamical phase transitions in spatially extended systems have only recently been investigated, and to date no non-analytic behavior in the entropy production has been observed [97, 221].

To address this, we introduce what we term the entropy production factor (EPF), a dimensionless function of frequency and wavevector that measures time reversal symmetry breaking in a system's spatial and temporal dynamics. The EPF is a strictly non-negative quantity that is identically zero at equilibrium, quantifying how far individual modes are from equilibrium. Integrating the EPF produces a lower bound on the entropy production rate (EPR) of a system. We illustrate how to calculate the EPF directly from data using the analytically tractable example of Gaussian fields obeying partly relaxational dynamics supplemented with out of equilibrium coupling [195]. We then turn to the Brusselator reaction-diffusion model for spatiotemporal biochemical oscillations to study the connections between pattern formation and irreversibility. As the Brusselator undergoes a Hopf bifurcation far from equilibrium, its behavior transitions from incoherent and localized to coordinated and system-spanning oscillations in a discontinuous transition. The EPF quantifies the shift in irreversibility from high to low wave-number as this transition occurs, but the EPR is indistinguishable from that of the well-mixed Brusselator where synchronization cannot occur. Importantly, the EPF can be calculated in any number of spatial dimensions, making it broadly applicable to a wide variety of data types, from particle tracking to 3+1 dimensional microscopy time series.

4.3 Results

4.3.1 Entropy production factor derivation

Consider a system described by a set of M real, random variables obeying some possibly unknown dynamics. A specific trajectory of the system over a total time T is given by $\mathbf{X} = \{X^i(t) | t \in [0, T]\}$. Given an ensemble of trajectories, the average EPR, $\dot{S}$, is bounded by [41, 202, 12]

$$\begin{aligned}\dot{S} &\geq \lim_{T\to\infty} \frac{1}{T} D_{\mathrm{KL}}\left(P[\mathbf{X}] \,\middle\|\, P[\widetilde{\mathbf{X}}]\right) \\ D_{\mathrm{KL}}\left(P[\mathbf{X}] \,\middle\|\, P[\widetilde{\mathbf{X}}]\right) &= \left\langle \log\left(\frac{P[\mathbf{X}]}{P[\widetilde{\mathbf{X}}]}\right)\right\rangle_{P[\mathbf{X}]}\end{aligned} \tag{4.1}$$

where we have set $k_{\mathrm{B}} = 1$ throughout and D_{KL} denotes the Kullback-Leibler divergence which measures the distinguishability between two probability distributions. $P\left[\mathbf{X}\right]$ and $P[\widetilde{\mathbf{X}}]$ are the steady state probability distribution functionals of observing the path $\mathbf{X}(t)$ of length T and the probability of observing its reverse path, respectively. Therefore, the KL divergence in Equation 4.1 measures the statistical irreversibility of a signal, and saturates the bound when $\mathbf{X}$ contains all relevant, non-equilibrium degrees of freedom.

We further bound the irreversibility itself by assuming the paths obey a Gaussian distribution. Writing the Fourier transform of $X^i(t)$ as $x^i(\omega)$, where ω is the temporal frequency, and writing the column vector $\mathbf{x}(\omega) = (x^1(\omega), x^2(\omega), \ldots)^T$:

$$P[\mathbf{x}(\omega)] = \frac{1}{Z} \prod_{\omega_n} \exp\left(-\frac{1}{2T} \mathbf{x}^\dagger C^{-1} \mathbf{x} \right), \tag{4.2}$$

where $\mathbf{x}^\dagger$ denotes the conjugate transpose of the vector $\mathbf{x}$ evaluated at the discrete frequencies $\omega_n = 2\pi n T^{-1}$. $C(\omega_n)$ is the covariance matrix in Fourier space with elements $C^{ij}(\omega_n) = \langle x^i(\omega_n) x^j(-\omega_n) \rangle T^{-1}$, and Z is the partition function. The expression for $P[\widetilde{\mathbf{x}}]$ is identical but with $C^{-1}(\omega_n) \to C^{-1}(-\omega_n)$. Combining Equation 4.1 with Equation 4.2 and taking $T \to \infty$, we arrive at our main result:

$$\dot{S} = \int \frac{d\omega}{2\pi} \, \mathcal{E}(\omega); \qquad \mathcal{E}(\omega) = \frac{1}{2} \left[C^{-1}(-\omega) - C^{-1}(\omega) \right]_{ij} C^{ji}(\omega). \tag{4.3}$$

This defines the EPF, $\mathcal{E}(\omega)$, which measures time reversal symmetry breaking interactions between $M \geq 2$ variables, while integrating $\mathcal{E}$ gives $\dot{S}$. $\mathcal{E}(\omega) = D_{\mathrm{KL}}(P[\mathbf{x}(\omega)] \,||\, P[\widetilde{\mathbf{x}}(\omega)])$ measures the Kullback-Leibler divergence between the joint distribution of M modes at a single frequency ω. While this quantity does not scale with trajectory length, the density of modes near a particular frequency is related to the total trajectory time by $\Delta\omega = 2\pi T^{-1}$. Since $\pm\omega$ modes must be complex conjugates of each other and an overall average phase is prohibited by time translation invariance, asymmetry between these distributions can only be captured by relative phase relationships, quantified by their correlation functions. $\mathcal{E}$ is large when one variable tends to lead another in phase, implying a directed rotation between these variables in the time domain.

As mentioned above, $P[\mathbf{x}(\omega)]$ describes the dynamics of a non-equilibrium steady state, and no reversal of external protocol is assumed. Further, in writing an expression for $P[\widetilde{\mathbf{x}}(\omega)]$, we assume that the observables are scalar, time-reversal symmetric quantities, such as the chemical concentrations we analyze below.

The Gaussian assumption we make here makes Equation 4.3 exact only for systems obeying linear dynamics. Nevertheless, $\mathcal{E}$ is still defined for non-linear systems, where the integrated $\mathcal{E}$ lower bounds the true $\dot{S}$. To see this, consider projecting complex dynamics onto Gaussian dynamics by choosing a data processing procedure which preserves two point correlations but which removes higher ones. This can be accomplished by multiplying every frequency by an independent random phase — a post processing procedure which can be applied to individual trajectories. Post-convolution, the integrated EPF is equal to the KL divergence rate between forward and backwards rates. From the data processing inequality, the KL divergence rate of the true fields must be higher, so that the integrated EPF lower bounds the true entropy production rate (Appendix C.2). In addition to bounding the true $\dot{S}$, we expect the integral of $\mathcal{E}$ to be a good approximation for the wide class of systems where linearization is reasonable. Such Gaussian approximations are starting points in many field theories, with higher order interactions accounted for by adding anharmonic terms in the action of Equation 4.2. While this is not our focus here, we expect these additional terms to systematically capture corrections to $\dot{S}$ that do not appear in Equation 4.3. As $C^{ii}(\omega) = C^{ii}(-\omega)$, the only contributions to $\mathcal{E}$ come from the cross-covariances between the random variables of interest. As such, this bound yields exactly 0 for a single variable even though higher order terms may contribute to $\dot{S}$.

This formulation extends naturally to random fields. For M random fields in d spatial dimensions, $\boldsymbol{\phi} = \{\phi^i(\mathbf{x}, t) | t \in [0, T], \mathbf{x} \in \mathbb{R}^d\}$, the EPR density, $\dot{s} \equiv \dot{S}/V$

where V is the system volume, is:

$$\begin{aligned} \dot{s} &= \int \frac{d\omega}{2\pi} \frac{d^d\mathbf{q}}{(2\pi)^d}\ \mathcal{E}(\mathbf{q},\omega); \\ \mathcal{E}(\mathbf{q},\omega) &= \frac{1}{2}\left[C^{-1}(\mathbf{q},-\omega) - C^{-1}(\mathbf{q},\omega)\right]_{ij} C^{ji}(\mathbf{q},\omega). \end{aligned} \tag{4.4}$$

where $C^{ij}(\mathbf{q},\omega)$ is the dynamic structure factor and $\mathcal{E}(\mathbf{q},\omega)$ is now a function of wavevector q and frequency ω.

Even without an explicit, analytic expression for the structure factor, C, we can estimate $\mathcal{E}$ from data. To use Equation 4.4, we consider data of N finite length trajectories of M variables over a time T in d spatial dimensions. Each dimension has a length L_i. We create an estimate of the covariance matrix, $\widetilde{C}(\mathbf{q},\omega)$, from time-series using standard methods [see Methods]. These measurements will inevitably contain noise that is not necessarily time-reversal symmetric, even for an equilibrium system. Noise due to thermal fluctuations and finite trajectory lengths in the estimate of $\widetilde{C}$ from a single experiment ($N = 1$) will systematically bias our estimated $\mathcal{E}$ by $\Delta\mathcal{E} = \frac{M(M-1)}{2}$ at each frequency and will thereby introduce bias and variance in our measurement of $\dot{s}$. We can simply remove the bias from our measured $\mathcal{E}$, but to reduce the variance, we smooth $\widetilde{C}$ by component-wise convolution with a multivariate Gaussian of width $\boldsymbol{\sigma} = (\sigma_{q_1}, \ldots, \sigma_{q_d}, \sigma_\omega)$ in frequency space, giving $\hat{C}$. This is equivalent to multiplying each component of the time domain $\widetilde{C}(\mathbf{r},t)$ by a Gaussian, cutting off the noisy tails in the real space covariance functions at large lag times. We then use $\hat{C}$ in Equation 4.4 to create our final estimator for the EPF, $\hat{\mathcal{E}}$, and thereby the EPR, $\hat{\dot{s}}$. We calculate and remove the bias in $\hat{\mathcal{E}}$ and $\hat{\dot{s}}$ in all results below [see Methods]. Smoothing $\widetilde{C}$ with increasingly wide Gaussians in ω and $\mathbf{q}$ leads to a systematic decrease in $\hat{\dot{s}}$ due to reduced amplitudes in $\widetilde{C}$ (Appendix C.4).

To illustrate the information contained in $\mathcal{E}$, its numerical estimation, and the accuracy of $\hat{\dot{s}}$, we analyze simulations of coupled, 1 dimensional Gaussian stochastic fields for which $\mathcal{E}$ and $\dot{s}$ can be calculated analytically. We then study simulations of the reaction-diffusion Brusselator, a prototypical model for non-linear biochemical oscillators, and use $\mathcal{E}$ to study how irreversibility manifests at different time and length scales as the system undergoes a Hopf bifurcation [95].

4.3.2 Driven Gaussian fields

Consider two fields obeying Model A dynamics [195] with non-equilibrium driving parametrized by α:

$$\begin{aligned}\partial_t\phi(x,t) &= -D\frac{\delta\mathcal{F}}{\delta\phi} - \alpha\psi + \sqrt{2D}\xi_\psi \\ \partial_t\psi(x,t) &= -D\frac{\delta\mathcal{F}}{\delta\psi} + \alpha\phi + \sqrt{2D}\xi_\phi,\end{aligned} \tag{4.5}$$

where $\xi(\mathbf{x},t)$ is Gaussian white noise with variance $\langle \xi^i(\mathbf{x},t)\xi^j(\mathbf{x}',t')\rangle = \delta^{ij}\delta(\mathbf{x}-\mathbf{x}')\delta(t-t')$, D is a relaxation constant, and $\delta\mathcal{F}/\delta\phi$ is the functional derivative with respect to ϕ of the free energy $\mathcal{F}$ given by:

$$\mathcal{F} = \int dx \left[\frac{r}{2}(\phi^2+\psi^2) + \frac{1}{2}\left(|\partial_x\phi|^2 + |\partial_x\psi|^2\right)\right], \tag{4.6}$$

so that the fields have units of $\ell^{1/2}$ and r penalizes large amplitudes.

The EPR density, $\dot{s}$, is calculated analytically in two ways. First, we solve Equation 4.1 directly using the Onsager-Machlup functional for the path probability functional of $\boldsymbol{\eta}(x,t) = (\phi(x,t),\psi(x,t))^T$ [39, 222]. Second, the covariance matrices are calculated analytically, used to find $\mathcal{E}$ through Equation 4.4, and integrated to find $\dot{s}$. Both cases give the same result for $\dot{s}$. The result for both $\mathcal{E}$ and $\dot{s}$ are [Appendix C.1]:

$$\mathcal{E}^{\mathrm{DGF}} = \frac{8\alpha^2\omega^2}{(\omega^2-\omega_0^2(q))^2 + (2D(r+q^2)\omega)^2}, \quad \dot{s}^{\mathrm{DGF}} = \frac{\alpha^2}{D\sqrt{r}}. \tag{4.7}$$

We see that $\mathcal{E}^{\mathrm{DGF}} \geq 0$ and exhibits a peak at $(q, \omega) = (0,\ \omega_0(0))$, where $\omega_0(q) = \sqrt{(D(r+q^2))^2 + \alpha^2}$, indicating that the system is driven at all length scales with a driving frequency of α, dampened by an effective spring constant Dr. In addition, it is clear that multiple combinations of α, r, and D can give the same value for $\dot{s}$ while $\mathcal{E}$ distinguishes between equally dissipative trajectories in the shape and location of its peaks. In this way, $\mathcal{E}$ gives information about the form of the underlying dynamics not present in the total EPR.

We note that $\mathcal{E}^{\mathrm{DGF}}$ is also recovered using an appropriately modified version of the generalized Harada-Sasa Relation (GHSR) introduced in [222]. The non-equilibrium driving in Equation 4.5 comes from a rotational current between the two fields, rather than from a current derived from the gradient of a non-conservative chemical potential. This requires us to derive a slightly altered version of the GHSR than given in [222], largely following the steps outlined therein. In addition, our 2-field problem requires that the response and correlation functions be tensors, and the energy dissipation is related to the trace of their difference [223]. The resulting GHSR is

$$\dot{S} = \int \frac{d\omega}{2\pi} \frac{d\mathbf{q}}{(2\pi)^d} \sigma(\mathbf{q}, \omega); \qquad \sigma(\mathbf{q}, \omega) = \frac{\omega}{D} \operatorname{Tr}\left[\omega C(\mathbf{q}, \omega) - 2\widetilde{\mathcal{R}}(\mathbf{q}, \omega)\right], \tag{4.8}$$

where $C(\mathbf{q}, \omega)$ is the covariance matrix given in Appendix C.1 and $\widetilde{\mathcal{R}}$ is the imaginary component of the response tensor due to the presence of a constant external field (h_ϕ, h_ψ), adding the term $h_\phi \phi + h_\psi \psi$ to the free energy in Equation 4.6.

We now show that $\sigma = \mathcal{E}$ for the driven Gaussian fields. As we have already calculated the correlation matrix, we are left to calculate $\mathcal{R}_{ij} = (\delta\langle\eta_i\rangle / \delta h_j)\,|_{h_j \to 0}$, where $\boldsymbol{\eta} = (\phi, \psi)$. Solving the perturbed versions of 4.5 in frequency space and taking the mean, we find

$$\langle\phi\rangle = \frac{Dh_\phi + \alpha\langle\psi\rangle}{D(r+q^2) - i\omega} \tag{4.9}$$

$$\langle\psi\rangle = \frac{Dh_\psi - \alpha\langle\phi\rangle}{D(r+q^2) - i\omega}. \tag{4.10}$$

Plugging one solution into the other, we find the auto-responses to be equal to each other, giving

$$\mathrm{Tr}\left[\mathcal{R}\right] = \frac{2D\left(D(r+q^2) - i\omega\right)}{\left(D(r+q^2) - i\omega\right)^2 + \alpha^2} \to \mathrm{Tr}\left[\widetilde{\mathcal{R}}\right] = \frac{2D\omega\left(D^2(r+q^2)^2 - \alpha^2 + \omega^2\right)}{(\omega^2 - \omega_0^2)^2 + (2r\omega)^2}, \tag{4.11}$$

where ω_0 is defined as in the main text, $\omega_0^2 = D^2(r+q^2)^2 + \alpha^2$. As can be seen in the previous section, the trace of the correlation function is

$$\mathrm{Tr}\left[C\right] = \frac{4D\left(D^2(r+q^2)^2 + \alpha^2 + \omega^2\right)}{(\omega^2 - \omega_0^2)^2 + (2r\omega)^2}. \tag{4.12}$$

This finally gets us to our desired result

$$\sigma(\mathbf{q}, \omega) = \frac{8\alpha^2\omega^2}{(\omega^2 - \omega_0^2)^2 + (2r\omega)^2} = \mathcal{E}^{\mathrm{DGF}}. \tag{4.13}$$

We perform simulations to assess how well $\mathcal{E}$ can be extracted from time series data of fields [See methods for details]. The estimated $\hat{\mathcal{E}}$ shows excellent agreement with Equation 4.7 (Fig. 4.1). Integrating $\hat{\mathcal{E}}$ gives $\hat{\dot{s}}$, which also shows good agreement with $\dot{s}^{\mathrm{DGF}}$.

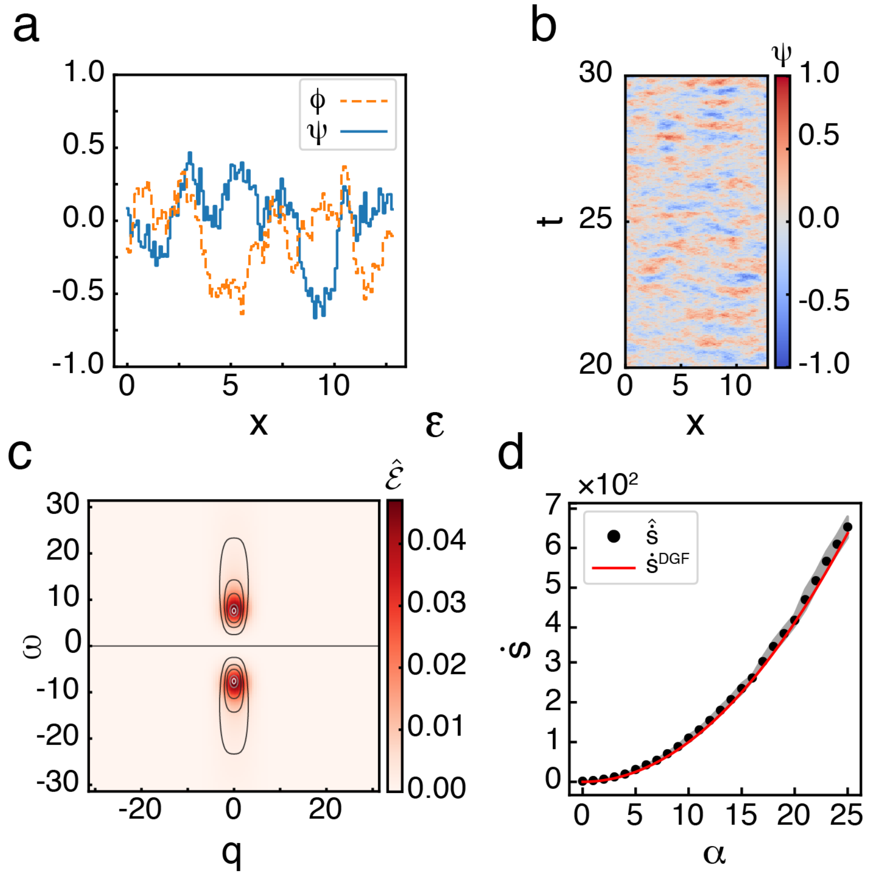

Figure 4.1: **Entropy production rate and entropy production factor are well estimated for driven Gaussian fields.** (a) Snapshot of typical configurations of both fields, ψ (blue solid line) and ϕ (orange dashed line) obeying Equation 4.5 for $\alpha = 7.5$. (b) Subsection of a typical trajectory for one field for $\alpha = 7.5$ in dimensionless units. Colors indicate the value of the field at each point in spacetime. (c) $\hat{\mathcal{E}}$ for $\alpha = 7.5$ averaged over $N = 10$ simulations. Contours show level sets of $\mathcal{E}^{\text{DGF}}$. (d) Measured $\dot{s}$ vs. α for simulations of total time $T = 50$ and length $L = 12.8$. Red line shows the theoretical value, $\dot{s}^{\text{DGF}}$. Mean ± s.d. of $\hat{\dot{s}}$ given by black dots and shaded area. See Table C.1 for all simulation parameters.

Our estimator gives exact results for the driven Gaussian fields because the true path probability functional for these fields is Gaussian. In contrast, the complex patterns seen in nature arise from systems obeying highly non-linear dynamics. For such dynamics, our Gaussian approximation is no longer exact but provides a lower bound on the total irreversibility. To investigate how irreversibility correlates with pattern formation, we study simulations of the Brusselator model for biochemical oscillations [224]. We begin by describing the various dynamical phases of the equations of motion. Next, we calculate $\mathcal{E}$ and $\dot{S}$ for only the reactions before adding diffusion to study the synchronized oscillations that arise in the 1 dimensional reaction-diffusion system.

4.3.3 Reaction-diffusion Brusselator

We use a reversible Brusselator model [224, 225, 226, 221] with dynamics governed by the reaction equations:

$$A \underset{k_1^-}{\overset{k_1^+}{\rightleftharpoons}} X; \quad B + X \underset{k_2^-}{\overset{k_2^+}{\rightleftharpoons}} Y + C; \quad 2X + Y \underset{k_3^-}{\overset{k_3^+}{\rightleftharpoons}} 3X; \tag{4.14}$$

where $\{A, B, C\}$ are external chemical baths with fixed concentrations $\{a, b, c\}$, and all the reactions occur in a volume V (Fig. 4.4a). The system is in equilibrium when the external chemical baths and reaction rates obey $Bk_2^+ k_3^+ = Ck_2^- k_3^-$. When this equality is violated, the system is driven away from equilibrium and exhibits cycles in the (X, Y) plane. Defining

$$\Delta\mu = \log\left(\frac{Bk_2^+ k_3^+}{Ck_2^- k_3^-}\right), \tag{4.15}$$

the Brusselator is at equilibrium when $\Delta\mu = 0$ and is driven into a non-equilibrium steady state when $\Delta\mu \neq 0$. We vary B and C to change $\Delta\mu$ while keeping the product $(bk_2^+ k_3^+)(ck_2^- k_3^-) = 1$, keeping the rate at which reactions occur constant for all $\Delta\mu$ [227].

As $\Delta\mu$ increases, the macroscopic version of Equation 4.14 undergoes dynamical phase transitions. For all $\Delta\mu$, there exists a steady state $(X_{\text{ss}}, Y_{\text{ss}})$, the stability of which is determined by the relaxation matrix, R (Appendix C.5). The two eigenvalues of R , $\lambda_\pm$, divide the steady state into four classes [95]:

1. $\lambda_\pm \in \mathbb{R}_{<0} \rightarrow$ Stable attractor, no oscillations
2. $\lambda_\pm \in \mathbb{C},\ \text{Re}[\lambda_\pm] < 0 \rightarrow$ Stable focus
3. $\lambda_\pm \in \mathbb{C},\ \text{Re}[\lambda_\pm] > 0 \rightarrow$ Hopf Bifurcation, limit cycle
4. $\lambda_\pm \in \mathbb{R}_{>0} \rightarrow$ Unstable repeller

The eigenvalues undergo these changes as $\Delta\mu$ changes, allowing us to consider $\Delta\mu$ as a bifurcation parameter. We define $\Delta\mu_{\text{HB}}$ as the value of $\Delta\mu$ where the macroscopic system undergoes the Hopf bifurcation (Fig. 4.2a).

Non-equilibrium steady states are traditionally characterized by their circulation in a phase space [46, 36, 79, 228, 229]. One may then question how it is possible to detect non-equilibrium effects in the Brusselator when the system's steady state is a stable attractor with no oscillatory component. While this is true for the macroscopic dynamics used to derive $\lambda_\pm$, we simulate a system with finite numbers of molecules subject to fluctuations. These stochastic fluctuations give rise to circulating dynamics, even when the deterministic dynamics do not [225]. We see persistent circulation in the (X, Y) plane when $\lambda_\pm \in \mathbb{R}_{<0}$, with the vorticity changing sign around $\Delta\mu = 0$ (Fig. 4.2).

In order to assess the accuracy of our estimated EPR, $\hat{\dot{S}}$, we calculate an estimate of the true EPR, $\dot{S}_{\text{true}}$, for a simulation of Equation 4.14 by calculating the exact entropy produced by each reaction that occurs in the trajectory [31], and then fitting a line to the cumulative sum (Fig. 4.3, Appendix C.3). We find that $\hat{\dot{S}}$ significantly underestimates $\dot{S}_{\text{true}}$ (note the logged axes in Fig. 4.4c) due to the Brusselator's

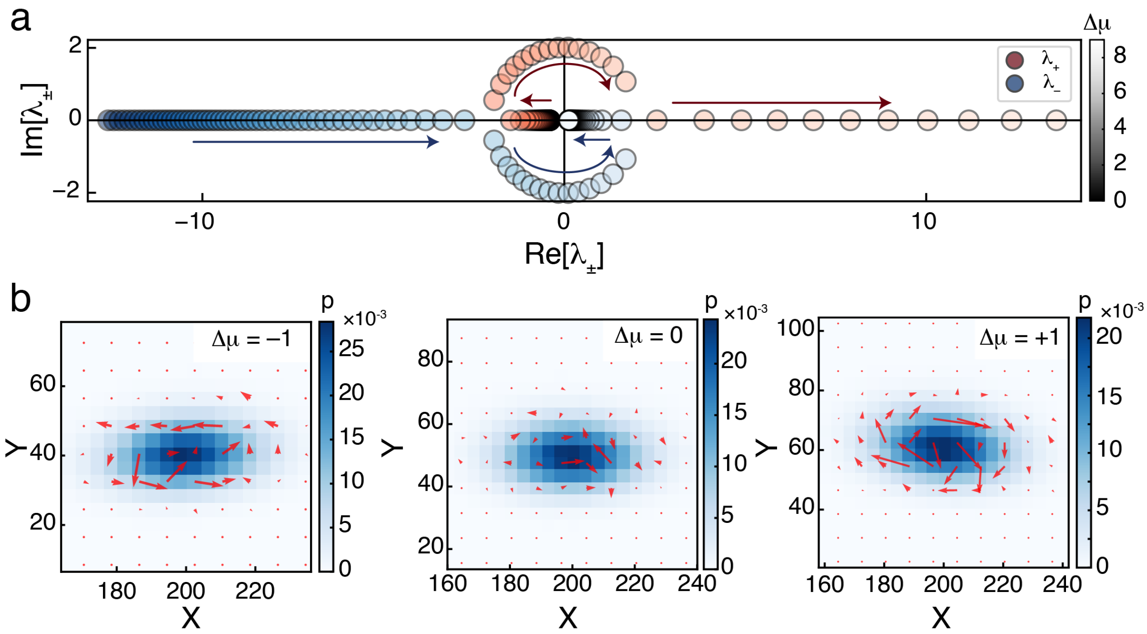

Figure 4.2: **Brusselator dynamics exhibit circulation without macroscopic oscillatory solution.** (a) Eigenvalues of the Brusselator's relaxation matrix, R as a function of the chemical driving force, $\Delta\mu$. $\lambda_\pm$ shown in red and blue, respectively, with each color going from dark to light with increasing $\Delta\mu$. The red and blue arrows serve as guides for the reader to follow the trajectory of $\lambda_\pm$. With our parameters, the stable focus appears at $\Delta\mu = 5.26$ and the Hopf bifurcation occurs at $\Delta\mu_{\text{HB}} = 6.16$. (b) Probability distributions (blue) and probability fluxes (red arrows) for Brusselator simulations with $\Delta\mu = [-1, 0, 1]$, showing the reversal in flux circulation direction at $\Delta\mu = 0$.

hidden dynamics. In the Brusselator, information is lost because the observed trajectories are coarse-grained — they do not distinguish between reactions that take place forward through the second reaction or backwards through the third reaction in Equation 4.14. These pathways would be distinguishable if trajectory of B and C were also observable. Our method relies purely on system dynamics to give $\hat{\dot{S}}$. Equation 4.1 is true only if all microscopic details are captured by trajectories $\mathbf{X}$. If $\mathbf{X}$ is already coarse-grained, multiple microscopic trajectories will be indistinguishable and Equation 4.1 will underestimate the true entropy production rate due to the data processing inequality [230, 231, 211].

In order to account for this, we recalculate $\dot{S}$ by considering the rate at which a

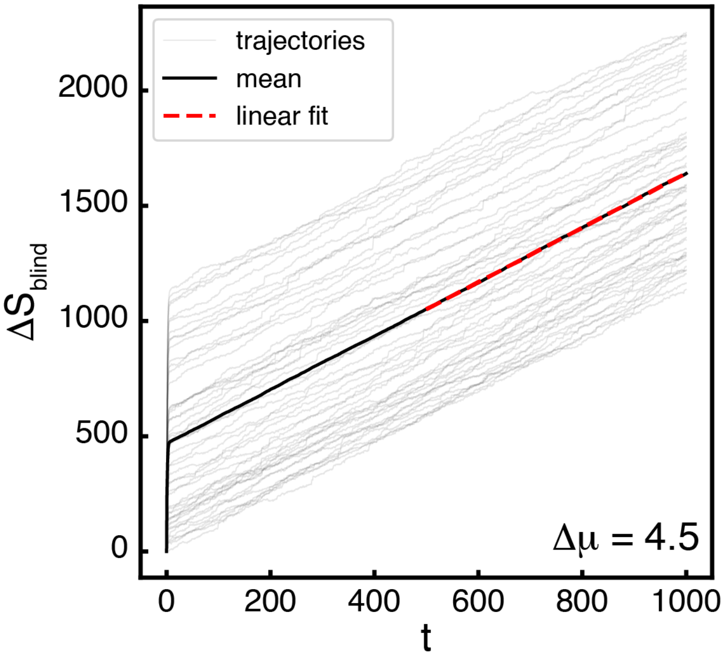

Figure 4.3: **Calculating $\dot{S}_{\text{true}}$ and $\dot{S}_{\text{blind}}$** Fit to (blinded) entropy produced for Brusselator. Light gray lines show the amount of entropy produce as a function of simulation time for $N = 50$ simulations at $\Delta\mu = 4.5$. Each simulation starts at a random initial condition and rapidly approaches the steady state value for (X, Y). This transient trajectory results in the large variation in initial entropy production which depends on how far the system begins from $(X_{\text{ss}}, Y_{\text{ss}})$. Once the system reaches its steady state, the rate of entropy production approaches a steady value. The average of ΔS is taken across all trajectories, and a linear fit to the second half of the resulting mean gives us our value of $\dot{S}_{\text{blind}}$ given in Fig. 4.4. The same method is used to calculate $\dot{S}_{\text{true}}$ as well as $\dot{s}_{\text{blind}}$ and $\dot{s}_{\text{true}}$ for the reaction-diffusion Brusselator model

given transition can occur as the sum over all chemical reactions that give the same dynamics. For example, a transition from $(X, Y) \to (X-1, Y+1)$ can occur via reaction k_2^+ or k_3^- in the Brusselator, each of which produces a different amount of entropy in general. Looking only in the (X, Y) plane, it is impossible to tell which reaction took place. When calculating the entropy produced by only the observable dynamics, the rate of making the transition $(X, Y) \to (X-1, Y+1)$ is $k_{\text{f}} = k_2^+ + k_3^-$, while the rate of making the reverse transition is $k_{\text{r}} = k_2^- + k_3^+$, and the entropy produced is $\log(k_{\text{f}}/k_{\text{r}})$. This estimate of the EPR, which we name $\dot{S}_{\text{blind}}$, is a coarse-graining of $\dot{S}_{\text{true}}$, giving the relation $\dot{S}_{\text{blind}} \leq \dot{S}_{\text{true}}$ [232]. We find that $\dot{S}_{\text{blind}}$ shows excellent agreement with $\hat{\dot{S}}$, indicating that the Gaussian approximation provides a good estimate for the observable dynamics even when the system is highly nonlinear.

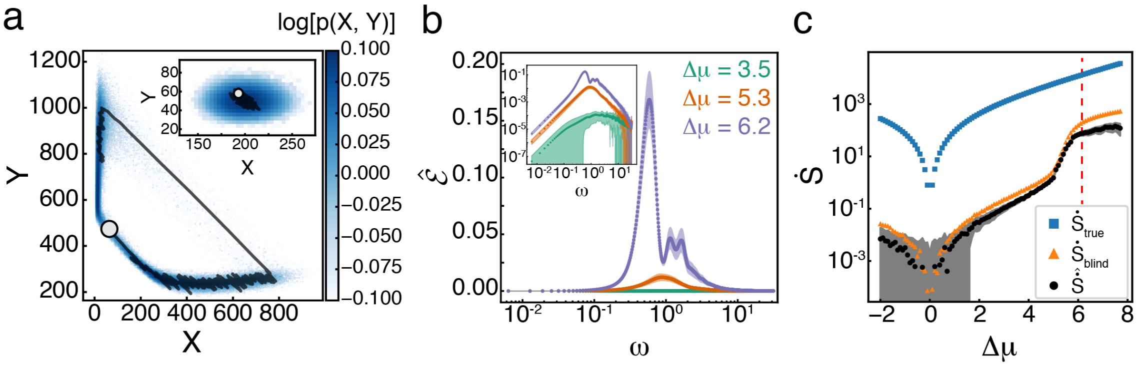

Figure 4.4: **$\dot{S}$ and $\mathcal{E}$ for well-mixed Brusselator.** (a) Typical trajectory in (X, Y) space for $\Delta\mu = 6.2$. The occupation probability distribution is shown in blue, with a subsection of a typical trajectory shown in black. The end of the trajectory is marked by the white circle. Inset shows the same information for the system at equilibrium, where $\Delta\mu = 0$, with the same colorbar as the main figure. (b) $\hat{\mathcal{E}}$ for $\Delta\mu = [3.5, 5.3, 6.2]$ shown in green, orange, and purple, respectively. Shaded area shows mean ± s.d. of $\hat{\mathcal{E}}$ for $N = 50$ simulations. $\hat{\mathcal{E}}$ is symmetric in ω, so only the positive axis is shown. Inset shows the same curves on a log-log scale. (c) $\dot{S}$ as a function of $\Delta\mu$. Blue squares, orange triangles, and black circles show results for $\dot{S}_{\text{true}}$, $\dot{S}_{\text{blind}}$, and $\hat{\dot{S}}$, respectively. Shaded area shows mean ± s.d. of $\hat{\dot{S}}$ for $N = 50$ simulations. Vertical red dashed line indicates $\Delta\mu_{\text{HB}}$. See Table C.2 for all simulation parameters.

To further benchmark our estimator, we calculate $\dot{S}$ using two alternative methods, one based on the thermodynamic uncertainty relation (TUR) [203, 233] and one based on measuring first passage times (MFPT) [234]. The prior method measures a macroscopic current based on a weighted average of a system's trajectory, $j_{\mathbf{d}}$, and estimates the EPR using the TUR for diffusive dynamics, $\dot{S} \geq 2\langle j_{\mathbf{d}}^2 \rangle \left(\tau_{\text{obs}} \text{Var}[j_{\mathbf{d}}]\right)^{-1}$, where $\langle\rangle$ and Var[] denote an ensemble average and variance taken after an observation time τ_{obs} [209]. The latter method requires measuring the MFPT of an observable $\mathcal{O}$ constructed from the system's dynamics to reach a threshold that depends on a user-defined error tolerance. We choose $\mathcal{O}$ and the threshold based on a drift-diffusion approximation for the winding number of the Brusselator. Similarly to $\dot{\hat{S}}$, both of these methods saturate to the true $\dot{S}$ for systems obeying linear dynamics. As such, they also approximate $\dot{S}_{\text{blind}}$, but we find that they provide a looser bound than $\dot{\hat{S}}$ (Fig. 4.5).

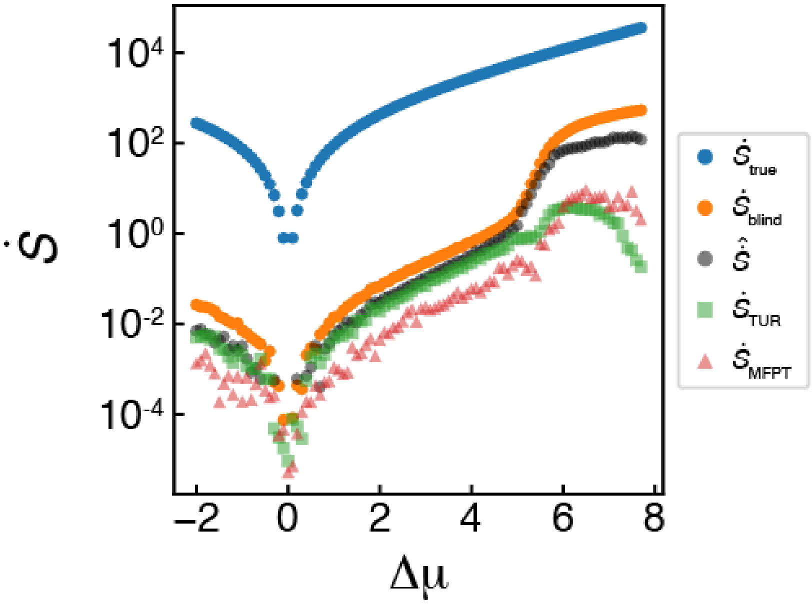

Figure 4.5: **Alternative methods for measuring $\dot{S}$.** Comparison of $\dot{\hat{S}}$ (black dots, same data as in Fig. 2c) with two alternative methods for estimating entropy production rates. $\dot{S}_{\text{TUR}}$ (green squares) is based on the thermodynamic uncertainty relation (TUR), and $\dot{S}_{\text{MFPT}}$ is based on measuring the mean first passage time of an observable. All estimates approximate $\dot{S}_{\text{blind}}$ because they are based only on observables in the (X, Y) plane. Our estimator, $\dot{\hat{S}}$, outperforms the other two estimators, especially beyond the Hopf bifurcation.

Prior to $\Delta\mu_{\text{HB}}$, both $\dot{\hat{S}}$ and $\dot{S}_{\text{blind}}$ show a shift in their trends, but $\dot{S}_{\text{true}}$ does not. The smooth transition is due to the finite system size we employ, and gets sharper as a power law as the system gets larger (Fig. 4.6a). The power law exponent measured from $\dot{\hat{S}}$ is nearly linear, consistent with the Gaussian assumption. The exponent differs from that of $\dot{S}_{\text{blind}}$ because our Gaussian assumption breaks down at the high values of $\Delta\mu$ where the maximum slope occurs (Fig. 4.6b).

The Hopf bifurcation for the Brusselator is supercritical [215], meaning the limit cycle grows continuously from the fixed point when $\Delta\mu - \Delta\mu_{\mathrm{HB}} \ll 1$. Further from the transition point, the trajectory makes a discontinuous transition. At our resolution in $\Delta\mu$, this discontinuous transition is what underlies the shift in $\dot{S}_{\mathrm{blind}}$ of the Brusselator. This same transition is present in $\dot{S}_{\mathrm{true}}$, but is difficult to detect numerically for reasons we explain here. In the deterministic limit, $\dot{S}_{\mathrm{true}} = \Delta\mu \left(J^{\mathrm{F}} - J^{\mathrm{R}}\right)$, where $J^{\mathrm{F}} = b\langle x\rangle k_2^+$ and $J^{\mathrm{R}} = c\langle y\rangle k_2^-$ are the forward and reverse fluxes for transforming a B molecule into a C molecule. $\langle x\rangle$ is a constant, but by numerically integrating the deterministic version for Equation 4.14, we observe a discontinuity in $\langle y\rangle$ above the Hopf bifurcation. However, $J^{\mathrm{F}} \gg J^{\mathrm{R}}$, obscuring the discontinuity in $\dot{S}_{\mathrm{true}}$ (Fig. 4.6c). Upon coarse-graining, we have $\dot{S}_{\mathrm{blind}} = \Delta\mu \left(J^{\mathrm{R}}_{\mathrm{blind}} - J^{\mathrm{F}}_{\mathrm{blind}}\right)$, with $J^{\mathrm{F}}_{\mathrm{blind}} = b\langle x\rangle k_2^+ + \langle x\rangle^3 k_3^-$ and $J^{\mathrm{R}} = c\langle y\rangle k_2^- + \langle x\rangle^2\langle y\rangle k_3^+$. These two terms are equal to each other for $\Delta\mu < \Delta\mu_{\mathrm{HB}}$ and diverge continuously when $\Delta\mu \gtrapprox \Delta\mu_{\mathrm{HB}}$, followed by the relatively large discontinuity in $J^{\mathrm{R}}_{\mathrm{blind}}$ (Fig. 4.6c, inset).

One gains further insight into the dynamics through the transition by studying $\hat{\mathcal{E}}$ (Fig. 4.4b). For $\Delta\mu < \Delta\mu_{\mathrm{HB}}$, $\hat{\mathcal{E}}$ exhibits a single peak that increases in amplitude while decreasing in frequency as $\Delta\mu$ increases. Above $\Delta\mu_{\mathrm{HB}}$, the peak frequency makes a discontinuous jump, the magnitude of the peak grows rapidly, and additional peaks at integer multiples of the peak frequency appear due to the non-linear shape of the limit cycle attractor. These harmonics are expected for dynamics on a non-circular path. For $\Delta\mu < \Delta\mu_{\mathrm{HB}}$, the magnitude of the peak is independent of system volume, while it gains a linear volume dependence in the limit cycle. The width of the peak is also maximized near the transition, reflecting a superposition of frequencies present in the trajectories (Fig. 4.7).

To investigate how dynamical phase transitions manifest in the irreversibility of spatially extended systems, we simulate a reaction-diffusion Brusselator on a 1 dimensional periodic lattice with L compartments, each with volume V, spaced a

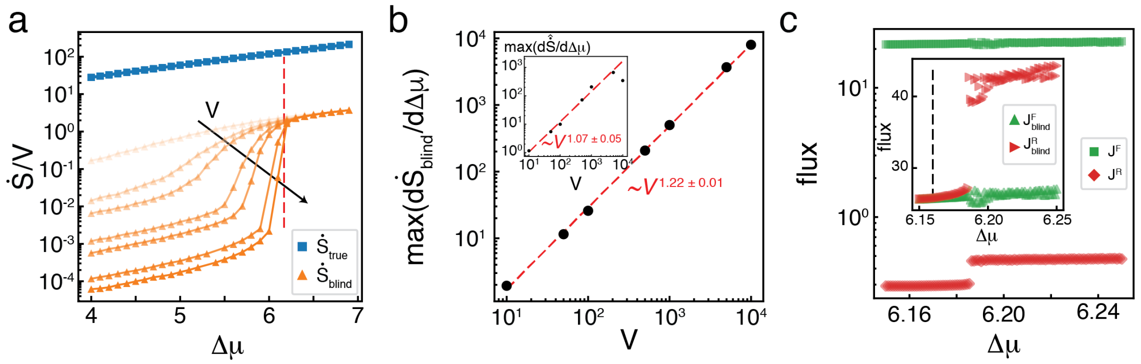

Figure 4.6: **Finite size scaling of $\dot{S}$** (a) $\dot{S}_{\mathrm{true}}/V$ (blue squares) and $\dot{S}_{\mathrm{blind}}/V$ (orange triangles) for system volumes $V = [10, 50, 100, 500, 1000, 5000, 10000]$, showing an increasingly sharp transition in $\dot{S}_{\mathrm{blind}}$, but not in $\dot{S}_{\mathrm{true}}$. $\dot{S}_{\mathrm{blind}}$ shows no volume dependence below the transition, and is linear dependent on V above it. Vertical red dashed line shows $\Delta\mu_{\mathrm{HB}}$. (b) Maximum value of $\partial\dot{S}_{\mathrm{blind}}/\partial\Delta\mu$ shows a power-law dependence with volume. Inset shows the same measurement for $\partial\dot{\hat{S}}/\partial\Delta\mu$. (c) Forward and reverse fluxes, J^{F} (green squares) and J^{R} (red diamonds), obtained from numerical integration of deterministic equations of motion for the Brusselator. Inset shows $J^{\mathrm{F}}_{\mathrm{blind}}$ (green upright triangles) and $J^{\mathrm{R}}_{\mathrm{blind}}$ (red rightward triangles). Vertical black dashed line shows $\Delta\mu_{\mathrm{HB}}$.

distance h apart. The full set of reactions are now

$$\begin{gathered} A_i \underset{k_1^-}{\overset{k_1^+}{\rightleftharpoons}} X_i; \quad B_i + X_i \underset{k_2^-}{\overset{k_2^+}{\rightleftharpoons}} Y_i + C_i; \quad 2X_i + Y_i \underset{k_3^-}{\overset{k_3^+}{\rightleftharpoons}} 3X_i; \\ X_i \underset{d_X}{\overset{d_X}{\rightleftharpoons}} X_{i+1}; \qquad Y_i \underset{d_Y}{\overset{d_Y}{\rightleftharpoons}} Y_{i+1}; \qquad i \in [1, L] \end{gathered} \tag{4.16}$$

where $d_j = D_j/h^2$, and D_j is the diffusion constant of chemical species $j = \{X, Y\}$. Qualitatively different dynamics occur based on the ratio D_X/D_Y. $D_X/D_Y \ll 1$ yields static Turing patterns [94, 97]. We focus on the $D_X/D_Y \gg 1$ regime which exhibits dynamic, excitable waves. All values of $\{a_i, b_i, c_i\}$ are kept constant in each compartment.

In the steady state, the reaction-diffusion Brusselator has the same dynamics as the well mixed Brusselator, and so it is not surprising that it's EPR curve as a function of $\Delta\mu$ is similar. However, unlike the well-mixed system, the Hopf bifurcation signals the onset of qualitatively distinct dynamics in the reaction-diffusion system. Prior to the Hopf bifurcation, there are no coherent, spatial patterns in the system's dynamics (Fig. 4.8a). Above the Hopf bifurcation, system-spanning waves begin to emerge that synchronize the oscillations across the system (Fig. 4.8b). Following standard methods [235, 236], we define the synchronization order parameter, $0 \leq r < 1$, using

$$r e^{i\psi} = \frac{1}{T} \int_0^T dt \; \frac{1}{M} \sum_{j=1}^{M} e^{i\theta_j(t)} \tag{4.17}$$

where $\theta_j(t)$ is the phase of the oscillator at position x_j and time t, defined with respect to the center of mass of the trajectory:

$$\theta_j(t) = \arctan \frac{Y_j - \langle Y_j \rangle}{X_j - \langle X_j \rangle}. \tag{4.18}$$

M is the number of oscillators (here, the number of lattice sites in our simulation), and T is the temporal extent of the data. ψ denotes the overall phase, and r is close to zero in the asynchronous phase and approaches one as the oscillators synchronize.

Below $\Delta\mu_{\mathrm{HB}}$, r is low and rapidly approaches one as the system approaches the macroscopic bifurcation point (Fig. 4.8c). Like $\dot{S}$, this transition occurs more sharply and closer to $\Delta\mu_{\mathrm{HB}}$ as the system size increases, approaching the discontinuous transition to the limit cycle behavior (Fig. 4.8c, inset) [237]. Throughout these changes, the system is driven further from equilibrium, as reflected in the increasing $\hat{\dot{s}}$ (Fig. 4.8d). The shift to collective behavior is not reflected in $\dot{s}$ as it is almost identical to $\dot{S}$ found for the well-mixed Brusselator. Instead, $\mathcal{E}$ carries the signature of the dynamical phase transition. For $\Delta\mu < \Delta\mu_{\mathrm{HB}}$, $\hat{\mathcal{E}}$ shows peaks at high wavenumbers, reflecting that irreversibility is occurring incoherently over short length scales. Above $\Delta\mu_{\mathrm{HB}}$, as the system shows synchronized oscillations, there is an abrupt shift in the peaks of $\hat{\mathcal{E}}$ to low q, indicating that this collective behavior carries the majority of the irreversibility (Fig. 4.9b,c). We also infer that the collective behavior is partially composed of traveling waves due to the streaks in $\hat{\mathcal{E}}$ (Fig. 4.9b). The slight offset in the transition occurs for high values of $\Delta\mu < \Delta\mu_{\mathrm{HB}}$ where small regions synchronize for short periods of time, but system wide oscillations are not observed (Fig. 4.10a). Furthermore, the transition moves closer to the macroscopic transition point with increased volume of the individual compartments (Fig. 4.10b).

4.4 Conclusion

Previous work has investigated the behavior of $\dot{S}$ at thermodynamic phase transitions with the work of [214] finding general signatures of discontinuous phase transitions in $\dot{S}$ which agree with our results. While [218] found $\dot{S}$ to have a discontinuity of its first derivative with respect to $\Delta\mu$ in a slightly modified version of the well-mixed Brusselator, work on the same system presented here did not find any non-analytic behavior in $\dot{S}_{\mathrm{true}}$ [221]. We show that a discontinuous phase transition exists in our model, but the magnitude of the discontinuity is small and difficult to detect in $\dot{S}_{\mathrm{true}}$ and is more easily seen in the coarse-grained $\dot{S}_{\mathrm{blind}}$ (Fig. 4.6). Further, other spectral decompositions of the dissipation rate either assume a particular form for the underlying dynamics [219] or require the measurement of a response function in addition to the correlation function [222], which is often difficult to perform in experiments.

Here, we illustrated that the total irreversibility rate cannot distinguish between the dynamical phase transitions in the well-mixed and the spatially extended Brusselator. While the EPR quantifies the emergence of oscillations, the synchronization of the oscillations across space is only captured in $\mathcal{E}$ by its peak shifting from high to low wavenumber (Fig. 4.9). By simulating systems with increasing compartment volumes, this shift occurs closer to the macroscopic transition point (Fig. 4.10b), similarly to the increasing sharpness of the shift in $\dot{S}$ for the well-mixed Brusselator (Fig. 4.6). Thus, synchronization is intimately related to the emergence of oscillations. We hypothesize that synchronization occurs due the presence of a slow segment of the Brusselator dynamics (Fig. 4.4a). The time spent in the slow portion of the dynamics allows neighboring oscillators to reduce their relative phase through their diffusive coupling, allowing previously out-of-sync lattice sites to synchronize via the low-cost mechanism of diffusion. Once the oscillations are synchronized, diffusion between lattice sites at equal concentrations is an equilibrium process and does not produce entropy.

In summary, we have introduced the entropy production factor, $\mathcal{E}$, a dimensionless, scalar function that quantifies irreversibility in macroscopic, non-equilibrium dynamics by measuring time-reversal symmetry breaking in the cross-covariances between multiple variables. Integrating $\mathcal{E}$ gives a lower bound on the net entropy production rate, $\dot{s}$. Calculating $\mathcal{E}$ does not require knowledge about the form of the underlying dynamics and is easy to calculate for many types of data, including both random variables, such as the positions of driven colloidal particles [238], and random fields, such as spatially heterogeneous protein concentrations in cells [110]. Furthermore, we stress that we are only able to resolve the irreversibility present in the observable dynamics of our chemical example. As discussed above, the presence of hidden dynamics will provide underestimates of irreversibility measured via Equation 4.1 due to the data processing inequality [44]. Using other observable information, such as asymmetric transition rates [239] or the ratio of populations in observed states under stalled conditions [231] in Markov jump processes, can give tighter bounds on the entropy produced when unobserved, dissipative processes are present. While the examples considered here are simulations of 1+1 dimensional fields, there is nothing inherently different in the methodology if one were to analyze experimental data in 2 or 3 spatial dimensions, such as the 3+1 dimensional time series data attained using lattice-light sheet microscopy [240].

In active matter, both living and non-living, the non-equilibrium dissipation of energy manifests in both time and space. With the method introduced here, compatible with widely-used computational and experimental tools, we provide access to these underexplored modes of irreversibility that drive complex spatiotemporal dynamics.

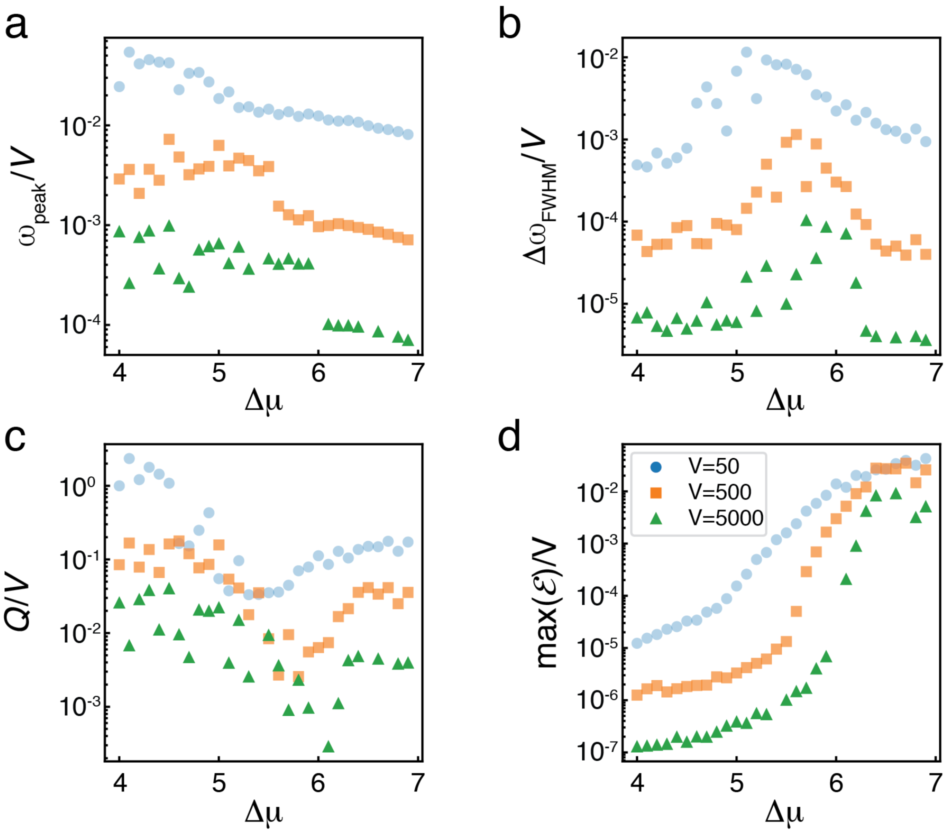

Figure 4.7: **Finite size scaling of $\mathcal{E}$ of Brusselator.** (a) Normalized frequency of maximum of $\mathcal{E}$, ω_{peak}/V is independent of V, but the jump from high to low frequency occurs more sharply and occurs closer to $\Delta\mu_{\text{HB}}$ as V increases. (b) Normalized full-width half-maximum (FWHM) of peak in $\mathcal{E}$, $\Delta\omega_{\text{FWHM}}$, is independent of V and is maximized around the transition point, reflecting the increased fluctuations near the phase transition. The location of the peak moves closer to $\Delta\mu_{\text{HB}}$ as V increases. (c) The normalized quality factor of $\mathcal{E}$, $Q/V = \omega_{\text{peak}}/\Delta\omega_{\text{FWHM}}V$, is independent of system size, and has a minimum at the transition point. (d) The normalized maximum value of $\mathcal{E}$ is independent of V below the transition, and gains a linear dependence on V above it, similar to $\dot{S}_{\text{blind}}$.

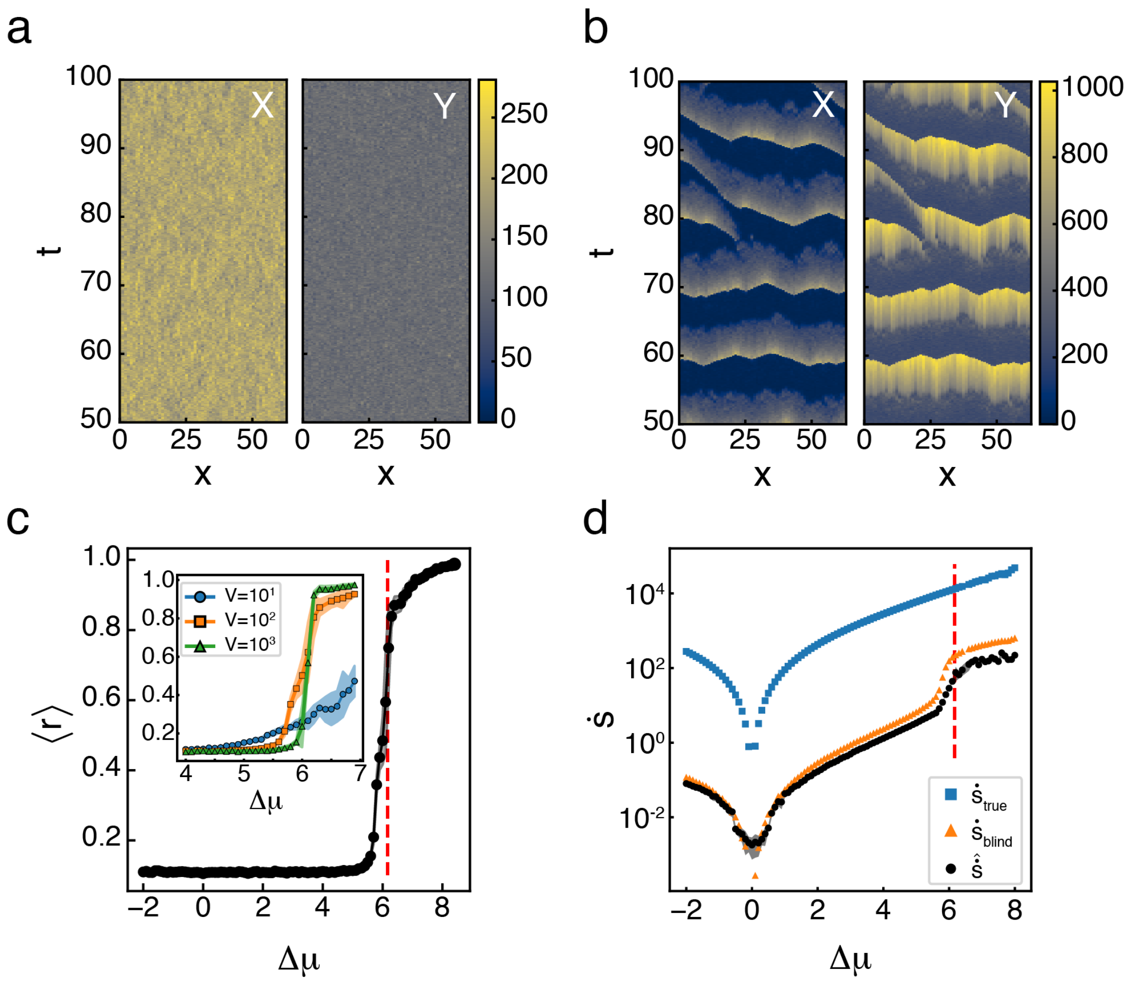

Figure 4.8: **1 dimensional Reaction-diffusion Brusselator synchronizes above Hopf bifurcation** (a) Subsection of a typical trajectory for $X(x,t)$ and $Y(x,t)$ for (a) $\Delta\mu = 3.5$, below the Hopf Bifurcation and (b) $\Delta\mu = 6.2$, above it. Color indicates the local number of the chemical species. (c) Synchronization order parameter, $\langle r \rangle$, as a function of $\Delta\mu$. Vertical red dashed line indicates $\Delta\mu_{\mathrm{HB}}$. Inset shows the same measurement for volumes $V = \{10^1, 10^2, 10^3\}$ shown by blue circles, orange squares, and green triangles, respectively, at each lattice site over a smaller region of $\Delta\mu$. Dots and shaded areas show mean ± s.d. of $N = 10$ simulations. (d) $\dot{s}$ as a function of $\Delta\mu$. Blue squares, orange triangles, and black circles show results for $\dot{S}_{\mathrm{true}}$, $\dot{S}_{\mathrm{blind}}$, and $\hat{\dot{S}}$, respectively. Shaded area shows mean ± s.d. of $N = 10$ simulations. Vertical dashed red line indicates $\Delta\mu_{\mathrm{HB}}$. See Tables C.3 & C.4 for all simulation parameters.

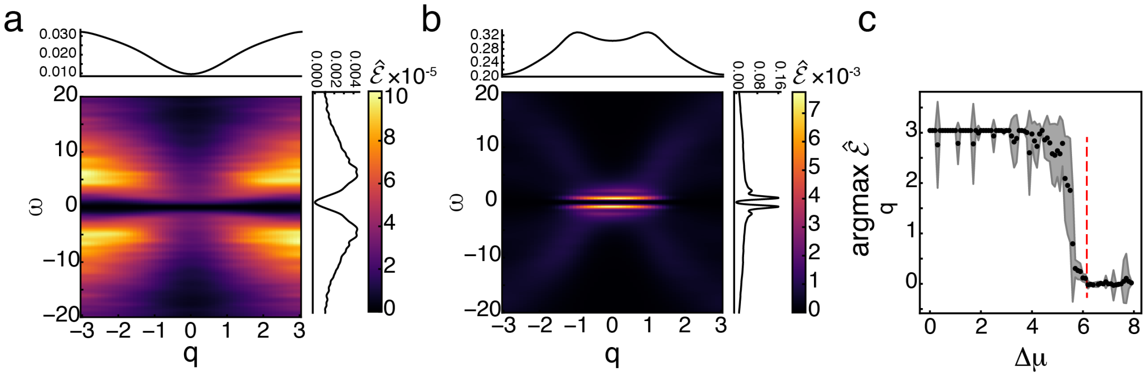

Figure 4.9: **Entropy production factor and macroscopic dynamics** (a) $\mathcal{E}$ averaged over $N = 10$ simulations for $\Delta\mu = 4.0$, i.e. $\Delta\mu < \Delta\mu_{\mathrm{HB}}$. Line plots on top and left of figure show marginals over ω and q, respectively. (b) Similar to (a), but for $\Delta\mu = 6.2$, i.e. $\Delta\mu > \Delta\mu_{\mathrm{HB}}$. (c) Wavenumber, q, that maximizes $\hat{\mathcal{E}}$ as a function of $\Delta\mu$. Vertical dashed red line shows $\Delta\mu_{\mathrm{HB}}$. Black dots and shaded area show mean ± s.d. over $N = 10$ simulations.

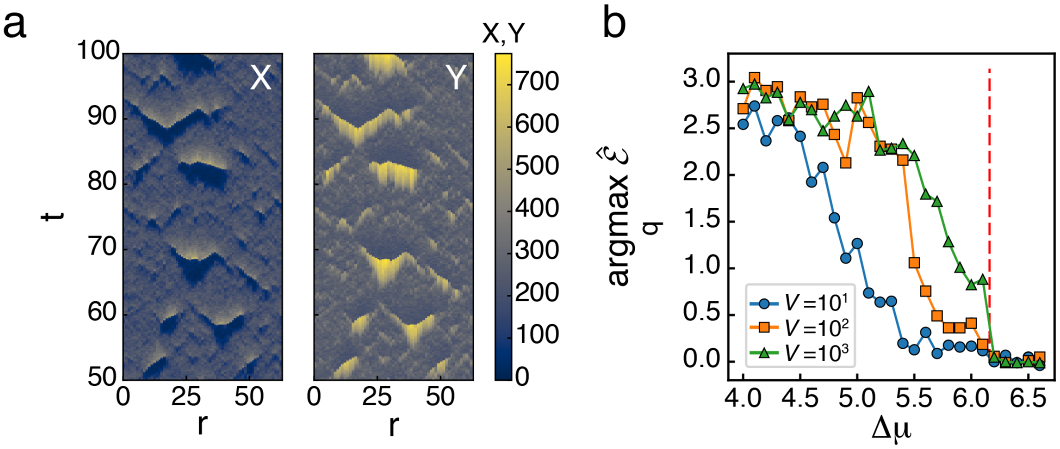

Figure 4.10: **Transiently synchronized dynamics in the reaction-diffusion Brusselator and finite-size scaling in $\mathcal{E}$.** (a) Typical trajectory of a reaction-diffusion Brusselator system just below the Hopf bifurcation, at $\Delta\mu = 5.8$ and $V = 100$. See some flashes on collective behavior, but it does not span the entire system, showing why $\mathcal{E}$ has peaks somewhere between $q = 0$ and the maximum in Fig. 5c. (b) Wavenumber q that maximizes $\hat{\mathcal{E}}$ for the reaction-diffusion Brusselator for compartment volumes $V = \{10^1, 10^2, 10^3\}$ shows a sharper transition that gets closer to $\Delta\mu_{\mathrm{HB}}$ (red line) as the volume increases.

Chapter 5

Conclusions and future directions

The work presented in this thesis provides a framework with which to understand seemingly disparate biological processes. It argues that energy dissipation, as quantified by entropy production, can be thought of as a control parameter to tune distinct dynamical and mechanical phases in living matter, in analogy to the temperature in equilibrium systems. I illustrated that the entropy production rate in the bending fluctuations of individual actin filaments within a network is indicative of the dynamical state of the network as a whole, with a maximal entropy production rate corresponding to a non-equilibrium steady state. Next, I showed that irreversibility in mechanosensitive binding kinetics correlates with the onset of a mechanically rigid phase of an active actin network, and is uncorrelated with a state associated with an increased amount of flow. Finally, I showed that total irreversibility reflects the onset of oscillations at a Hopf Bifurcation of a biochemical oscillator, but that the effects of synchronization are contained in the newly introduced entropy production factor.

Future work will involve the use of the entropy production factor to characterize spatiotemporal oscillations in cells. For example, egg cells from the African clawed frog, a highly studied model organism in developmental biology, exhibit excitable wave dynamics induced by the interactions between actin and Rho, a membrane-bound signaling protein that is, among other things, an upstream regulator of actomyosin activity [110, 241]. These excitable waves are hypothesized to be important for the proper location of the cytokinetic ring at the equator of the cell. This system therefore couples chemical wave behavior of Rho to mechanical deformations of actomyosin to properly integrate spatial information in order to properly assemble a complex machine critical for the development. This represents an ideal use case for the entropy production factor to gain insight into the energetic costs of cell division.

In reporting my results, I have placed particular emphasis on the ability to use entropy production as a way to make fundamental insights into biological function. Most work in this field uses living matter to test equalities and bounds derived using non-equilibrium statistical mechanics, but ignores the ability for physics to equally contribute to understanding biology. However, spatiotemporal biological phenomena also inspired the creation of the entropy production factor, an advance that sits squarely within the realm of theoretical physics. Thus, the avenue for discovery in biological physics is a two-way street. Applying tools from physics to biology can give insight into mechanisms used by living matter to accomplish complex tasks. Simultaneously, biology can give insight into the dynamics possible for systems driven far from equilibrium, which have been notoriously difficult to enumerate. Biology provides an ideal class of systems to guide our study of non-equilibrium systems without the need to go to extreme environmental conditions. I believe that some of the most important contributions to physics and biology in the next few decades will come from those who are firmly planted at their interface.

Appendix A

Appendix for Chapter 2

A.1 Nematic order parameter calculations

The nematic order parameter q is calculated using custom Matlab code available here. First, a director field is created from images of fluorescently labeled F-actin [242]. Briefly, fluorescent images are divided into small, overlapping 3.5 μm by 3.5 μm windows, and the local F-actin orientation (director) is calculated for each window, yielding an F-actin director field over an image. To determine the local F-actin director, each window is Gaussian filtered and transformed into Fourier space using a 2D fast Fourier Transform (FFT). The axis of the least second moment was calculated from the second-order central moments of the transformed window, and the angle of the local F-actin director is defined as orthogonal to this axis. Next, the local degree of alignment is calculated between adjacent windows within 33 kernels. The local nematic order is calculated for the central window in each kernel using the modified order parameter equation $q = 2\left\langle \cos^2(\theta) - 1/2 \right\rangle$, where θ is the difference in F-actin orientation between the central window and the 8 surrounding windows. This process is repeated for all possible 33 kernels over an image, yielding a nematic director field with defined director magnitude and orientation for each window over an image. Perfect alignment between adjacent regions within an F-actin network results in an order parameter equal to one. Conversely, orientation differences of 45° (maximum expected for quasi-2D F-actin network) between adjacent regions of the network result in an order parameter equal to zero.

A.2 Filament Normal Modes

Consider a filament that is tracked over time. The tangent angle along the arc length of the filament can be decomposed into an infinite series of orthogonal functions, $\psi_n(s)$

$$\theta(s,t) = \sum_{n=1}^{\infty} a_n(t)\psi_n(s) \tag{A.1}$$

The orthogonal functions are given by solving the eigenvalue problem for the fourth order, linear partial differential equation for the bending of a slender rod with length L (see section IV of [125])

$$\frac{\mathrm{d}^4\psi_n}{\mathrm{d}s^4} = \lambda_n \psi_n \tag{A.2}$$

Which yields the solutions (with $s \in [-L/2, L/2]$)

$$\psi_n(s) = \begin{cases} \frac{\cos(k_n s/L)}{\cos(k_n/2)} + \frac{\cosh(k_n s/L)}{\cosh(k_n/2)} & n = 1,3,5\ldots \\ \frac{\sin(k_n s/L)}{\sin(k_n/2)} + \frac{\sinh(k_n s/L)}{\sinh(k_n/2)} & n = 2,4,6\ldots \end{cases} \tag{A.3}$$

where $k_n \approx (n+1/2)\pi$. By inverting (A.1), we can determine the state of the filament at each time by its position in the phase space spanned by its expansion coefficients, $\vec{a}(t) = \{a_i(t)\}$.

A.3 Calculating entropy produced from bending modes

To calculate Δs_{tot}, we begin with a time series of the coefficients obtained by expanding the tangent angles along the filament's arc length as described in Appendix A.2: $\{a^i_\alpha\}$. From here on, let Greek characters define spatial indices, and Latin letters define temporal indices. Taking the time integral of 1.35, the total entropy produced is

$$\Delta s(t)_{tot} = \int_0^t \mathrm{d}\tau \, \dot{\vec{a}}^T(\tau) \mathbf{D}^{-1} \vec{v}^{ss} \tag{A.4}$$

For simplicity, we assume that the diffusion matrix is a scalar and has no spatial dependence, $\mathbf{D} = D_0$. Discretizing (A.4), we find the change in entropy at each time point j as (using Einstein notation to imply sums over repeated indices)

$$\Delta s^j_{tot} = D_0^{-1} \sum_\Omega \dot{a}^j_\mu v^{ss}_\mu \tag{A.5}$$

where the sum over Ω indicates a sum over the entire phase space, as both $\dot{a}^j_\mu$ and v^{ss}_μ are vector fields, with values at each point in space. We are left to calculate two quantities: $\dot{a}^j_\mu$ and v^{ss}_μ. It is important to note that, in order to calculate a velocity from (1.22), one must use the *Stratanovich interpretation* [12]. Therefore, any velocity is evaluated as a mid-point:

$$\dot{x} = \frac{x(t + \delta t) - x(t - \delta t)}{2\delta t} \tag{A.6}$$

Using the Ito interpretation would instead give the *force* on the particle.

- Calculating v^{ss}_μ
  - To calculate the steady state velocity throughout phase space, the entire

space is first discretized into bins of size Δx. Each position along the trajectory is then assigned to a bin, α. The velocity at that point is then calculated in the Stratanovich sense mentioned above. This process is repeated for the entire trajectory. After every velocity has been assigned to each visited bin α, the average velocity is found in each bin by summing all the velocities assigned to that bin and dividing by the number of times that bin was visited. This gives

$$v_\mu^{ss}(\alpha) = \{E\left(\frac{a_\mu^{i+1} - a_\mu^{i-1}}{2\delta t}\right) |a_\mu^i \in \alpha\} \tag{A.7}$$

- Calculating $\dot{a}_\mu$
  - The instantaneous velocity is calculated in exactly the same way that each instantaneous velocity is calculated above to find v_μ^{ss}. The only difference between the two is that v_μ^{ss} is the average taken over all time.

Looking at (A.5), the calculation is done for every time point (except the first and last one, to allow the center difference for the velocity to be taken). The sum over Ω is reduced to a simple product because, at any given time, the system's velocity is at a single point, not distributed over space.

More specifically, the steps taken are:

1. Set the parameters used
   (a) D_0, diffusion constant
   (b) Δa, bin size
   (c) δt, time step between points along trajectory
   (d) a_μ, the modes to consider

2. Calculate the steady-state velocity field using the entire trajectory as described above
3. Find the velocity at t_2 using (A.6)
4. Find the bin α that the system is occupying at t_2
5. Take the dot product between $\dot{a}_\mu^2$ and v_μ^{ss}, and multiply by D_0^{-1}
6. Repeat for all time points up to the second to last one.

This gives the total change in entropy at each time t_j, Δs_{tot}^j. To get the change in entropy along a trajectory of length N, we simply take a moving sum

$$^{(N)}\Delta s_{tot}^j = \sum_{i=j}^{j+N} \Delta s_{tot}^i \tag{A.8}$$

A.4 Testing Detailed Fluctuation Theorem (DFT)

To verify that the entropy being calculated is correct, it is useful to check that it fulfills Equation 1.30. In order to get sufficient statistics while maintaining the same analysis pipeline, we consider freely available data on beating axonemes [1, 243]. Once Δs_{tot}^j is found along the trajectory as described above, the distribution of values is found as shown in Fig A.1. A small region around $\Delta s = 0$ is chosen to ensure sufficient statistics in the negative side of the axis. Then, the logarithm of the ratio of probabilities is plotted as a function of Δs. If the DFT is satisfied, the result should be a line of slope 1. The results are shown in Fig A.1 for a maximum magnitude of $|\Delta s| = 1$, using the same parameters as in the caption of Fig A.1. These result in most filaments satisfying the DFT.

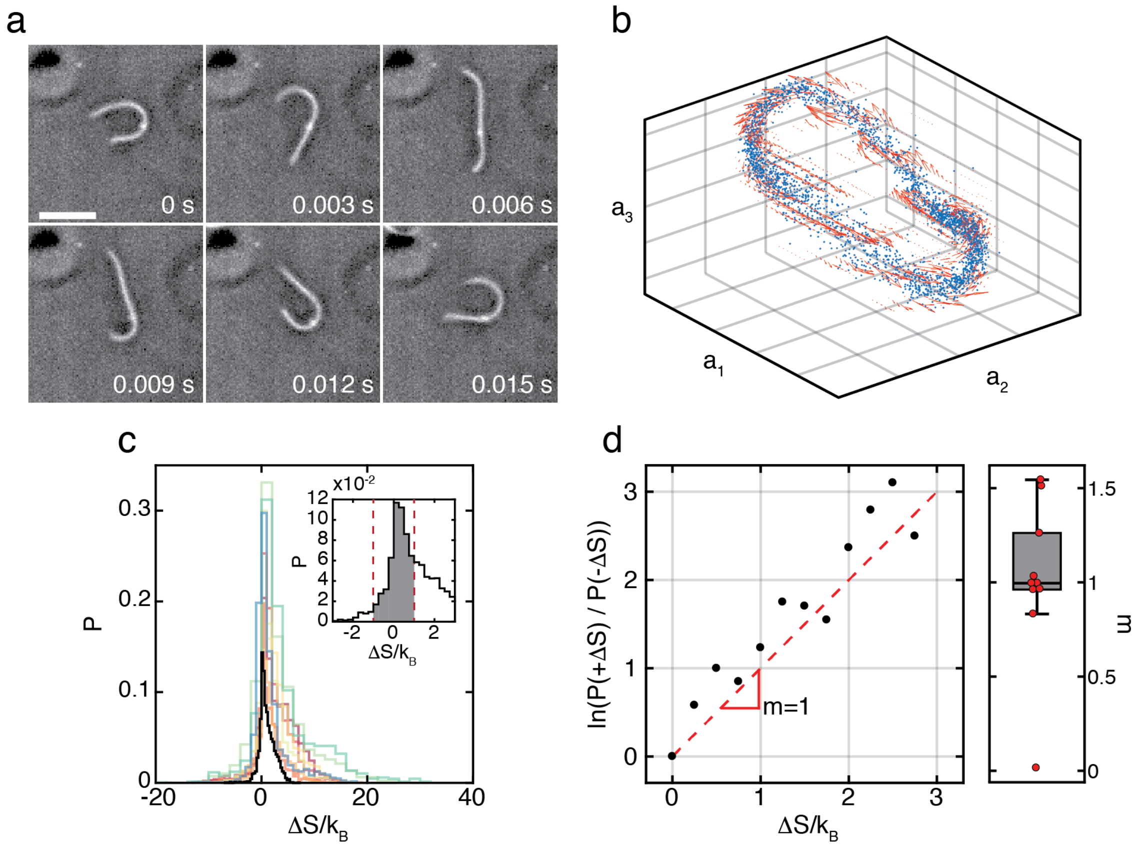

Figure A.1: **Testing the detailed fluctuation theorem for filament bending modes.** (a) Screenshots showing a single period of motion for a beating axoneme, from [1]. (b) Resulting phase space locations (blue) and velocities (red) in a 3-dimensional subspace of the bending mode coefficient phase space for the axoneme shown in (a). (c) Probability distributions of entropy production for 10 axonemes. Inset shows a zoom in on the histogram in black. The red dotted lines indicate the region around zero where Equation 1.30 is tested. (d) Results for single distribution shown in the inset of (c), with red dotted line showing the theoretical prediction of a line with slope 1. The boxplot and individual points on the right show the fitted slopes for all 10 axonemes analyzed.

A.5 Anisotropic velocity autocorrelation calculation

The velocity autocorrelation functions in Fig. 2.5b are calculated as follows. For each frame in a movie of an F-actin network, the velocity and alignment fields are calculated as described in the main methods. Each vector is then decomposed into components parallel and perpendicular to the alignment found at its grid point, defined as $v^{\parallel}(\mathbf{x},t) = |\mathbf{n}\cdot\mathbf{v}|$, and $v^{\perp} = |\mathbf{v}| - v^{\parallel}$, respectively. The spatial mean is then subtracted to remove short and long wavelength correlations, giving $\delta v^{\perp}(\mathbf{x},t) = v^{\perp} - \left\langle v^{\perp}\right\rangle_{\mathbf{x}}$, and similarly for $v^{\parallel}$. The velocity autocorrelation function is then given by

$$C_{vv}^{\perp}(r,t) = \frac{1}{A}\int d\mathbf{x}d\mathbf{x}'\left[\delta v^{\perp}(\mathbf{x},t)\delta v^{\perp}\left(\mathbf{x}',t\right)\delta\left(r - |\mathbf{x}-\mathbf{x}'|\right)\right] \tag{A.9}$$

where A is the total area of the field of view and $\delta()$ is the Dirac delta function. A similar expression is used for $C_{vv}^{\parallel}$. The anisotropic autocorrelation function is defined as the temporal average of the difference between the normalized perpendicular and parallel autocorrelations, as given by Equation 2.3

Appendix B

Appendix for Chapter 3

B.1 AFINES Simulation

The coarse-grained interactions between actin filaments and active motors were simulated using the simulation package AFINES [137]. This simplified polymer dynamics package enabled simulations of large networks and did not require the mechanistic detail and precision made possible with the MEDYAN or Cytosim packages [180, 129]. Constituent particles evolved via overdamped Langevin dynamics at a fixed temperature in 2D with no volume exclusion. Actin filaments were modeled as polar beadspring filaments with finite stretching stiffness k_{a} and bending modulus κ_{B} and have a persistence length and equilibrium contour length equal to 10 μm. Motors were modeled as Hookean springs with spring constant km that dynamically bind and unbind to actin filaments with finite on and offrates k_{on} and k_{off} respectively.

Motors bind to a nearby filament within a distance of $\sqrt{k_{\mathrm{B}}T/k_{\mathrm{m}}}$ with a probability $P_{\mathrm{on}} = k_{\mathrm{on}}\Delta t \times \min[1, \exp(\Delta E/k_{\mathrm{B}}T)]$, where min[] is the Metropolis factor for accepting the binding event, Δt is the discrete time-step of the simulation, k_{on} is the defined on-rate, and $\Delta E = E_{\mathrm{f}} - E_{\mathrm{i}}$ is the energy change in moving from a state with initial energy E_{i} to a state with final energy E_{f}.

The definition of a catch bond describes $k_{\text{off}}^{\text{eff}}$ exponentially depending on F and ξ and a sharp unbinding transition at $F = F_{\text{max}}$, thus capturing the essential features of a broad class of catchbonds [86] both within biology [185] and suggested to be ubiquitous to all nonlinear bonds [244]. As Factin networks cannot sustain a compressive load on bonds, $k_{\text{off}}^{\text{eff}} = k_{\text{off}}$ when $F < 0$. Unless otherwise stated, F_{max} is set sufficiently high such that $F < F_{\text{max}}$ for all motors at all times. This expression for the k_{off} is a lowforce approximation to a more general expression for catch bonds that include a transition to slip bonds at high forces, a phenomenon seen in singlemolecule pulling experiments for molecular catch bonds [170]. This low force approximation has been used to model the dynamics of catch bond crosslinkers *in vivo* [3] and gives simulations that replicate results seen in experiments. In particular, *in vitro* experiments of reconstituted actomyosin networks also showed a nonmonotonic behavior of network strain with increasing myosin concentration, an experimental analog for increasing active stresses (Figures B.1&B.2). Further, it was also observed that experiments of actomyosin networks in the presence of the slip bond crosslinker fascin [7] evolved into asters, similar to simulations with ideal motors, while experiments containing the catch bond crosslinker αactinin [3, 2] evolved to an arrested state, similar to simulations with high values of $|\xi|$.

When bound, a motor moves towards the barbed end of a filament with a baseline velocity v_0 that decreases linearly with the applied load until a stall force F_{stall} is reached, that is $v(F) = v_0(1 - |F|/F\text{stall})$, with $v(|F| > F_{\text{stall}}) = 0$.

Filaments and motors were deposited randomly within a box of size $L \times L$ ($L = 50$ μm) with periodic boundary conditions at time $t = 0$. There are no steric forces between particles, so no equilibration was necessary. All simulations were run at a filament density of 0.4 filaments per μm^2. In the model, the bending and stretching stiffness of motors and filaments were finite but decreased below physically realistic values for computational feasibility and the energy input through motor stepping was

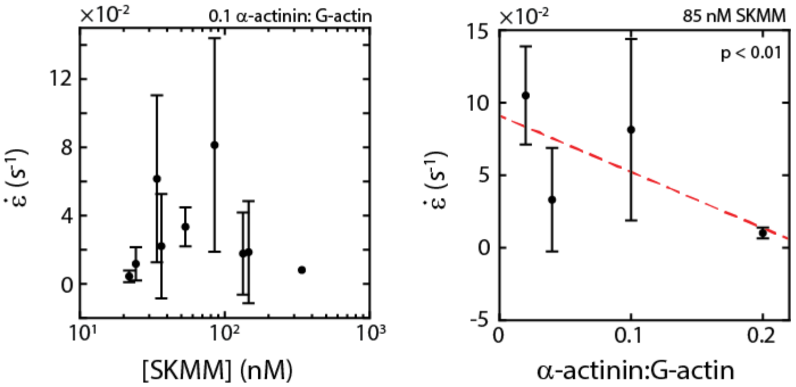

Figure B.1: **Experimental non-monotonicity of actomyosin networks** (left) Reconstituted *in vitro* experiments consisting of skeletal muscle myosin (SkMM), F-actin, and the cross-linker α-actinin, shows a non-monotonic behavior of strain rate with increasing SkMM concentration. α-actinin is known to exhibit catch-bond behavior [2, 3]. (right) Increasing the concentration of α-actinin at a fixed concentration of SkMM decreases the network strain rate. Experimental detail can be found in published works [4, 5, 6].

modeled as a load-dependent velocity along the actin filament over the time step.

B.2 Strain calculations

The deformation of the network was quantified by calculating the strain (t) of the actin network [137]. To do this, the system was first coarse grained into 5×5 μm^2 windows. Akin to particle image velocimetry, the change in positions of the center of mass for the filaments within each coarsegrained window across a time interval $\Delta t = 5$ s was calculated. As such, the instantaneous displacement field at position $\mathbf{r}$ and time t were calculated, weighted by the local density of actin monomers, $\mathbf{x}_0(\mathbf{r}, t)$, which is then interpolated onto a 1.25×1.25 μm^2 grid. The instantaneous displacement field is related to the velocity field by the timescale Δt.

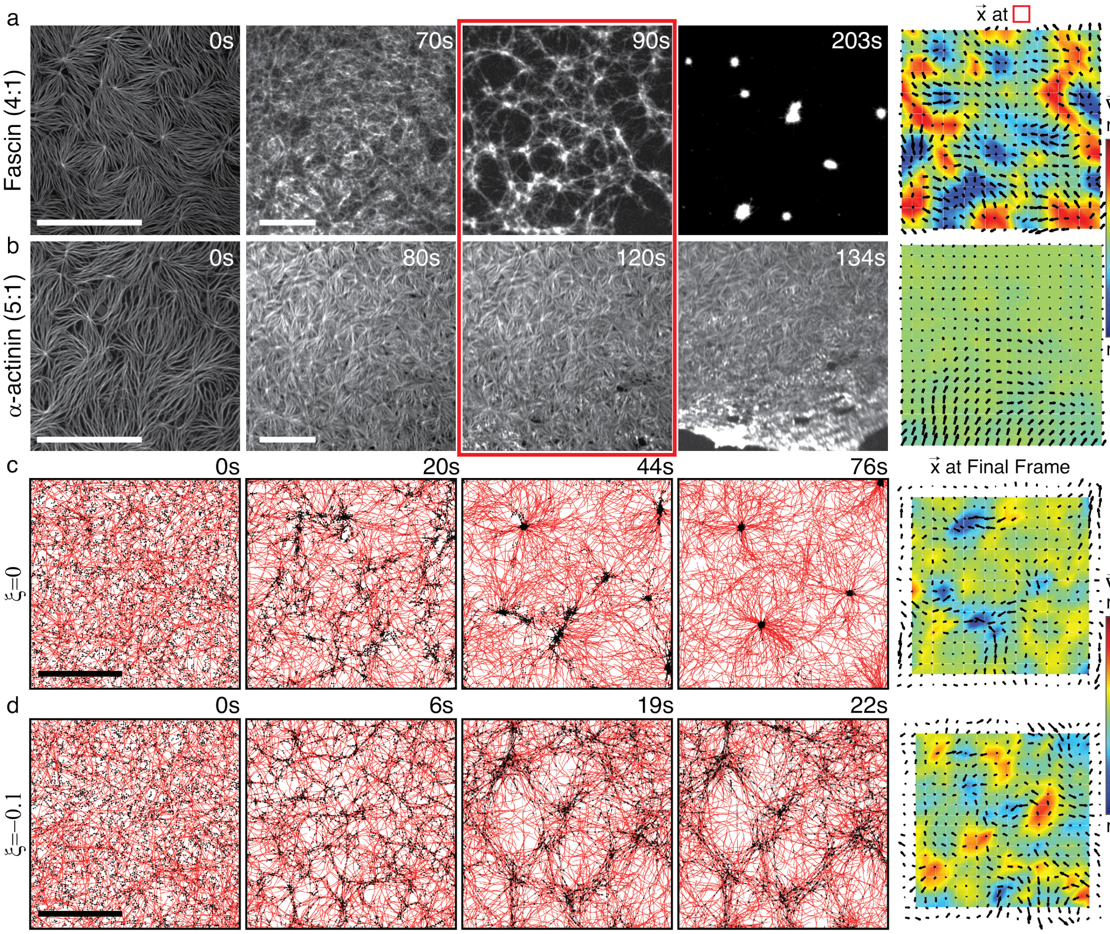

Figure B.2: **Simulations and experiments give similar dynamics** (a) Montage of dynamics seen in reconstituted *in vitro* actomyosin experiment containin skeletal muscle myosin, actin, and the slip bond cross-linker fascin [7]. There is a $4:1$ ratio between G-actin and fascin, showing the system evolving to asters. Right shows the cumulative displacement field (arrows) and strain (colors) at the time point indicated by the red rectangle. (b) Similar to (a), but with the catch bond cross-linker α-actinin in the place of fascin, showing the system leading to an arrested state until there is a large-scale network rupture seen in the final panel. (c) Typical simulation containing ideal motors ($\xi = 0$ μm) showing the formation of asters, similar to the experiments containing fascin. (d) Typical simulation containing motors with high catch-strength ($\xi = -0.1$ μm) showing an arrested state, similar to the experiment containing α-actinin.

The cumulative displacement field is calculated as

$$\mathbf{x}(\mathbf{r},t) = \int_0^t \mathrm{d}\tau \, \mathbf{x}_0(\mathbf{r},\tau). \tag{B.1}$$

The strain is calculated as the spatial average of the divergence of the cumulative displacement field at every time point, $\varepsilon(t) = \langle \boldsymbol{\nabla} \cdot \mathbf{x} \rangle$. Contraction is defined as transitioning from $\varepsilon \approx 0$ to a maximum $\varepsilon_{\mathrm{max}}$. The rate of contraction, or average strain rate $\dot{\varepsilon}$, was defined as the slope of a line fit to $\varepsilon(t)$ from 25% to 75% of $\varepsilon_{\mathrm{max}}$

B.3 Energy Density Calculation

The potential energies for filament stretching, $U_{\mathrm{f}}^{\mathrm{stretch}}$, filament bending, $U_{\mathrm{f}}^{\mathrm{bend}}$, and motor stretching, $U_{\mathrm{motor}}^{\mathrm{stretch}}$ were calculated at each time point. The energy density ω of a network in a box of area L^2 is defined as $\omega = \sum_i U_i / L^2$.

B.4 Calculating irreversibility

Considering a trajectory of length t broken in N steps indexed by $j \in [1, N]$, for each state m', there exists a probability per unit time of transitioning to a state m at the next time step via a mechanism μ, denoted by $W^{\mu_j}_{m_{j+1}m'_j}$. The irreversibility is [31]

$$\lambda(t) = \sum_{j=1}^{N} \ln \frac{W^{\mu_j}_{m_{j+1}m'_j}}{W^{\mu_{j+1}}_{m_{j+2}m'_j}}. \tag{B.2}$$

The denominator in the natural logarithm is the probability per unit time of making the reverse transition at the next time step, hence measures how likely a transition is to reverse itself and is equal to zero when the forward and backward transitions are equal to each other. The only mechanisms for which irreversibility was calculated were binding and unbinding.

Appendix C

Appendix for Chapter 4

C.1 Analytic $\dot{S}$ of coupled Gaussian fields

Consider the coupled equations of motion for the scalar fields ϕ and ψ in $d+1$ dimensions.

$$\partial_t \phi(\mathbf{x}, t) = -D(r - \nabla^2)\phi - \alpha\psi + \sqrt{2D}\xi_\phi \tag{C.1}$$

$$\partial_t \psi(\mathbf{x}, t) = -D(r - \nabla^2)\psi + \alpha\phi + \sqrt{2D}\xi_\psi. \tag{C.2}$$

with $\langle \xi^i(\mathbf{x}, t)\xi^j(\mathbf{x}', t')\rangle = \delta^{ij}\delta(t - t')\delta^d(\mathbf{x} - \mathbf{x}')$. This is a Gaussian model with free energy

$$F = \int d^d x \, \left[\frac{r}{2}\left(\phi^2 + \psi^2\right) + \frac{1}{2}\left(|\boldsymbol{\nabla}\phi|^2 + |\boldsymbol{\nabla}\psi|^2\right) \right]. \tag{C.3}$$

The interaction term cannot be written as a gradient of an energy, so we have

$$\partial_t \phi(\mathbf{x}, t) = -D\frac{\delta F}{\delta \phi} - \alpha\psi + \sqrt{2D}\xi_\phi \tag{C.4}$$

$$\partial_t \psi(\mathbf{x}, t) = -D\frac{\delta F}{\delta \psi} + \alpha\phi + \sqrt{2D}\xi_\psi. \tag{C.5}$$

Combining the two fields into a single vector, $\boldsymbol{\eta}(\mathbf{x}, t) = (\phi(\mathbf{x}, t), \psi(\mathbf{x}, t))^T$, we write:

$$\partial_t \boldsymbol{\eta} = B\boldsymbol{\eta} + \sqrt{2D}\boldsymbol{\xi}; \qquad B(\mathbf{x}) = \begin{pmatrix} -D(r - \nabla^2) & -\alpha \\ \alpha & -D(r - \nabla^2) \end{pmatrix}. \tag{C.6}$$

To get the cross-spectral density, we rewrite Equation C.6 as an Ito stochastic differential equation:

$$d\boldsymbol{\eta} = B\boldsymbol{\eta}\, dt + \Xi\, d\mathbf{W}, \tag{C.7}$$

where $\mathbf{W}(\mathbf{x}, t)$ is a multidimensional Wiener process in space and time with strength $\Xi^{ij} = \sqrt{2D}\delta^{ij}$. The eigenvalues of A have negative real parts, so a stationary solution exists. The cross-spectral density is [29]

$$C(\mathbf{q}, \omega) = \left(B(\mathbf{q}) - i\omega\mathbb{I}\right)^{-1} \Xi\Xi^T \left(B(\mathbf{q}) + i\omega\mathbb{I}\right)^{-T}. \tag{C.8}$$

Noting $\boldsymbol{\Xi}\ \boldsymbol{\Xi}^T = 2D\mathbb{I}$, we have

$$C(\omega) = \frac{2D}{|\left(D(r + q^2) + i\omega\right)^2 + \alpha^2)|^2} \begin{pmatrix} \left[D(r + q^2)\right]^2 + \alpha^2 + \omega^2 & i2\alpha\omega \\ -i2\alpha\omega & \left[D(r + q^2)\right]^2 + \alpha^2 + \omega^2 \end{pmatrix}. \tag{C.9}$$

The inverse is given by

$$C^{-1}(\omega) = \frac{1}{2D} \begin{pmatrix} \left[D(r + q^2)\right]^2 + \alpha^2 + \omega^2 & -i2\alpha\omega \\ i2\alpha\omega & \left[D(r + q^2)\right]^2 + \alpha^2 + \omega^2 \end{pmatrix}. \tag{C.10}$$

Finally, using Equation 4.4, we have

$$\dot{S} = V \iint_{-\infty}^{\infty} \frac{d\omega}{2\pi} \frac{d\mathbf{q}}{2\pi} \frac{8\alpha^2\omega^2}{|(D(r + q^2) + i\omega)^2 + \alpha^2)|^2} = V \frac{\alpha^2}{D\sqrt{r}}. \tag{C.11}$$

Rearranging the denominator of the integrand of above gives $\mathcal{E}^{DGF}$ given in the main text.

We can alternatively calculate the entropy production rate by using the Onsager-Machlup functional [39] for the path probability functional $P[\boldsymbol{\eta}]$ in

$$\dot{S} = \lim_{T\to\infty} \frac{1}{T} \left\langle \ln \frac{P[\boldsymbol{\eta}]}{\widetilde{P}[\boldsymbol{\eta}]} \right\rangle \tag{C.12}$$

Writing it as a path $P[\boldsymbol{\eta}] \propto \exp(-\mathcal{A})$, where $\mathcal{A}$ is the action, this becomes

$$\dot{S} = \lim_{T\to\infty} \frac{1}{T} \left\langle \widetilde{\mathcal{A}} - \mathcal{A} \right\rangle, \tag{C.13}$$

where $\widetilde{\mathcal{A}}$ is the action under time-reversal. To calculate $\mathcal{A}$, we use standard path integral techniques, i.e. the Martin-Siggia-Rose formalism [245]. The idea is to try and find the expectation of some observable, O, over noise realizations.

$$\langle O[\boldsymbol{\eta}] \rangle_{\xi} = \int \mathcal{D}[\boldsymbol{\xi}]\ O[\boldsymbol{\eta}] P[\boldsymbol{\xi}]. \tag{C.14}$$

Since the noise is Gaussian, we have

$$P[\boldsymbol{\xi}] \propto \exp\left(\frac{1}{4D} \int d^d x\ dt\ \boldsymbol{\xi}^2 \right) \tag{C.15}$$

(we use Einstein notation throughout). We then insert the most complicated expression for 1 ever written. Using the integral representation of the functional delta function, $\delta[f(x)] = \int \mathcal{D}[i\widetilde{f}] \exp\Big[- \int dx \widetilde{f}(x) f(x) \Big]$, we write

$$\begin{aligned} 1 &= \int \prod_j \mathcal{D}[\eta^j] \delta(\partial_t \eta^j - B^j_k \eta^k - \xi^j) \qquad (C.16) \\ &= \int \prod_j \mathcal{D}[\eta^j] \mathcal{D}[i\widetilde{\eta}_j] \exp\Big\{ - \int d^d x\ dt \left[\widetilde{\eta}_j \left(\partial_t \eta^j - B^j_k \eta^k - \xi^j \right) \right] \Big\} \qquad (C.17) \end{aligned}$$

to get

$$\langle O[\boldsymbol{\eta}]\rangle_{\xi} = \int \mathcal{D}[\boldsymbol{\xi}] \prod_{j} \mathcal{D}[\eta^{j}]\mathcal{D}[i\widetilde{\eta}_{j}]\, O[\boldsymbol{\eta}] \exp\left[\frac{1}{4}\int d^{d}x\ dt\,\left(\xi^{i}\Xi^{-1}_{ij}\xi^{j} - 4\widetilde{\eta}_{j}\xi^{j}\right) - \widetilde{\eta}_{j}\left(\partial_{t}\eta^{j} - B^{j}_{k}\eta^{k}\right)\right]. \tag{C.18}$$

Completing the square in ξ and doing the Gaussian integrals, we get

$$\langle O[\boldsymbol{\eta}]\rangle_{\xi} = \int \prod_{j} \mathcal{D}[\eta^{j}]\mathcal{D}[i\widetilde{\eta}_{j}]\ O[\boldsymbol{\eta}] \times \exp\left\{-\int d^{d}x\ dt\,\left[\widetilde{\eta}_{j}\left(\partial_{t}\eta^{j} - B^{j}_{k}\eta^{k}\right) - \widetilde{\eta}_{j}\Xi^{jk}\widetilde{\eta}_{k}\right]\right\}. \tag{C.19}$$

Doing the integrals over the response fields $\widetilde{\eta}$, we are left with

$$\langle O[\boldsymbol{\eta}]\rangle_{\xi} = \int \prod_{j} \mathcal{D}[\eta^{j}]\ O[\boldsymbol{\eta}]\ \exp(-\mathcal{A}[\boldsymbol{\eta}]) \tag{C.20}$$

where $\mathcal{A}$ is the Onsager-Machlup functional

$$\mathcal{A} = -\frac{1}{4D}\int d^{d}x\ dt\ \left(\partial_{t}\eta^{j} - B^{j}_{k}\eta^{k}\right)^{2} \tag{C.21}$$

Noting that the only time asymmetric part of the action is $\partial_t \eta$, we can write

$$\mathcal{A} = -\frac{1}{4D}\int d^{d}x\ dt\ \left(\partial_{t}\phi + D\frac{\delta F}{\delta\phi} + \alpha\psi\right)^{2} + \left(\partial_{t}\psi + D\frac{\delta F}{\delta\psi} - \alpha\phi\right)^{2} \tag{C.22}$$

$$\widetilde{\mathcal{A}} = -\frac{1}{4D}\int d^{d}x\ dt\ \left(\partial_{t}\phi - D\frac{\delta F}{\delta\phi} - \alpha\psi\right)^{2} + \left(\partial_{t}\psi - D\frac{\delta F}{\delta\psi} + \alpha\phi\right)^{2} \tag{C.23}$$

Taking the difference $\widetilde{\mathcal{A}} - \mathcal{A}$, and noting that $(a+b)^2 - (a-b)^2 = 4ab$, we have

$$\widetilde{\mathcal{A}} - \mathcal{A} = -\frac{1}{D}\int d^{d}x dt\ \partial_{t}\phi\left(-D\frac{\delta F}{\delta\phi} - \alpha\psi\right) + \partial_{t}\psi\left(-D\frac{\delta F}{\delta\psi} + \alpha\phi\right) \tag{C.24}$$

In the Stratonovich convention, $dF/dt = \partial_t\phi\ (\delta F/\delta\phi) + \partial_t\psi\ (\delta F/\delta\psi)$, which will turn into a constant difference in free energies upon taking the time integral. This constant value will tend to zero as the limit $T \to \infty$ is taken. Further, there is a time-symmetric portion of the action that is being omitted due to the Jacobian factor in switching from an integral in $\boldsymbol{\xi}$ to $\boldsymbol{\eta}$ that also arises due to the Stratonovich discretization used throughout this article.

We find the entropy production rate to be

$$\dot{S} = \lim_{T\to\infty} \frac{\alpha}{DT} \int d^d x dt \ \left(\psi\dot{\phi} - \dot{\psi}\phi\right) \tag{C.25}$$

Plugging in the equations of motion, we find

$$\left\langle \dot{\psi}\phi \right\rangle = \left\langle -D\frac{\delta F}{\delta \psi}\phi - \alpha\phi^2 + \xi_\psi \phi \right\rangle = \left\langle -D\left[(r-\nabla^2)\psi\right]\phi - \alpha\phi^2 + \xi_\psi\phi \right\rangle \tag{C.26}$$

$$\left\langle \psi\dot{\phi} \right\rangle = \left\langle -D\frac{\delta F}{\delta \phi}\psi + \alpha\psi^2 + \xi_\phi \psi \right\rangle = \left\langle -D\left[(r-\nabla^2)\phi\right]\psi + \alpha\psi^2 + \xi_\phi\psi \right\rangle \tag{C.27}$$

Some care must be taken in evaluating the terms linear in the noise. If the Ito convention had been used, they would be trivially zero, but that is not the general case in the Stratonovich convention. However, as each field is multiplied by the opposite component of the noise, one can show that they indeed identically equal 0. Putting everything together, we have

$$-Dr\psi\phi + D(\nabla^2\psi)\phi + \alpha\phi^2 + Dr\phi\psi - D(\nabla^2\phi)\psi + \alpha\psi^2 \tag{C.28}$$

The two Laplacian terms will cancel under one integration by parts each, leaving us with

$$\dot{S} = \frac{\alpha^2}{D}\int d^d x \ \left\langle \phi^2 + \psi^2 \right\rangle \tag{C.29}$$

where we have replaced the time average with an ensemble average, assuming ergodicity. Assuming the system to be in the steady state, we integrate over the equal-time (i.e. $\omega = 0$) power spectrum of ϕ and ψ

$$\langle \phi(k)\phi(-k) \rangle = \int \frac{dk}{2\pi} \frac{1}{k^2 + r} = \frac{1}{2\sqrt{r}}. \tag{C.30}$$

Using this expression for both ϕ and ψ in the equation for $\dot{S}$ above, we have

$$\dot{S} = \frac{\alpha^2}{D\sqrt{r}} V, \tag{C.31}$$

where V is the total volume of the space, and $\dot{s} = \dot{S}/V$.

C.2 Gaussian approximation lower bounds $\dot{S}$

The KL divergence in Equation 4.1 is an exact expression for the entropy production rate provided that the observed set of variables, $\{x^\mu\}$, contains every non-equilibrium degree of freedom present in the system. In practice, one only has access to a subset of those degrees of freedom, making the measured KL divergence a lower bound on the entropy production rate. Here, we show that the Gaussian assumption for $P[\mathbf{X}]$ provides another lower bound on the irreversibility measured on the scale of the observed mesoscale trajectories.

The proof relies on the data processing inequality [44], which states that any transformation of variables $F : x^\mu \to y^\mu$ will lower the relative entropy between two distributions over both sets of variables,

$$D_{\text{KL}}\left(P\left[\{x^\mu\}\right] || Q\left[\{x^\mu\}\right]\right) \geq D_{\text{KL}}\left(P\left[\{y^\mu\}\right] || Q\left[\{y^\mu\}\right]\right). \tag{C.32}$$

Intuitively, it states that any processing of an observation $\{x^\mu\}$ makes it more difficult to determine whether it came from P or Q. Our strategy will be to choose a transformation that will turn any distribution over x^μ into a Gaussian distribution over y^μ. In our case, our observables are the frequency space variables $x^\mu(\mathbf{q},\omega)$, and the transformation is a multiplication of by a random phase field $\theta(\mathbf{q},\omega)$, i.e. $x^\mu(\mathbf{q},\omega) \to x^\mu(\mathbf{q},\omega)e^{i\theta(\mathbf{q},\omega)}$. This random phase, when integrated over frequency space, will make all correlations zero except for the two-point correlation function due to the fact that the variables in real space are real, making the two-point correlation equal to $\langle x^\mu(x^\mu)^*\rangle$, cancelling the random phase. Thus, the transformed variables are described by a Gaussian distribution (defined as the distribution whose only non-zero cumulants are the first and second), and the data processing inequality guarantees that this provides a lower bound to the KL divergence over the original distributions.

C.3 True and blind entropy production

We calculate the true $\dot{S}$ of any specific trajectory $\mathbf{z} = \{m_j | j = 1, \ldots, N\}$ as follows. For each state m', there exists a probability per unit time of transitioning to a new state m via a chemical reaction μ, denoted by $W^{(\mu)}_{m,m'}$. At steady state, the true entropy produced is [31]

$$\Delta S_{\text{true}}[\mathbf{z}] = \sum_{j=1}^{N} \ln \frac{W^{(\mu_j)}_{m_j,m_{j-1}}}{W^{(\mu_j)}_{m_{j-1},m_j}} \tag{C.33}$$

Note that ΔS_{true} is now itself a random variable that depends on the specific trajectory. We estimate $\left\langle \dot{S}_{\text{true}} \right\rangle$ by fitting a line to an ensemble average of ΔS_{true} (Supplementary Figure 3), and compare that to $\hat{\dot{S}}$. We calculate $\dot{S}_{\text{blind}}$ by considering the “rate” at which a transition can occur as the sum over all the rates that give rise to the observed transition in (X, Y), i.e.

$$\Delta S_{\text{blind}} = \sum_{j=1}^{N} \ln \frac{\sum\limits_{\{\mu_j | m_{j-1} \to m_j\}} W_{m_j, m_{j-1}}^{(\mu_j)}}{\sum\limits_{\{\mu_j | m_{j-1} \to m_j\}} W_{m_{j-1}, m_j}^{(\mu_j)}} \tag{C.34}$$

where $\sum_{\{\mu_j | m_{j-1} \to m_j\}}$ denotes a sum over all reaction pathways μ that give rise to the transition $m_{j-1} \to m_j$. This procedure coarse-grains ΔS_{true}, giving $\Delta S_{\text{blind}} \leq \Delta S_{\text{true}}$ [232]. ΔS_{blind} is the maximum entropy production that can be inferred by any method that observes trajectories in (X, Y), but which does not have access to the reaction pathways followed.

C.4 Bias in $\dot{S}$ and $\mathcal{E}$ estimators

We now turn to the problem of estimating the bias in our measured entropy production rate. For this, we assume that we have an equilibrium process and calculate what the average measured entropy production rate is, representing the systematic overestimation of our estimator. We work in coordinates where the covariance matrix is the identity, $C^{\mu\nu} = \delta^{\mu\nu}$. Due to a combination of measurement errors and only having a finite time series, we will measure a matrix that deviates from the identity by

$$\widetilde{C}^{\mu\nu} = \delta^{\mu\nu} + \widetilde{R}^{\mu\nu} + i\widetilde{A}^{\mu\nu}, \tag{C.35}$$

where $\widetilde{R}^{\mu\nu}(\omega)$ and $\widetilde{A}^{\mu\nu}(\omega)$ are elements of a symmetric and anti-symmetric $D \times D$ matrix, respectively, each assumed to be much smaller than 1. The anti-symmetric contribution must be purely imaginary because $\widetilde{C}^{\mu\nu}$ is a Hermitian matrix by definition. Further, we have $R^{\mu\nu}(-\omega) = R^{\mu\nu}(\omega)$ and $A^{\mu\nu}(-\omega) = -A^{\mu\nu}(\omega)$. For notational simplicity, we define $\widetilde{M}^{\mu\nu} \equiv \delta^{\mu\nu} + \widetilde{R}^{\mu\nu}$ and therefore $\hat{\mathbf{C}} = \hat{\mathbf{M}} + i\hat{\mathbf{A}}$.

To calculate the EPR, we need to calculate the EPF, $\mathcal{E} = \mathrm{Tr}\{\mathbf{C}(\omega)\,[\mathbf{C}^{-1}(-\omega) - \mathbf{C}^{-1}(\omega)]\}$.

We approximate $\hat{\mathbf{C}}^{-1}$ as

$$\hat{\mathbf{C}}^{-1} = (\hat{\mathbf{M}} + i\hat{\mathbf{A}})^{-1} \approx \hat{\mathbf{M}}^{-1} - i\hat{\mathbf{M}}^{-1}\hat{\mathbf{A}}\hat{\mathbf{M}}^{-1}. \tag{C.36}$$

Then, $\mathbf{C}^{-1}(-\omega) - \mathbf{C}^{-1}(\omega) = 2i\hat{\mathbf{M}}^{-1}\hat{\mathbf{A}}\hat{\mathbf{M}}^{-1}$. Multiplying by $\hat{\mathbf{C}}$,

$$\mathbf{C}(\omega)\left[\mathbf{C}^{-1}(-\omega) - \mathbf{C}^{-1}(\omega)\right]\} = 2i\hat{\mathbf{M}}^{-1}\hat{\mathbf{A}}\hat{\mathbf{M}}^{-1}\hat{\mathbf{M}} - 2\hat{\mathbf{M}}^{-1}\hat{\mathbf{A}}\hat{\mathbf{M}}^{-1}\hat{\mathbf{A}} \tag{C.37}$$

Taking the trace of Equation C.37, the first term is an asymmetric matrix with zero trace. By writing $\hat{\mathbf{M}} = \mathbb{I} + \hat{\mathbf{R}}$, we approximate $\hat{\mathbf{M}}^{-1} \approx \mathbb{I} - \hat{\mathbf{R}}$, and the second term is approximately as $\hat{\mathbf{A}}^2 + \mathcal{O}(\hat{\mathbf{A}}^2\hat{\mathbf{R}} + \hat{\mathbf{A}}\hat{\mathbf{R}}\hat{\mathbf{A}})$. Thus, to lowest order we have

$$\mathcal{E} = \mathrm{Tr}\{\mathbf{C}(\omega)\left[\mathbf{C}^{-1}(-\omega) - \mathbf{C}^{-1}(\omega)\right]\} \approx -\mathrm{Tr}\left(\hat{\mathbf{A}}^2\right) = 2\sum_{\mu>\nu}(\hat{A}^{\mu\nu})^2. \tag{C.38}$$

Assuming each element of $\mathbf{A}$ is an indepenent and identically distributed random variable, we can write the average EPF measured at equilibrium as

$$\langle\mathcal{E}\rangle_{\mathrm{eq}} = 2\frac{M(M-1)}{2}\left\langle(\hat{A}^{\mu\nu})^2\right\rangle = \frac{M(M-1)}{2}. \tag{C.39}$$

We calculated $\left\langle(\widetilde{A}^{\mu\nu})^2\right\rangle$ as follows:

$$\begin{aligned}
\left\langle(\widetilde{A}^{\mu\nu})^2\right\rangle &= \left\langle[\mathrm{Im}(x^\mu x^{\nu *})]^2\right\rangle && \text{(C.40)}\\
&= \left\langle[\mathrm{Re}(x^\mu)\mathrm{Im}(x^{\nu *}) + \mathrm{Im}(x^\mu)\mathrm{Re}(x^{\nu *})]^2\right\rangle && \text{(C.41)}\\
&= \left\langle[\mathrm{Re}(x^\mu)\mathrm{Im}(x^{\nu *})]^2 + [\mathrm{Im}(x^\mu)\mathrm{Re}(x^{\nu *})]^2 + \text{cross-terms}\right\rangle && \text{(C.42)}\\
&= \frac{1}{2} && \text{(C.43)}
\end{aligned}$$

The cross-terms average to zero because, in our choice of coordinate system, $|x^\mu|^2 = 1$, so the real and imaginary parts of x^μ are equally distributed along the unit circle.

In addition, x^μ and x^ν should be uncorrelated (recall that we are working at equilibrium). The first and second term each have both a real and an imaginary part squared, each of which is always positive and on average equal to $\frac{1}{2}$. Thus, each term is $\frac{1}{4}$ and adds to $\frac{1}{2}$.

To estimate $\hat{\dot{S}}$, we smooth $\widetilde{\mathcal{E}}$ and integrate over all frequencies. We calculate $\left\langle(\hat{A}^{\mu\nu})^2\right\rangle$ as

$$(\hat{A}^{\mu\nu})^2 = \left(\sum_{\omega_i} \Delta\omega \frac{\exp\left[-\dfrac{(\omega_i-\omega_n)^2}{2\sigma^2}\right]}{\sqrt{2\pi\sigma^2}} \widetilde{A}^{\mu\nu}(\omega_i)\right)^2 \tag{C.44}$$

$$\begin{aligned}
\left\langle(\hat{A}^{\mu\nu})^2\right\rangle &= \sum_{\omega_i} (\Delta\omega)^2 \frac{\exp\left[-\dfrac{(\omega_i-\omega_n)^2}{\sigma^2}\right]}{2\pi\sigma^2} \left\langle(\hat{A}^{\mu\nu})^2(\omega_i)\right\rangle && \text{(C.45)}\\
&\approx \frac{\Delta\omega}{4\pi\sigma^2}\int d\omega \exp\left[-\omega^2/\sigma^2\right] = \frac{\Delta\omega}{4\pi\sigma^2}\sqrt{\pi\sigma^2} && \text{(C.46)}\\
&= \frac{\sqrt{\pi}}{2T\sigma}. && \text{(C.47)}
\end{aligned}$$

We used $\left\langle\widetilde{A}^{\mu\nu}(\omega_i)\widetilde{A}^{\mu\nu}(\omega_j)\right\rangle = \left\langle(\widetilde{A}^{\mu\nu})^2(\omega_i)\right\rangle \delta_{ij}$ in the second line, passed to an integral using one of the integration measures $\Delta\omega$ in the third line, and substituted $\Delta\omega = 2\pi(T)^{-1}$ in the fourth line. Finally, we arrive at

$$\dot{S}_{\text{eq}} = 2\frac{M(M-1)}{2}\int\limits_{-\omega^{\max}}^{\omega^{\max}} \frac{d\omega}{2\pi}\left\langle(\hat{A}^{\mu\nu})^2\right\rangle = \frac{M(M-1)}{2}\frac{\omega^{\max}}{T\sigma\sqrt{\pi}} \tag{C.48}$$

If we also average the covariance functions over N independent trajectories with the same dynamics, this bias is further reduced, leaving us with our final estimate of the bias in our entropy production rate estimator

$$\dot{S}_{\text{eq}} = \frac{1}{N}\frac{M(M-1)}{2}\frac{\omega^{\max}/\sigma}{T\sqrt{\pi}} \tag{C.49}$$

Following the same line of reasoning for a set of M fields in $d+1$ dimensions, a similar expression can be derived. We again write $C^{\mu\nu}(\mathbf{q},\omega) = \mathbb{I} + R^{\mu\nu}(\mathbf{q},\omega) + iA^{\mu\nu}(\mathbf{q},\omega)$. Extra care must be taken in the field case because Equation 4.4 does not have the same symmetries as Equation 4.3. Specifically, while $R^{\mu\nu}(-\mathbf{q},-\omega) = R^{\mu\nu}(\mathbf{q},\omega)$ and $A^{\mu\nu}(-\mathbf{q},-\omega) = -A^{\mu\nu}(-\mathbf{q},-\omega)$, nothing can be said *a priori* about $R(\mathbf{q},-\omega)$ or $A(\mathbf{q},-\omega)$.

In order to calculate the bias, we will calculate the mean of the spatiotemporal entropy production factor, $\mathcal{E} = \mathrm{Tr}\{[\mathbf{C}^{-1}(\mathbf{q},-\omega) - \mathbf{C}^{-1}(\mathbf{q},\omega)]\,\mathbf{C}(\mathbf{q},\omega)\}$. The calculation is tedious, so we only report the result here:

$$\begin{aligned}
\langle\mathcal{E}\rangle_{\mathrm{eq}} &= \left\langle \mathrm{Tr}\left[\mathbf{R}^2 - \mathbf{A}^2\right]\right\rangle && \text{(C.50)}\\
&= M(M-1)\left(\left\langle (R^{\mu\nu})^2\right\rangle + \left\langle (A^{\mu\nu})^2\right\rangle\right) + M\left\langle (R^{\mu\mu})^2\right\rangle && \text{(C.51)}\\
&= M(M-1) + \frac{3M}{4} && \text{(C.52)}
\end{aligned}$$

We arrived at this by using the fact that $\mathrm{Tr}\,(\mathbf{A}^2) = \sum_{\mu\neq\nu}(A^{\mu\nu})^2$ and $\mathrm{Tr}\,(\mathbf{R}^2) = \sum_{\mu}(R^{\mu\mu})^2 + \sum_{\mu\neq\nu}(R^{\mu\nu})^2$ for an asymmetric and symmetric matrix, respectively, in addition to the assumption that every matrix element is an independent and identically distributed random variable. As before, $\langle (A^{\mu\nu})^2\rangle = 1/2 = \langle (R^{\mu\nu})^2\rangle$. Now turning to the diagonal elements of $\mathbf{R}$,

$$\begin{aligned}
\left\langle (R^{\mu\mu})^2\right\rangle &= \left\langle [1 - \mathrm{Re}\,(\phi^{\mu}\phi^{\mu *})]^2\right\rangle && \text{(C.53)}\\
&= 1 + \left\langle \mathrm{Re}\,(\phi^{\mu})^2\,\mathrm{Im}\,(\phi^{\mu})^2\right\rangle + \left\langle \mathrm{Re}\,(\phi^{\mu})^4\right\rangle + \left\langle \mathrm{Im}\,(\phi^{\mu})^4\right\rangle - 2\left\langle \mathrm{Re}\,(\phi^{\mu})^2 + \mathrm{Im}\,(\phi^{\mu})^2\right\rangle && \text{(C.54)}\\
&= \frac{3}{4}, && \text{(C.55)}
\end{aligned}$$

where we used $\langle x^4\rangle = 3\left\langle x^2\right\rangle^2$ for Gaussian variables and $\left\langle \mathrm{Re}\,(\phi^{\mu})^2\right\rangle = \left\langle \mathrm{Im}\,(\phi^{\mu})^2\right\rangle = 1/2$ in our choice of coordinate system.

Assuming the signals to have a total length in time of T and a total length in each spatial dimension of L_i, we smooth the spatiotemporal covariance function with a multivariate Gaussian of width σ_ω in the temporal dimension, and σ_{k_i} in each of the spatial dimensions, giving a factor of $\omega^{\max}\left(\sigma_\omega T\sqrt{\pi}\right)^{-1}$ for the temporal dimension and $q_i^{\max}\left(\sigma_{q_i} L_i\sqrt{\pi}\right)^{-1}$ for each spatial dimension. Putting all these results together, we have

$$\dot{s}_{\mathrm{eq}} = \frac{1}{N}\left(\frac{M(M-1)}{2} + \frac{3M}{8}\right)\frac{\omega^{\max}}{T\sigma_\omega\sqrt{\pi}}\prod_{i=1}^{d}\frac{q_i^{\max}}{L_i\sigma_{q_i}\sqrt{\pi}} \tag{C.56}$$

C.5 Macroscopic Brusselator

The reversible Brusselator model we consider in this paper is defined by

$$A \underset{k_1^-}{\overset{k_1^+}{\rightleftharpoons}} X; \quad B + X \underset{k_2^-}{\overset{k_2^+}{\rightleftharpoons}} Y + C; \quad 2X + Y \underset{k_3^-}{\overset{k_3^+}{\rightleftharpoons}} 3X, \tag{C.57}$$

where A, B, C are fixed external chemicals and the system is assumed to occur in a well-mixed vessel of volume V. Using mass action kinetics and writing lower-case letters as concentrations (e.g. $x \equiv X/V$), the macroscopic dynamics of the Brusselator are given by the coupled ODEs

$$\begin{aligned}\dot{x} &= k_1^+ a - k_1^- x - k_2^+ bx + k_2^- cy + k_3^+ x^2 y - k_3^- x^3 \\ \dot{y} &= k_2^+ bx - k_2^- cy - k_3^+ x^2 y + k_3^- x^3\end{aligned} \tag{C.58}$$

Detailed balance holds when each reaction rate in Equation C.57 is balanced, leading to the following equilibrium concentrations

$$X_{eq} = A\frac{k_1^+}{k_1^-} \tag{C.59}$$

$$Y_{eq} = X_{eq}\frac{Bk_2^+}{Ck_2^-} = X_{eq}\frac{k_3^-}{k_3^+}, \tag{C.60}$$

where the first and second equation for y_{eq} come from the k_2 and k_3 reactions, respectively. Using the two equations for y_{eq} gives us the condition for detailed balance given in the main text, $Bk_2^+k_3^+ = Ck_2^-k_3^-$.

The steady state values of (x, y) are given by setting the deterministic equations to 0, giving

$$x_{ss} = a\frac{k_1^+}{k_1^-} \tag{C.61}$$

$$y_{ss} = \frac{k_2^+ b x_{ss} + k_3^- x_{ss}^3}{k_2^- c + k_3^+ x_{ss}^2} \tag{C.62}$$

The relaxation matrix, R, that defines the stability of the steady state is given by expanding the deterministic equations to first order around their steady state values

$$R = \begin{pmatrix} \partial_x \dot{x} & \partial_y \dot{x} \\ \partial_x \dot{y} & \partial_y \dot{y} \end{pmatrix}\Bigg|_{ss} = \begin{pmatrix} -(k_1^- + bk_2^+) + 2k_3^+ x_{ss} y_{ss} - 3k_3^- x_{ss}^2 & k_2^- c + k_3^+ x_{ss}^2 \\ bk_2^+ - 2k_3^+ x_{ss} y_{ss} + 3k_3^- x_{ss}^2 & -(k_2^- c + k_3^+ x_{ss}^2) \end{pmatrix}. \tag{C.63}$$

The eigenvalues of R are given by solving its characteristic equation, giving

$$\lambda_\pm = \frac{\mathrm{Tr}(R)}{2} \pm \left[\left(\frac{\mathrm{Tr}(R)}{2}\right)^2 - \det(R)\right]^{1/2} \tag{C.64}$$

C.6 Numerical Methods

C.6.1 Driven Gaussian Field

We used a first-order Euler-Maruyama method to simulate Equation 4.5. In short, for a Langevin equation given by

$$\frac{\partial x(t)}{\partial t} = F(x(t)) + \sqrt{2D}\xi, \tag{C.65}$$

we can discretize the dynamics in time and integrate forward using

$$x(t_{j+1}) = x(t_j) + \Delta t \left(F(x(t_j) + \sqrt{\frac{2D}{\Delta t}} \right). \tag{C.66}$$

The important detail here is that the random force moves forward with a weight $\sqrt{\Delta t}$. This ensures that the mean-square displacement when $F = 0$ obeys Equation 1.19.

C.6.2 Gillespie algorithm

Simulations of the Brusselator, both the well-mixed version of Equation 4.14 and the reaction-diffusion version of Equation 4.16, are run using the Gillespie algorithm [8]. The basic premise is to consider a volume of well-mixed molecules that interact with each other via various mechanisms when they come into contact. By assuming a Maxwell-Boltzmann distribution for the velocities, one can write the distribution of time τ before a reaction μ occurs. We define c_μ as the probability that reaction μ occurs given a collision, and h_μ as a combinatorial factor reflecting the number of available particles for reaction μ. The algorithm at each time step is as follows:

1. Input desired values for M reactions, $c_1, \ldots, c_M$ and the initial molecular population numbers, $X_1, \ldots, X_N$. c_μ is related to the reaction rates and type of the reaction
2. Calculate the affinity $a_\mu = h_\mu c_\mu$ for current population sizes
3. Generate two random numbers, r_1, r_2, each distributed uniformly over $(0, 1)$.
    (a) Use r_1 to calculate the time of the next reaction step,

$$\tau = \frac{-\ln(r_1)}{\sum_{\nu=1}^{M} a_\nu},$$

(b) Normalize all the affinities as $\widetilde{a}_\mu = a_\mu / \sum_\mu a_\mu$. Use r_2 to choose which reaction happens by finding the μ that satisfies

$$\sum_{\nu=1}^{\mu-1} \widetilde{a}_\nu < r_2 \leq \sum_{\nu=1}^{\mu} \widetilde{a}_\nu$$

4. Change $t \to t+\tau$, and change number of chemical species according to whatever reaction just happened

For the Brusselator, our system of equations are given by Equation 4.14. There are $N = 2$ chemical species of interest (X and Y, A, B, C are assumed to remain constant), and $M = 6$ chemical pathways (the forward and reverse paths given by the chemical reaction scheme given above). The probabilities c_μ are

$$\begin{aligned} c_1^\pm = k_1^\pm; \quad c_2^\pm = k_2^\pm/V; \\ c_3^+ = \frac{2!}{V^2} k_3^+; \quad c_3^- = \frac{3!}{V^2} k_3^- \end{aligned} \tag{C.67}$$

and the combinatorial factors are

$$\begin{aligned} h_1^+ = A, \quad h_1^- = X \\ h_2^+ = BX, \quad h_2^- = DY \\ h_3^+ = Y\frac{X(X-1)}{2!}, \quad h_3^- = \frac{X(X-1)(X-2)}{3!} \end{aligned} \tag{C.68}$$

Simulation Parameters

name	**value**	**units**	**description**
N_{sim}	10	1	number of simulations per parameter set
dt	0.0001	τ	simulation time step
t_{final}	50	τ	total simulation time
dx	0.1	λ	spacing between lattice sites
N_{sites}	128	1	number of lattice sites
α	$[0, 1, \ldots, 25]$	τ^{-1}	driving frequency
σ_ω	1.57	τ^{-1}	width of smoothing Gaussian in time
σ_k	1.47	λ^{-1}	width of smoothing Gaussian in space

Table C.1: **Gaussian field simulation parameters.** Simulations of the Gaussian fields use an Euler-Maruyama algorithm to integrate the equations of motion. Time and space are scaled by $\tau = (Dr)^{-1}$ and $\lambda = r^{-1/2}$. The simulation is performed on a periodic, 1-dimensional lattice.

name	**value**	**units**	**description**
N_{sim}	50	1	number of simulations per parameter set
t_{final}	5000	τ	total time of simulation
k_1^+	1	τ^{-1}	forward reaction rate for reaction 1
k_1^-	0.5	τ^{-1}	reverse reaction rate for reaction 1
k_2^+	2	τ^{-1}	forward reaction rate for reaction 2
k_2^-	0.5	τ^{-1}	reverse reaction rate for reaction 2
k_3^+	2	τ^{-1}	forward reaction rate for reaction 3
k_3^-	0.5	τ^{-1}	reverse reaction rate for reaction 3
A	100	1	number of chemical species in reaction volume
V	100	1	reaction volume

Table C.2: **Brusselator simulation parameters.** Simulations of the Brusselator are done using a Gillespie algorithm [8]. Time is non-dimensionalized by $\tau = \left(k_1^+\right)^{-1}$. The strength of external driving is given by $\Delta\mu = \log\left((bk_2^+k_3^+)(ck_2^-k_3^-)^{-1}\right)$, where b and c are the concentrations of B and C, respectively. Values of B and C are changed to give driving strengths $\Delta\mu \in [-2, 8]$ with step size 0.1, while keeping $\sqrt{(bk_2^+k_3^+)(ck_2^-k_3^-)} = 1$, with 1 an arbitrarily chosen constant. The EPR plot in Fig. 2c uses varying smoothing widths. When $\Delta\mu < 5$, $\sigma = 1.26$. When $\Delta\mu \in [5, 5.8]$, $\sigma = 0.063$. When $\Delta\mu > 5.8$, $\sigma = 0.031$. The EPF plot shown in Fig. 2b uses a smoothing width of $\sigma = 0.126$. Different system volumes are used in Fig. 3.

name	**value**	**units**	**description**
N_{sim}	10	1	number of simulations per parameter set
N_{c}	64	1	number of lattice sites
D_X	1	$\lambda^2\tau^{-1}$	diffusion constant of chemical species X
D_Y	0.1	$\lambda^2\tau^{-1}$	diffusion constant of chemical species Y
t_{final}	100	τ	total time of simulation
k_1^+	1	τ^{-1}	forward reaction rate for reaction 1
k_1^-	0.5	τ^{-1}	reverse reaction rate for reaction 1
k_2^+	2	τ^{-1}	forward reaction rate for reaction 2
k_2^-	0.5	τ^{-1}	reverse reaction rate for reaction 2
k_3^+	2	τ^{-1}	forward reaction rate for reaction 3
k_3^-	0.5	τ^{-1}	reverse reaction rate for reaction 3
A	100	1	number of chemical species in reaction volume
C	400	1	number of chemical species in reaction volume
V	100	1	reaction volume of each compartment

Table C.3: **Reaction-diffusion Brusselator simulation parameters.** To add diffusion to the Brusselator, we employ a compartment-based Gillespie algorithm. Time is non-dimensionalized by $\tau = \left(k_1^+\right)^{-1}$, and space is non-dimensionalized by using the distance between each compartment, $\lambda = h = 1$.

$\Delta\mu$	$(\sigma_\omega, \sigma_q)$
$\in [-1, -0.5]$	(7, 1)
$\in [-0.5, 0.5]$	(14, 2)
$\in [0.5, 1]$	(7, 1)
$\in [1, 5.65]$	(5, 0.5)
$= 5.7$	(3.5, 0.4)
$= 5.8$	(1.75, 0.3)
$= 5.9$	(0.7, 0.1)
$= 6.0$	(0.35, 0.05)
$= 6.1$	(0.14, 0.02)
≥ 6.2	(0.035, 0.005)

Table C.4: **Smoothing widths as a function of driving force.** This table gives the smoothing widths $(\sigma_\omega, \sigma_q)$ as a function of chemical driving force $\Delta\mu$ used in Figure 4c in the main text. Figure 5 in the main text uses a smoothing width of $(\sigma_\omega, \sigma_q) = (0.07, 0.1)$ for all $\Delta\mu$.

Bibliography

[1] Pablo Sartori, Veikko F. Geyer, Andre Scholich, Frank Jülicher, and Jonathon Howard. Dynamic curvature regulation accounts for the symmetric and asymmetric beats of Chlamydomonas flagella. *eLife*, 2016. xxi, 93, 94

[2] Jorge M. Ferrer, Hyungsuk Lee, Jiong Chen, Benjamin Pelz, Fumihiko Nakamura, Roger D. Kamm, and Matthew J. Lang. Measuring molecular rupture forces between single actin filaments and actin-binding proteins. *PNAS*, 105(27):9221–9226, jul 2008. xxii, 47, 97, 98

[3] T Luo, K Mohan, P A Iglesias, and D N Robinson. Molecular mechanisms of cellular mechanosensing. *Nature Materials*, 12(11):1064–1071, 2013. xxii, 97, 98

[4] Ian Linsmeier, Shiladitya Banerjee, Patrick W. Oakes, Wonyeong Jung, Taeyoon Kim, and Michael P. Murrell. Disordered actomyosin networks are sufficient to produce cooperative and telescopic contractility. *Nature Communications*, 7:12615, 8 2016. xxii, 23, 29, 34, 39, 42, 46, 54, 98

[5] Michael P. Murrell and Margaret L. Gardel. Actomyosin sliding is attenuated in contractile biomimetic cortices. *Molecular Biology of the Cell*, 25(12):1845–53, jun 2014. xxii, 31, 34, 49, 98

[6] Michael P. Murrell, Todd Thoresen, and Margaret L. Gardel. Reconstitution of contractile actomyosin arrays. *Methods in Enzymology*, 540:265–282, 2014. xxii, 29, 32, 49, 98

[7] R Ishikawa, T Sakamoto, T Ando, S Higashi-Fujime, and K Kohama. Polarized actin bundles formed by human fascin-1: their sliding and disassembly on myosin II and myosin V in vitro. *Journal of Neurochemistry*, 87(3):676–685, 2003. xxii, 97, 99

[8] Daniel T. Gillespie. Exact stochastic simulation of coupled chemical reactions. *Journal of Physical Chemistry*, 81(25):2340–2361, dec 1977. xxiii, 115, 117

[9] Gill Bejerano. Ultraconserved Elements in the Human Genome. *Science*, 304(5675):1321–1325, may 2004. 1

[10] Xianrui Cheng and James E. Ferrell. Spontaneous emergence of cell-like organization in Xenopus egg extracts. *Science*, 366(6465):631–637, nov 2019. 1

[11] Tania A. Baker and Stephen P. Bell. Polymerases and the Replisome: Machines within Machines. *Cell*, 92(3):295–305, feb 1998. 2

[12] Udo Seifert. Stochastic thermodynamics, fluctuation theorems and molecular machines. *Reports on Progress in Physics*, 75(12):126001, 12 2012. 2, 12, 35, 42, 63, 64, 91

[13] F.S. Gnesotto, F. Mura, Jannes Gladrow, and Chase P. Broedersz. Broken detailed balance and non-equilibrium dynamics in living systems: a review. *Reports on Progress in Physics*, 81(6):066601, 6 2018. 2

[14] Mehran Kardar. *Statistical Physics of Particles*. Cambridge University Press, Cambridge, 2007. 5

[15] L P Wheeler. *Josiah Willard Gibbs: The History of a Great Mind*. Ox Bow Press, 1998. 9

[16] C. E. Shannon. A Mathematical Theory of Communication. *Bell System Technical Journal*, 27(3):379–423, 1948. 10

[17] Lars Onsager. Reciprocal Relations in Irreversible Processes. II. *Physical Review*, 38(12):2265–2279, dec 1931. 11

[18] Lars Onsager. Reciprocal Relations in Irreversible Processes. I. *Physical Review*, 37(4):405–426, feb 1931. 11

[19] Satoshi Yukawa. A Quantum Analogue of the Jarzynski Equality. *Journal of the Physical Society of Japan*, 69(8):2367–2370, aug 2000. 12

[20] Jordan M Horowitz and Juan M R Parrondo. Entropy production along nonequilibrium quantum jump trajectories. *New Journal of Physics*, 15(8):085028, aug 2013. 12

[21] Massimiliano Esposito, Upendra Harbola, and Shaul Mukamel. Nonequilibrium fluctuations, fluctuation theorems, and counting statistics in quantum systems. *Reviews of Modern Physics*, 81:1665–1702, Dec 2009. 12

[22] Albert Einstein. Über die von der molekularkinetischen Theorie der Wärme geforderte Bewegung von in ruhenden Flüssigkeiten suspendierten Teilchen. *Annalen der Physik*, 322(8):549–560, 1905. 13

[23] E M Purcell. Life at low Reynolds number. *American Journal of Physics*, 45(1):3–11, 1977. 13

[24] J Perrin. Mouvement brownien et réalité moléculaire. *Ann. Chim. Phys.*, 18(8):5–114, 1909. 13

[25] Ronald Newburgh, Joseph Peidle, and Wolfgang Rueckner. Einstein, Perrin, and the reality of atoms: 1905 revisited. *American Journal of Physics*, 74(6):478–481, jun 2006. 14

[26] Carlo Cercignani. *Ludwig Boltzmann: The Man who Trusted Atoms.* Oxford scholarship online: Physics module. Oxford University Press, 1998. 14

[27] R Kubo. The fluctuation-dissipation theorem. *Reports on Progress in Physics*, 29(1):306, jan 1966. 14

[28] Paul Langevin. Sur la theorie du mouvement brownien. *C.R. Acad. Sci., (Paris)*, 146:530–533, 1908. 14

[29] Crispin W. Gardiner. *Stochastic Methods: A Handbook for the Natural and Social Sciences.* Springer Berlin, 4th edition, 2010. 15, 103

[30] Ken Sekimoto. Langevin Equation and Thermodynamics. *Progress of Theoretical Physics Supplement*, 130:17–27, jan 1998. 15

[31] Massimiliano Esposito and Christian Van den Broeck. Three Detailed Fluctuation Theorems. *Physical Review Lettters*, 104(9):090601, mar 2010. 17, 52, 73, 100, 108

[32] Udo Seifert. Entropy production along a stochastic trajectory and an integral fluctuation theorem. *Physical Review Letters*, 95(4):040602, 2005. 17, 18, 35

[33] Christopher Jarzynski. Nonequilibrium Equality for Free Energy Differences. *Physical Review Letters*, 78(14):2690–2693, 1997. 17

[34] Jan Liphardt, Sophie Dumont, Steven B Smith, Ignacio Tinoco, and Carlos Bustamante. Equilibrium Information from Nonequilibrium Measurements in an Experimental Test of Jarzynski's Equality. *Science*, 296(5574):1832–1835, 2002. 17

[35] S. Chandrasekhar. Stochastic Problems in Physics and Astronomy. *Reviews of Modern Physics*, 15(1):1–89, jan 1943. 18

[36] R.K.P. Zia and B. Schmittmann. Probability currents as principal characteristics in the statistical mechanics of non-equilibrium steady states. *Journal of Statistical Mechanics*, 2007. 19, 73

[37] Carson C Chow and Michael A Buice. Path Integral Methods for Stochastic Differential Equations. *The Journal of Mathematical Neuroscience*, 5(1):8, dec 2015. 19

[38] U. C. Täuber. Field-Theory Approaches to Nonequilibrium Dynamics. In *Ageing and the Glass Transition*, pages 295–348. Springer Berlin Heidelberg, nov 2005. 19

[39] Lars Onsager and S. Machlup. Fluctuations and Irreversible Processes. *Physical Review*, 91(6):1505–1512, 9 1953. 19, 63, 68, 104

[40] Gavin E. Crooks. Entropy production fluctuation theorem and the nonequilibrium work relation for free energy differences. *Physical Review E*, 60(3):2721–2726, sep 1999. 20, 52

[41] R. Kawai, J. M. R. Parrondo, and C. Van den Broeck. Dissipation: The phase-space perspective. *Physical Review Letters*, 98:080602, Feb 2007. 20, 64

[42] Édgar Roldán and Juan M. R. Parrondo. Estimating dissipation from single stationary trajectories. *Physical Review Letters*, 105:150607, Oct 2010. 20

[43] Édgar Roldán and Juan M R Parrondo. Entropy production and Kullback-Leibler divergence between stationary trajectories of discrete systems. *Phys. Rev. E*, 85(3):31129, mar 2012. 20

[44] T. M. Cover and Joy A. Thomas. *Elements of information theory.* Wiley-Interscience, 2006. 20, 82, 107

[45] Juan M. R. Parrondo, Jordan M. Horowitz, and Takahiro Sagawa. Thermodynamics of information. *Nature Physics*, 11(2):131–139, 2015. 20

[46] J. Schnakenberg. Network theory of microscopic and macroscopic behavior of master equation systems. *Reviews of Modern Physics*, 48(4):571–585, 10 1976. 21, 73

[47] Terrell L. Hill. *Free Energy Transduction and Biochemical Cycle Kinetics.* Springer New York, New York, NY, 1989. 21

[48] Hong Qian. Phosphorylation Energy Hypothesis: Open Chemical Systems and Their Biological Functions. *Annual Review of Physical Chemistry*, 58(1):113–142, 5 2007. 21

[49] A.F. Huxley and R. Niedergerke. Structural Changes in Muscle During Contraction: Interference Microscopy of Living Muscle Fibres. *Nature*, 173(4412):971–973, may 1954. 22, 29, 31, 42

[50] Robert G. Roeder and William J. Rutter. Multiple Forms of DNA-dependent RNA Polymerase in Eukaryotic Organisms. *Nature*, 224(5216):234–237, oct 1969. 22

[51] J.J. Hopfield. Kinetic proofreading: a new mechanism for reducing errors in biosynthetic processes requiring high specificity. *PNAS*, 71(10):4135–9, 1974. 22

[52] Rennolds S. Ostrom, Caroline Gregorian, and Paul A. Insel. Cellular Release of and Response to ATP as Key Determinants of the Set-Point of Signal Transduction Pathways. *Journal of Biological Chemistry*, 275(16):11735–11739, apr 2000. 22

[53] Rob Phillips and Ron Milo. A feeling for the numbers in biology. *Proceedings of the National Academy of Sciences*, 106(51):21465–21471, dec 2009. 22

[54] Jasmine A. Nirody, Itay Budin, and Padmini Rangamani. ATP synthase: Evolution, energetics, and membrane interactions. *Journal of General Physiology*, 152(11), nov 2020. 22

[55] Thomas D Pollard. The cytoskeleton, cellular motility and the reductionist agenda. *Nature*, 422(6933):741–745, apr 2003. 22, 23

[56] Luca Goitre, Eliana Trapani, Lorenza Trabalzini, and Saverio Francesco Retta. *The Ras Superfamily of Small GTPases: The Unlocked Secrets*, pages 1–18. Humana Press, Totowa, NJ, 2014. 22

[57] Peter Mitchell. Coupling of Phosphorylation to Electron and Hydrogen Transfer by a Chemi-Osmotic type of Mechanism. *Nature*, 191(4784):144–148, jul 1961. 22

[58] J Howard. *Mechanics of Motor Proteins and the Cytoskeleton*. Sinauer Associates, Publishers, 2001. 23

[59] Thomas D. Pollard and Gary G. Borisy. Cellular Motility Driven by Assembly and Disassembly of Actin Filaments. *Cell*, 112(4):453–465, feb 2003. 23, 26

[60] Michael P. Murrell, Patrick W. Oakes, Martin Lenz, and Margaret L. Gardel. Forcing cells into shape: the mechanics of actomyosin contractility. *Nature Reviews Molecular Cell Biology*, 16(8):486–498, jul 2015. 23, 46

[61] Laurent Blanchoin, Rajaa Boujemaa-Paterski, Cécile Sykes, and Julie Plastino. Actin dynamics, architecture, and mechanics in cell motility. *Physiological Reviews*, 94(1):235–263, jan 2014. 23, 26, 46

[62] Miguel Vicente-Manzanares, Xuefei Ma, Robert S Adelstein, and Alan Rick Horwitz. Non-muscle myosin II takes centre stage in cell adhesion and migration. *Nature Reviews Molecular Cell Biology*, 10(11):778–790, nov 2009. 23

[63] M. Cristina Marchetti, Jean-Francois Joanny, Sriram Ramaswamy, Tanniemola B. Liverpool, Jacques Prost, Madan Rao, and R. Aditi Simha. Hydrodynamics of soft active matter. *Reviews of Modern Physics*, 85:1143–1189, 7 2013. 23, 61, 63

[64] Jacques Prost, Frank Jülicher, and J-F. Joanny. Active gel physics. *Nature Physics*, 11(2):111–117, feb 2015. 23, 61

[65] S Banerjee, M L Gardel, and U S Schwarz. The Actin Cytoskeleton as an Active Adaptive Material. *Annual Review of Condensed Matter Physics, Vol 11, 2020*, 11:421–439, 2020. 23, 48, 61

[66] Frank Jülicher, Armand Ajdari, and Jacques Prost. Modeling molecular motors. *Reviews of Modern Physics*, 69(4):1269–1282, 1997. 23, 46

[67] Oliver Lieleg, Mireille M.A.E. Claessens, and Andreas R. Bausch. Structure and dynamics of cross-linked actin networks. *Soft Matter*, 6(2):218–225, jan 2010. 23, 29, 46

[68] Chase P. Broedersz and Fred C. MacKintosh. Modeling semiflexible polymer networks. *Reviews of Modern Physics*, 86(3):995–1036, jul 2014. 23, 56

[69] Pierre Ronceray, Chase P. Broedersz, and Martin Lenz. Fiber networks amplify active stress. *Proceedings of the National Academy of Sciences*, 113(11):2827–2832, mar 2016. 23

[70] Gijsje H. Koenderink, Zvonimir Dogic, Fumihiko Nakamura, Poul M. Bendix, Fred C. MacKintosh, John H. Hartwig, Thomas P. Stossel, and David A. Weitz. An active biopolymer network controlled by molecular motors. *PNAS*, 106(36):15192–7, sep 2009. 23

[71] Michael P. Murrell and Margaret L. Gardel. F-actin buckling coordinates contractility and severing in a biomimetic actomyosin cortex. *PNAS*, 109(51):20820–5, 2012. 23, 26, 31, 39, 49

[72] Nikta Fakhri, Alok D. Wessel, Charlotte Willms, Matteo Pasquali, Dieter R. Klopfenstein, Frederick C. MacKintosh, and Christoph F. Schmidt. High-resolution mapping of intracellular fluctuations using carbon nanotubes. *Science*, 344(6187):1031–1035, may 2014. 23, 24

[73] Daisuke Mizuno, Catherine Tardin, C. F. Schmidt, and Fred C. MacKintosh. Nonequilibrium Mechanics of Active Cytoskeletal Networks. *Science*, 315(5810), 2007. 24, 35, 46, 59

[74] P Martin, A J Hudspeth, and F. Julicher. Comparison of a hair bundle's spontaneous oscillations with its response to mechanical stimulation reveals the underlying active process. *PNAS*, 98(25):14380–14385, dec 2001. 24

[75] Leticia F Cugliandolo. The effective temperature. *Journal of Physics A: Mathematical and Theoretical*, 44(48):483001, dec 2011. 24

[76] Étienne Fodor, Cesare Nardini, Michael E. Cates, Julien Tailleur, Paolo Visco, and Frédéric Van Wijland. How Far from Equilibrium Is Active Matter? *Physical Review Letters*, 2016. 24, 63

[77] Jannes Gladrow, Nikta Fakhri, Fred C. MacKintosh, Christoph. F. Schmidt, and Chase P. Broedersz. Broken Detailed Balance of Filament Dynamics in Active Networks. *Physical Review Letters*, 116(24):248301, 2016. 24, 35

[78] Jannes Gladrow, Chase P. Broedersz, and Christoph F. Schmidt. Nonequilibrium dynamics of probe filaments in actin-myosin networks. *Physical Review E*, 96(2):022408, apr 2017. 24, 35

[79] Christopher Battle, Chase P. Broedersz, Nikta Fakhri, Veikko Geyer, Jonathon Howard, Christoph F. Schmidt, and Fred C. MacKintosh. Broken detailed balance at mesoscopic scales in active biological systems. *Science*, 351(6268):604–607, 4 2016. 24, 35, 73

[80] Martin Bergert, Stanley D Chandradoss, Ravi A Desai, and Ewa Paluch. Cell mechanics control rapid transitions between blebs and lamellipodia during migration. *PNAS*, 109(36):14434–14439, sep 2012. 24

[81] Sergei Sukharev and Frederick Sachs. Molecular force transduction by ion channels diversity and unifying principles. *Journal of Cell Science*, 125(13):3075–3083, jul 2012. 25

[82] Margaret L Gardel, Ian C Schneider, Yvonne Aratyn-Schaus, and Clare M Waterman. Mechanical Integration of Actin and Adhesion Dynamics in Cell Migration. *Annual Review of Cell and Developmental Biology*, 26(1):315–333, 2010. 25, 29

[83] Bin Guo and William H. Guilford. Mechanics of actomyosin bonds in different nucleotide states are tuned to muscle contraction. *PNAS*, 103(26):9844–9849, jun 2006. 25, 47, 49, 50

[84] Allen J. Ehrlicher, Ramaswamy Krishnan, Ming Guo, Cécile M. Bidan, David A. Weitz, and Martin R. Pollak. Alpha-actinin binding kinetics modulate cellular dynamics and force generation. *PNAS*, 112(21):6619–6624, may 2015. 25

[85] M. Dembo, D. C. Torney, K. Saxman, and D. Hammer. The reaction-limited kinetics of membrane-to-surface adhesion and detachment. *Proceedings of the Royal Society of London. Series B. Biological Sciences*, 234(1274):55–83, jun 1988. 25, 47

[86] W E Thomas, V Vogel, and E Sokurenko. Biophysics of catch bonds. *Annual Review of Biophysics*, 37:399–416, 2008. 25, 47, 48, 50, 97

[87] Adriano Mesquita Alencar, Mariana Sacrini Ayres Ferraz, Chan Young Park, Emil Millet, Xavier Trepat, Jeffrey J. Fredberg, and James P. Butler. Non-equilibrium cytoquake dynamics in cytoskeletal remodeling and stabilization. *Soft Matter*, 12(41):8506–8511, 2016. 25

[88] José Alvarado, Misha Sheinman, Abhinav Sharma, Fred C. Mackintosh, and Gijsje H. Koenderink. Molecular motors robustly drive active gels to a critically connected state. *Nature Physics*, 9(9):591–597, 2013. 25, 46, 54

[89] B L Mbanga, B V S Iyer, V V Yashin, and A C Balazs. Tuning the Mechanical Properties of Polymer-Grafted Nanoparticle Networks through the Use of Biomimetic Catch Bonds. *Macromolecules*, 49(4):1353–1361, 2016. 26, 48, 60

[90] K C Dansuk and S Keten. Tunable seat belt behavior in nanocomposite interfaces inspired from bacterial adhesion pili. *Soft Matter*, 14(9):1530–1539, 2018. 26, 48, 60

[91] Brannon R McCullough, Laurent Blanchoin, Jean-Louis Martiel, and Enrique M De La Cruz. Cofilin Increases the Bending Flexibility of Actin Filaments: Implications for Severing and Cell Mechanics. *Journal of Molecular Biology*, 381(3):550–558, 2008. 26

[92] Chuan-Hsiang Huang, Ming Tang, Changji Shi, Pablo A Iglesias, and Peter N Devreotes. An excitable signal integrator couples to an idling cytoskeletal oscillator to drive cell migration. *Nature Cell Biology*, 15(11):1307–1316, nov 2013. 27

[93] M. C. Cross and P. C. Hohenberg. Pattern formation outside of equilibrium. *Reviews of Modern Physics*, 65(3):851–1112, 7 1993. 27, 62, 63

[94] Alan M. Turing. The chemical basis of morphogenesis. *Phil. Trans. R. Soc. Lond. B*, 237:37–72, 1952. 27, 63, 79

[95] Steven H. Strogatz. *Nonlinear dynamics and chaos*. CRC Press, 2015. 27, 68, 73

[96] J D Murray. *Mathematical Biology : I . An Introduction , Third Edition*. Springer, 2002. 27

[97] Gianmaria Falasco, Riccardo Rao, and Massimiliano Esposito. Information Thermodynamics of Turing Patterns. *Physical Review Letters*, 121(10):108301, 9 2018. 27, 63, 79

[98] Francesco Avanzini, Gianmaria Falasco, and Massimiliano Esposito. Thermodynamics of chemical waves. *The Journal of Chemical Physics*, 151(23):234103, dec 2019. 27

[99] Rebecca A Green, Ewa Paluch, and Karen Oegema. Cytokinesis in Animal Cells. *Annual Review of Cell and Developmental Biology*, 28(1):29–58, 2012. 29

[100] Akankshi Munjal and Thomas Lecuit. Actomyosin networks and tissue morphogenesis. *Development*, 141(9):1789–1793, 2014. 29

[101] A.F. Huxley. Muscle structure and theories of contraction. *Progress in Biophysics and Biophysical Chemistry*, 7:255–318, 1957. 29, 31, 42

[102] H.E. Huxley. The double array of filaments in cross-striated muscle. *The Journal of Biophysical and Biochemical Cytology*, 3(5):631–48, sep 1957. 29, 31

[103] M L Gardel, F Nakamura, J H Hartwig, J C Crocker, T P Stossel, and D A Weitz. Prestressed F-actin networks cross-linked by hinged filamins replicate mechanical properties of cells. *Proceedings of the National Academy of Sciences*, 103(6):1762–1767, 2006. 29

[104] Ben Fabry, Geoffrey N Maksym, James P Butler, Michael Glogauer, Daniel Navajas, and Jeffrey J Fredberg. Scaling the Microrheology of Living Cells. *Physical Review Letters*, 87(14):148102, sep 2001. 30

[105] Annafrancesca Rigato, Atsushi Miyagi, Simon Scheuring, and Felix Rico. High-frequency microrheology reveals cytoskeleton dynamics in living cells. *Nature Physics*, 13(8):771–775, may 2017. 30

[106] Edwin Munro, Jeremy Nance, and James R. Priess. Cortical flows powered by asymmetrical contraction transport PAR proteins to establish and maintain anterior-posterior polarity in the early C. elegans embryo. *Developmental Cell*, 2004. 31

[107] Masatoshi Nishikawa, Sundar Ram Naganathan, Frank Jülicher, and Stephan W. Grill. Controlling contractile instabilities in the actomyosin cortex. *eLife*, 6, jan 2017. 31

[108] Aaron F. Straight, Amy Cheung, John Limouze, Irene Chen, Nick J. Westwood, James R. Sellers, and Timothy J. Mitchison. Dissecting temporal and spatial control of cytokinesis with a myosin II inhibitor. *Science*, 2003. 31

[109] Adam C. Martin, Matthias Kaschube, and Eric F. Wieschaus. Pulsed contractions of an actin-myosin network drive apical constriction. *Nature*, 2009. 31

[110] William M. Bement, Marcin Leda, Alison M. Moe, Angela M. Kita, Matthew E. Larson, Adriana E. Golding, Courtney Pfeuti, Kuan-Chung Su, Ann L. Miller, Andrew B. Goryachev, and George von Dassow. Activatorinhibitor coupling

between Rho signalling and actin assembly makes the cell cortex an excitable medium. *Nature Cell Biology*, 17(11):1471–1483, 10 2015. 31, 62, 82, 88

[111] Jan Brugués and Daniel Needleman. Physical basis of spindle self-organization. *PNAS*, 111(52):18496–500, 2014. 31

[112] Tim Sanchez, Daniel T. N. Chen, Stephen J. DeCamp, Michael Heymann, and Zvonimir Dogic. Spontaneous motion in hierarchically assembled active matter. *Nature*, 491(7424):431–434, nov 2012. 31, 34

[113] Stephen J DeCamp, Gabriel S Redner, Aparna Baskaran, Michael F Hagan, and Zvonimir Dogic. Orientational order of motile defects in activenematics. *Nature Materials*, 14(11):1110–1115, 2015. 31, 34

[114] Martin Lenz. Geometrical Origins of Contractility in Disordered Actomyosin Networks. *Physical Review X*, 4(4):041002, oct 2014. 31, 49

[115] Sven K Vogel, Zdenek Petrasek, Fabian Heinemann, and Petra Schwille. Myosin motors fragment and compact membrane-bound actin filaments. *eLife*, 2:e00116, jan 2013. 31

[116] Simone Köhler, Volker Schaller, and Andreas R Bausch. Structure formation in active networks. *Nature Materials*, 10(6):462–468, 2011. 31

[117] Marina Soares E Silva, Martin Depken, Björn Stuhrmann, Marijn Korsten, Fred C. MacKintosh, and Gijsje H. Koenderink. Active multistage coarsening of actin networks driven by myosin motors. *PNAS*, 108(23):9408–9413, 2011. 31

[118] P. M. Chaikin and T. C. Lubensky. *Principles of condensed matter physics*. Cambridge University Press, Cambridge, 1995. 34, 48

[119] Frederick Gittes, Brian Mickey, Jilda Nettleton, and Jonathon Howard. Flexural rigidity of microtubules and actin filaments measured from thermal fluctuations in shape. *Journal of Cell Biology*, 120(4):923–934, feb 1993. 34, 39

[120] Rui Zhang, Nitin Kumar, Jennifer L Ross, Margaret L Gardel, and Juan J de Pablo. Interplay of structure, elasticity, and dynamics in actin-based nematic materials. *Proceedings of the National Academy of Sciences*, 115(2):E124—-E133, 2018. 34

[121] Nitin Kumar, Rui Zhang, Juan J. de Pablo, and Margaret L. Gardel. Tunable structure and dynamics of active liquid crystals. *Science Advances*, 4(10):eaat7779, oct 2018. 34

[122] Martin Lenz, Todd Thoresen, Margaret L. Gardel, and Aaron R. Dinner. Contractile Units in Disordered Actomyosin Bundles Arise from F-Actin Buckling. *Physical Review Letters*, 108(23):238107, jun 2012. 34

[123] A. Melling. Tracer particles and seeding for particle image velocimetry. *Measurement Science and Technology*, 8(12):1406–1416, dec 1997. 34

[124] Joel L. Lebowitz and Herbert Spohn. A Gallavotti-Cohen-Type Symmetry in the large deviation functional for stochastic dynamics. *Journal of Statistical Physics*, 95(1/2):333–365, 1999. 35

[125] Sergio R. Aragon and R. Pecora. Dynamics of wormlike chains. *Macromolecules*, 18(10):1868–1875, 1985. 35, 90

[126] T Speck, V Blickle, C Bechinger, and U Seifert. Distribution of entropy production for a colloidal particle in a nonequilibrium steady state. *Europhysics Letters*, 79(3):30002, 2007. 38

[127] José García de la Torre and Victor A. Bloomfield. Hydrodynamic properties of complex, rigid, biological macromolecules: theory and applications. *Quarterly Reviews of Biophysics*, 14(1):81–139, feb 1981. 38

[128] Gavin E. Crooks. Path-ensemble averages in systems driven far from equilibrium. *Physical Review E*, 61(3):2361–2366, 2000. 38

[129] Francois Nedelec and Dietrich Foethke. Collective Langevin dynamics of flexible cytoskeletal fibers. *New Journal of Physics*, 9(11):427–427, 2007. 39, 46, 96

[130] Pierre Ronceray, Chase P. Broedersz, and Martin Lenz. Fiber plucking by molecular motors yields large emergent contractility in stiff biopolymer networks. *Soft Matter*, 15(7):1481–1487, 2019. 44

[131] M. L. Gardel, J. H. Shin, F. C. MacKintosh, L. Mahadevan, P. Matsudaira, and D. A. Weitz. Elastic behavior of cross-linked and bundled actin networks. *Science*, 304(5675):1301–1305, may 2004. 46

[132] C. G. Dos Remedios, D. Chhabra, M. Kekic, I. V. Dedova, M. Tsubakihara, D. A. Berry, and N. J. Nosworthy. Actin binding proteins: Regulation of cytoskeletal microfilaments, 2003. 46

[133] Ekta Seth Chhabra and Henry N. Higgs. The many faces of actin: Matching assembly factors with cellular structures. *Nature Cell Biology*, 9(10):1110–1121, oct 2007. 46

[134] K. E. Kasza, C. P. Broedersz, G. H. Koenderink, Y. C. Lin, W. Messner, E. A. Millman, F. Nakamura, T. P. Stossel, F. C. MacKintosh, and D. A. Weitz. Actin filament length tunes elasticity of flexibly cross-linked actin networks. *Biophysical Journal*, 99(4):1091–1100, aug 2010. 46

[135] Karsten Kruse, Jean-Francois Joanny, Frank Jülicher, Jacques Prost, and K. Sekimoto. Generic theory of active polar gels: a paradigm for cytoskeletal dynamics. *The European Physical Journal E*, 16(1):5–16, 2005. 46

[136] Daniel S. Seara, Vikrant Yadav, Ian Linsmeier, A. Pasha Tabatabai, Patrick W. Oakes, S. M. Ali Tabei, Shiladitya Banerjee, and Michael P. Murrell. Entropy production rate is maximized in non-contractile actomyosin. *Nature Communications*, 9(1):4948, 12 2018. 46, 63

[137] S L Freedman, S Banerjee, G M Hocky, and A R Dinner. A Versatile Framework for Simulating the Dynamic Mechanical Structure of Cytoskeletal Networks. *Biophysical Journal*, 113(2):448–460, 2017. 46, 49, 96, 98

[138] S L Freedman, G M Hocky, S Banerjee, and A R Dinner. Nonequilibrium phase diagrams for actomyosin networks. *Soft Matter*, 14(37):7740–7747, 2018. 46, 53

[139] G.I. Bell. Models for the specific adhesion of cells to cells. *Science*, 200(4342):618–627, may 1978. 47

[140] Franck J. Vernerey and Umut Akalp. Role of catch bonds in actomyosin mechanics and cell mechanosensitivity. *Physical Review E*, 94(1):012403, jul 2016. 47, 49

[141] Bryan T. Marshall, Mian Long, James W. Piper, Tadayuki Yago, Rodger P. McEver, and Cheng Zhu. Direct observation of catch bonds involving cell-adhesion molecules. *Nature*, 423(6936):190–193, may 2003. 47

[142] Wendy E Thomas, Elena Trintchina, Manu Forero, Viola Vogel, and Evgeni V Sokurenko. Bacterial Adhesion to Target Cells Enhanced by Shear Force. *Cell*, 109(7):913–923, 2002. 47

[143] E A Mason and W E Rice. The Intermolecular Potentials for Some Simple Nonpolar Molecules. *Journal of Chemical Physics*, 22(5):843–851, 1954. 48

[144] J Rottler and M O Robbins. Jamming under tension in polymer crazes. *Physical Review Letters*, 89(19), 2002. 48

[145] A N Gupta, A Vincent, K Neupane, H Yu, F Wang, and M T Woodside. Experimental validation of free-energy-landscape reconstruction from non-equilibrium single-molecule force spectroscopy measurements. *Nature Physics*, 7(8):631–634, 2011. 48

[146] H Yu, A N Gupta, X Liu, K Neupane, A M Brigley, I Sosova, and M T Woodside. Energy landscape analysis of native folding of the prion protein yields the diffusion constant, transition path time, and rates. *PNAS*, 109(36):14452–14457, 2012. 48

[147] J E Komianos and G A Papoian. Stochastic Ratcheting on a Funneled Energy Landscape Is Necessary for Highly Efficient Contractility of Actomyosin Force Dipoles. *Physical Review X*, 8(2), 2018. 48

[148] K W Desmond and E R Weeks. Measurement of Stress Redistribution in Flowing Emulsions. *Physical Review Letters*, 115(9):98302, 2015. 48

[149] T Bauer, J Oberdisse, and L Ramos. Collective rearrangement at the onset of flow of a polycrystalline hexagonal columnar phase. *Physical Review Letters*, 97(25):258303, 2006. 48

[150] P Hebraud, F Lequeux, J P Munch, and D J Pine. Yielding and rearrangements in disordered emulsions. *Physical Review Letters*, 78(24):4657–4660, 1997. 48

[151] V V Vasisht, S K Dutta, E Del Gado, and D L Blair. Rate Dependence of Elementary Rearrangements and Spatiotemporal Correlations in the 3D Flow of Soft Solids. *Physical Review Letters*, 120(1):18001, 2018. 48

[152] T Gibaud, D Frelat, and S Manneville. Heterogeneous yielding dynamics in a colloidal gel. *Soft Matter*, 6(15):3482–3488, 2010. 48

[153] B J Landrum, W B Russel, and R N Zia. Delayed yield in colloidal gels: Creep, flow, and re-entrant solid regimes. *Journal of Rheology*, 60(4):783–807, 2016. 48

[154] K C Dansuk and S Keten. A Simple Mechanical Model for Synthetic Catch Bonds. *Matter*, 1(4):911–925, 2019. 48, 60

[155] B V S Iyer, V V Yashin, and A C Balazs. Harnessing biomimetic catch bonds to create mechanically robust nanoparticle networks. *Polymer*, 69:310–320, 2015. 48, 60

[156] T Zhang, B L Mbanga, V V Yashin, and A C Balazs. Tailoring the mechanical properties of nanoparticle networks that encompass biomimetic catch bonds. *Journal of Polymer Science Part B-Polymer Physics*, 56(1):105–118, 2018. 48, 60

[157] Visar Ajeti, A.P. Pasha Tabatabai, Andrew J. A.J. Fleszar, M.F. Michael F. Staddon, Daniel S. D.S. Seara, Cristian Suarez, M.S. Sulaiman Yousafzai, Dapeng Bi, David R. D.R. Kovar, Shiladitya Banerjee, and Michael P. M.P. Murrell. Wound healing coordinates actin architectures to regulate mechanical work. *Nature Physics*, 15(7):1, apr 2019. 48

[158] V Yadav, D S Banerjee, A P Tabatabai, D R Kovar, T Kim, S Banerjee, and M P Murrell. Filament Nucleation Tunes Mechanical Memory in Active Polymer Networks. *Advanced Functional Materials*, 29(49), 2019. 48

[159] D Bray and J G White. Cortical flow in animal cells. *Science*, 239(4842):883–888, 1988. 48

[160] J T Finer, R M Simmons, and J A Spudich. Single myosin molecule mechanics: piconewton forces and nanometre steps. *Nature*, 368(6467):113–119, 1994. 49

[161] T Yanagida, T Arata, and F Oosawa. Sliding Distance of Actin Filament Induced by a Myosin Crossbridge during One Atp Hydrolysis Cycle. *Nature*, 316(6026):366–369, 1985. 49

[162] E M De La Cruz and E M Ostap. Relating biochemistry and function in the myosin superfamily. *Current Opinion in Cell Biology*, 16(1):61–67, 2004. 49

[163] C Veigel, L M Coluccio, J D Jontes, J C Sparrow, R A Milligan, and J E Molloy. The motor protein myosin-I produces its working stroke in two steps. *Nature*, 398(6727):530–533, 1999. 49

[164] M Whittaker, E M Wilson-Kubalek, J E Smith, L Faust, R A Milligan, and H L Sweeney. A 35-A movement of smooth muscle myosin on ADP release. *Nature*, 378(6558):748–751, 1995. 49

[165] S F Wulf, V Ropars, S Fujita-Becker, M Oster, G Hofhaus, L G Trabuco, O Pylypenko, H L Sweeney, A M Houdusse, and R R Schroder. Force-producing ADP state of myosin bound to actin. *PNAS*, 113(13):E1844–E1852, 2016. 49

[166] M Kovacs, F Wang, A Hu, Y Zhang, and J R Sellers. Functional divergence of human cytoplasmic myosin II: kinetic characterization of the non-muscle IIA isoform. *J Biol Chem*, 278(40):38132–38140, 2003. 49

[167] J M Laakso, J H Lewis, H Shuman, and E M Ostap. Myosin I can act as a molecular force sensor. *Science*, 321(5885):133–136, 2008. 49, 60

[168] N Hundt, W Steffen, S Pathan-Chhatbar, M H Taft, and D J Manstein. Load-dependent modulation of non-muscle myosin-2A function by tropomyosin 4.2. *Scientific Reports*, 6:20554, 2016. 49

[169] C Veigel, J E Molloy, S Schmitz, and J Kendrick-Jones. Load-dependent kinetics of force production by smooth muscle myosin measured with optical tweezers. *Nature Cell Biology*, 5(11):980–986, 2003. 49

[170] T Erdmann and U S Schwarz. Stochastic force generation by small ensembles of myosin II motors. *Physical Review Letters*, 108(18):188101, 2012. 49, 97

[171] E Rozbicki, M Chuai, A I Karjalainen, F Song, H M Sang, R Martin, H J Knolker, M P MacDonald, and C J Weijer. Myosin-II-mediated cell shape changes and cell intercalation contribute to primitive streak formation. *Nature Cell Biology*, 17(4):397–408, 2015. 49

[172] D Vavylonis, D R Kovar, B O'Shaughnessy, and T D Pollard. Model of formin-associated actin filament elongation. *Molecular Cell*, 21(4):455–466, 2006. 49

[173] N Courtemanche and T D Pollard. Interaction of profilin with the barbed end of actin filaments. *Biochemistry*, 52(37):6456–6466, 2013. 49

[174] Robert Blackwell, Oliver Sweezy-Schindler, Christopher Baldwin, Loren E. Hough, Matthew A. Glaser, and M. D. Betterton. Microscopic origins of anisotropic active stress in motor-driven nematic liquid crystals. *Soft Matter*, 12(10):2676–2687, 2016. 49

[175] Y V Pereverzev, O V Prezhdo, M Forero, E V Sokurenko, and W E Thomas. The two-pathway model for the catch-slip transition in biological adhesion. *Biophysical Journal*, 89(3):1446–1454, 2005. 50

[176] J E Molloy, J E Burns, J Kendrick-Jones, R T Tregear, and D C S White. Movement and force produced by a single myosin head. *Nature*, 378(6553):209–212, 1995. 50

[177] G E Crooks. Nonequilibrium measurements of free energy differences for microscopically reversible Markovian systems. *Journal of Statistical Physics*, 90(5-6):1481–1487, 1998. 52

[178] Robert Marsland and Jeremy L. England. Limits of predictions in thermodynamic systems: a review. *Reports on Progress in Physics*, 81(1):016601, jan 2018. 52

[179] V Wollrab, J M Belmonte, L Baldauf, M Leptin, F Nedelec, and G H Koenderink. Polarity sorting drives remodeling of actin-myosin networks. *Journal of Cell Science*, 132(4), 2018. 53

[180] Konstantin Popov, James Komianos, and Garegin A. Papoian. MEDYAN: Mechanochemical Simulations of Contraction and Polarity Alignment in Actomyosin Networks. *PLOS Computational Biology*, 12(4):e1004877, 2016. 53, 96

[181] C P Broedersz, X M Mao, T C Lubensky, and F C MacKintosh. Criticality and isostaticity in fibre networks. *Nature Physics*, 7(12):983–988, 2011. 54

[182] M Sheinman, C P Broedersz, and F C MacKintosh. Nonlinear effective-medium theory of disordered spring networks. *Physical Review E*, 85(2), 2012. 54

[183] James Clerk Maxwell. On the calculation of the equilibrium and stiffness of frames. *The London, Edinburgh, and Dublin Philosophical Magazine and Journal of Science*, 27(182):294–299, apr 1864. 56

[184] K Manibog, H Li, S Rakshit, and S Sivasankar. Resolving the molecular mechanism of cadherin catch bond formation. *Nature Communications*, 5:3941, 2014. 58

[185] F Kong, A J Garcia, A P Mould, M J Humphries, and C Zhu. Demonstration of catch bonds between an integrin and its ligand. *Journal of Cell Biology*, 185(7):1275–1284, 2009. 58, 97

[186] D L Huang, N A Bax, C D Buckley, W I Weis, and A R Dunn. Vinculin forms a directionally asymmetric catch bond with F-actin. *Science*, 357(6352):703–706, 2017. 58, 60

[187] Urna Basu and Christian Maes. Nonequilibrium Response and Frenesy. *Journal of Physics: Conference Series*, 638(1):012001, sep 2015. 59

[188] Christian Maes. Frenesy: Time-symmetric dynamical activity in nonequilibria. *Physics Reports*, 850:1–33, 2020. 59

[189] C Floyd, G A Papoian, and C Jarzynski. Quantifying dissipation in actomyosin networks. *Interface Focus*, 9(3):20180078, 2019. 60

[190] B Akiyoshi, K K Sarangapani, A F Powers, C R Nelson, S L Reichow, H Arellano-Santoyo, T Gonen, J A Ranish, C L Asbury, and S Biggins. Tension directly stabilizes reconstituted kinetochore-microtubule attachments. *Nature*, 468(7323):576–U255, 2010. 60

[191] A Yamada, A Mamane, J Lee-Tin-Wah, A Di Cicco, C Prevost, D Levy, J F Joanny, E Coudrier, and P Bassereau. Catch-bond behaviour facilitates membrane tubulation by non-processive myosin 1b. *Nature Communications*, 5, 2014. 60

[192] John Toner and Yuhai Tu. Flocks, herds, and schools: A quantitative theory of flocking. *Physical Review E*, 58(4):4828–4858, 10 1998. 61, 63

[193] Igor S. Aranson and Lorenz Kramer. The world of the complex Ginzburg-Landau equation. *Reviews of Modern Physics*, 74(1):99–143, feb 2002. 61

[194] Sriram Ramaswamy. The Mechanics and Statistics of Active Matter. *Annual Review of Condensed Matter Physics*, 1(1):323–345, 8 2010. 61, 63

[195] P. C. Hohenberg and B. I. Halperin. Theory of dynamic critical phenomena. *Reviews of Modern Physics*, 49(3):435–479, 7 1977. 62, 64, 68

[196] Jeremy B A Green and James Sharpe. Positional information and reaction-diffusion: two big ideas in developmental biology combine. *Development*, 142(7):1203–1211, apr 2015. 62

[197] A. L. Hodgkin and A. F. Huxley. A quantitative description of membrane current and its application to conduction and excitation in nerve. *The Journal of Physiology*, 117(4):500–544, aug 1952. 62

[198] Hiroshi Ito, Hakuto Kageyama, Michinori Mutsuda, Masato Nakajima, Tokitaka Oyama, and Takao Kondo. Autonomous synchronization of the circadian KaiC phosphorylation rhythm. *Nature Structural & Molecular Biology*, 14(11):1084–1088, nov 2007. 62

[199] Masato Nakajima, Keiko Imai, Hiroshi Ito, Taeko Nishiwaki, Yoriko Murayama, Hideo Iwasaki, Tokitaka Oyama, and Takao Kondo. Reconstitution of Circadian Oscillation of Cyanobacterial KaiC Phosphorylation in Vitro. *Science*, 308(5720):414–415, 2005. 62

[200] Joe Lutkenhaus. Assembly Dynamics of the Bacterial MinCDE System and Spatial Regulation of the Z Ring. *Annual Review of Biochemistry*, 76(1):539–562, jun 2007. 62

[201] Tzer Han Tan, Jinghui Liu, Pearson W. Miller, Melis Tekant, Jörn Dunkel, and Nikta Fakhri. Topological turbulence in the membrane of a living cell. *Nature Physics*, pages 1–6, mar 2020. 62

[202] Juan M. R. Parrondo, C Van den Broeck, and R Kawai. Entropy production and the arrow of time. *New Journal of Physics*, 11(7):073008, 7 2009. 63, 64

[203] Andre C. Barato and Udo Seifert. Thermodynamic Uncertainty Relation for Biomolecular Processes. *Physical Review Letters*, 114(15):158101, 4 2015. 63, 76

[204] Benjamin B. Machta. Dissipation Bound for Thermodynamic Control. *Physical Review Letters*, 115(26):260603, 12 2015. 63

[205] Samuel J Bryant and Benjamin B Machta. Energy dissipation bounds for autonomous thermodynamic cycles. *PNAS*, 117(7):3478–3483, 2020. 63

[206] Q. Ouyang and Harry L. Swinney. Transition from a uniform state to hexagonal and striped Turing patterns. *Nature*, 352(6336):610–612, 8 1991. 63

[207] I. Prigogine. *Introduction to thermodynamics of irreversible processes*. Wiley, 1967. 63

[208] Edgar Roldan and Juan M. R. Parrondo. Estimating Dissipation from Single Stationary Trajectories. *Physical Review Letters*, 105(15):150607, 10 2010. 63

[209] Junang Li, Jordan M. Horowitz, Todd R. Gingrich, and Nikta Fakhri. Quantifying dissipation using fluctuating currents. *Nature Communications*, 10(1):1666, 12 2019. 63, 76

[210] Anna Frishman and Pierre Ronceray. Learning force fields from stochastic trajectories. *Physical Review X*, 10:021009, Apr 2020. 63

[211] Ignacio A. Martínez, Gili Bisker, Jordan M. Horowitz, and Juan M. R. Parrondo. Inferring broken detailed balance in the absence of observable currents. *Nature Communications*, 10(1):3542, 12 2019. 63, 74

[212] Pierre Gaspard. Fluctuation theorem for nonequilibrium reactions. *Journal of Chemical Physics*, 120(19):8898–8905, 5 2004. 63

[213] Tnia Tomé and Mrio J. de Oliveira. Entropy Production in Nonequilibrium Systems at Stationary States. *Physical Review Letters*, 108(2):020601, 1 2012. 63

[214] C. E. Fernndez Noa, Pedro E. Harunari, M. J. de Oliveira, and C. E. Fiore. Entropy production as a tool for characterizing nonequilibrium phase transitions. *Physical Review E*, 100(1):012104, 7 2019. 63, 81

[215] Yirui Zhang and Andre C Barato. Critical behavior of entropy production and learning rate: Ising model with an oscillating field. *Journal of Statistical Mechanics*, 2016(11):113207, Nov 2016. 63, 77

[216] Hao Ge and Hong Qian. Thermodynamic limit of a nonequilibrium steady state: Maxwell-type construction for a bistable biochemical system. *Physical Review Letters*, 103(14):148103, oct 2009. 63

[217] Hao Ge and Hong Qian. Non-equilibrium phase transition in mesoscopic biochemical systems: from stochastic to nonlinear dynamics and beyond. *J. R. Soc. Interface*, 8(54):107–116, Jan 2011. 63

[218] Basile Nguyen, Udo Seifert, and Andre C. Barato. Phase transition in thermodynamically consistent biochemical oscillators. *Journal of Chemical Physics*, 149(4):045101, Jul 2018. 63, 81

[219] Laura Tociu, Étienne Fodor, Takahiro Nemoto, and Suriyanarayanan Vaikuntanathan. How Dissipation Constrains Fluctuations in Nonequilibrium Liquids: Diffusion, Structure, and Biased Interactions. *Physical Review X*, 9(4):041026, Nov 2019. 63, 81

[220] Basile Nguyen and Udo Seifert. Exponential volume dependence of entropy-current fluctuations at first-order phase transitions in chemical reaction networks. *Physical Review E*, 102:022101, Aug 2020. 63

[221] Shubhashis Rana and Andre C. Barato. Precision and dissipation of a stochastic turing pattern. *Physical Review E*, 102:032135, Sep 2020. 63, 72, 81

[222] Cesare Nardini, Etienne Fodor, Elsen Tjhung, Frdric van Wijland, Julien Tailleur, and Michael E. Cates. Entropy production in field theories without time-reversal symmetry: Quantifying the non-equilibrium character of active matter. *Physical Review X*, 7(2), 2017. 68, 69, 81

[223] Takahiro Harada and Shin-ichi Sasa. Energy dissipation and violation of the fluctuation-response relation in nonequilibrium Langevin systems. *Physical Review E*, 73(2):026131, 2 2006. 69

[224] I. Prigogine and R. Lefever. Symmetry Breaking Instabilities in Dissipative Systems. II. *Journal of Chemical Physics*, 48(4):1695–1700, 2 1968. 72

[225] Hong Qian, Saveez Saffarian, and Elliot L. Elson. Concentration fluctuations in a mesoscopic oscillating chemical reaction system. *Proc. Natl Acad. Sci. USA*, 99(16):10376–81, 8 2002. 72, 73

[226] Chenyi Fei, Yuansheng Cao, Qi Ouyang, and Yuhai Tu. Design principles for enhancing phase sensitivity and suppressing phase fluctuations simultaneously in biochemical oscillatory systems. *Nature Communications*, 9(1):1434, Dec 2018. 72

[227] Christian Maes and Maarten H. van Wieren. Time-Symmetric Fluctuations in Nonequilibrium Systems. *Physical Review Letters*, 96(24):240601, 6 2006. 72

[228] Todd R. Gingrich, Grant M. Rotskoff, and Jordan M. Horowitz. Inferring dissipation from current fluctuations. *Journal of Physics A*, 50(18):184004, 4 2017. 73

[229] Jeffrey B. Weiss, Baylor Fox-Kemper, Dibyendu Mandal, Arin D. Nelson, and R. K. P. Zia. Nonequilibrium Oscillations, Probability Angular Momentum, and the Climate System. *Journal of Statistical Physics*, pages 1–18, 10 2019. 73

[230] Naoto Shiraishi and Takahiro Sagawa. Fluctuation theorem for partially masked nonequilibrium dynamics. *Physical Review E*, 91(1):012130, 1 2015. 74

[231] Matteo Polettini and Massimiliano Esposito. Effective Thermodynamics for a Marginal Observer. *Physical Review Letters*, 119(24):240601, 12 2017. 74, 82

[232] Massimiliano Esposito. Stochastic thermodynamics under coarse graining. *Physical Review E*, 85(4):041125, apr 2012. 76, 109

[233] Jordan M. Horowitz and Todd R. Gingrich. Proof of the finite-time thermodynamic uncertainty relation for steady-state currents. *Physical Review E*, 96(2):020103, Aug 2017. 76

[234] Édgar Roldán, Izaak Neri, Meik Dörpinghaus, Heinrich Meyr, and Frank Jülicher. Decision Making in the Arrow of Time. *Physical Review Letters*, 115(25):250602, dec 2015. 76

[235] Juan A. Acebrón, L. L. Bonilla, Conrad J.Pérez Vicente, Félix Ritort, and Renato Spigler. The Kuramoto model: A simple paradigm for synchronization phenomena. *Reviews of Modern Physics*, 77(1):137–185, jan 2005. 80

[236] Dongliang Zhang, Yuansheng Cao, Qi Ouyang, and Yuhai Tu. The energy cost and optimal design for synchronization of coupled molecular oscillators. *Nature Physics*, pages 1–6, 11 2019. 80

[237] Sarthak Chandra, Michelle Girvan, and Edward Ott. Continuous versus discontinuous transitions in the d-dimensional generalized kuramoto model: Odd d is different. *Physical Review X*, 9:011002, Jan 2019. 80

[238] Bo Sun, Jiayi Lin, Ellis Darby, Alexander Y. Grosberg, and David G. Grier. Brownian vortexes. *Physical Review E*, 80(1):010401, 7 2009. 82

[239] Stefano Martiniani, Paul M. Chaikin, and Dov Levine. Quantifying Hidden Order out of Equilibrium. *Physical Review X*, 9(1):011031, 2 2019. 82

[240] Bi-Chang Chen, Wesley R. Legant, Kai Wang, Lin Shao, Daniel E. Milkie, Michael W. Davidson, Chris Janetopoulos, Xufeng S. Wu, John A. Hammer, Zhe Liu, Brian P. English, Yuko Mimori-Kiyosue, Daniel P. Romero, Alex T. Ritter, Jennifer Lippincott-Schwartz, Lillian Fritz-Laylin, R. Dyche Mullins, Diana M. Mitchell, Joshua N. Bembenek, Anne-Cecile Reymann, Ralph Böhme, Stephan W. Grill, Jennifer T. Wang, Geraldine Seydoux, U. Serdar Tulu, Daniel P. Kiehart, and Eric Betzig. Lattice light-sheet microscopy: Imaging molecules to embryos at high spatiotemporal resolution. *Science*, 346(6208):1257998, 10 2014. 83

[241] Sandrine Etienne-Manneville and Alan Hall. Rho GTPases in cell biology. *Nature*, 420(6916):629–635, dec 2002. 88

[242] Maureen Cetera, Guillermina R. Ramirez-San Juan, Patrick W. Oakes, Lindsay Lewellyn, Michael J. Fairchild, Guy Tanentzapf, Margaret L. Gardel, and Sally Horne-Badovinac. Epithelial rotation promotes the global alignment of contractile actin bundles during Drosophila egg chamber elongation. *Nature Communications*, 5(1):5511, dec 2014. 89

[243] P Sartori, V F Geyer, A Scholich, F Jülicher, and J Howard. Data from: Dynamic curvature regulation accounts for the symmetric and asymmetric beats of Chlamydomonas flagella, 2016. 93

[244] C Vrusch and C Storm. Catch bonding in the forced dissociation of a polymer endpoint. *Physical Review E*, 97(4-1):42405, 2018. 97

[245] P. C. Martin, E. D. Siggia, and H. A. Rose. Statistical Dynamics of Classical Systems. *Phys. Rev. A*, 8(1):423–437, 7 1973. 104

ProQuest Number: 28321627

INFORMATION TO ALL USERS
The quality and completeness of this reproduction is dependent on the quality
and completeness of the copy made available to ProQuest.

Distributed by ProQuest LLC (2021).
Copyright of the Dissertation is held by the Author unless otherwise noted.

This work may be used in accordance with the terms of the Creative Commons license
or other rights statement, as indicated in the copyright statement or in the metadata
associated with this work. Unless otherwise specified in the copyright statement
or the metadata, all rights are reserved by the copyright holder.

This work is protected against unauthorized copying under Title 17,
United States Code and other applicable copyright laws.

Microform Edition where available © ProQuest LLC. No reproduction or digitization
of the Microform Edition is authorized without permission of ProQuest LLC.

ProQuest LLC
789 East Eisenhower Parkway
P.O. Box 1346
Ann Arbor, MI 48106 - 1346 USA